Examination of a locus coeruleus to dentate gyrus noradrenergic circuit in aversive contextual processing

Eric Zhang

A dissertation

submitted in partial fulfillment of the

requirements for the degree of

Doctor of Philosophy

University of Washington

2024

Reading Committee:

Michael R. Bruchas, Chair

Garret Stuber

Larry Zweifel

Program Authorized to Offer Degree:

Bioengineering

University of Washington

Abstract

Examination of a locus coeruleus to dentate gyrus noradrenergic circuit in aversive contextual processing

Eric Zhang

Chair of the Supervisory Committee:

Michael R. Bruchas

Department of Pharmacology

Dysregulation in aversive contextual processing is believed to affect several forms of psychopathology, including post-traumatic stress disorder (PTSD). The dentate gyrus (DG), a subregion of the hippocampus, is thought to be an important brain region for disambiguating new experiences from prior memories. Noradrenergic (NE) neurons in the locus coeruleus (LC) are more tonically active during stressful events and send dense projections to the DG, yet an understanding of their function in DG-dependent contextual discrimination has not been established. In this thesis, I isolate a key function of the LC-DG noradrenergic circuit in contextual aversive processing using selective manipulations and *in vivo* calcium imaging. In **Chapter 1**, we review the current understanding of LC-DG noradrenergic circuitry in aversive contextual processing, and its role in post-

traumatic stress disorder. Next, we explore how activation of LC-NE neurons and terminal activity results in contextual generalization, while inhibition of this circuit results in facilitation of contextual disambiguation (**Chapter 2**). Additionally, we uncover how neural ensemble shifts in the DG granule cell layer (GCL) observed during contextual processing using *in vivo* 1-photon calcium imaging are involved in successful contextual discrimination, while failure in contextual discrimination is associated with a lack of neural ensemble shift in the DG (**Chapter 3**). In **Chapter 4**, we elucidate the effect of β-adrenergic receptor-mediated modulation of DG hilar interneurons to ultimately promote aversive generalization. Then, using *in vivo* fiber photometry, we demonstrate that prolonged NE release in the DG during aversive contextual processing results in successful contextual discrimination, even in the absence of an aversive stimulus, suggesting that norepinephrine dynamics in the DG serve an important role in driving contextual discrimination (**Chapter 5**). Altogether, the findings of this thesis suggest that modulation of LC-DG noradrenergic circuitry may serve as an important avenue for treating stress-induced disorders. Lastly, in **Chapter 6**, we outline our conclusions and future work to further build upon the findings of this thesis.

Table of Contents

List of Figures

List of Tables

Acknowledgements

I have so many people to thank for the roles they played in helping me and supporting me during my graduate studies, and even before that. It has been an incredible journey through the many years that this degree has taken, and I would like to take this opportunity to express my sincerest gratitude to everyone who has been there for me and helped me along the way.

First and foremost, I want to thank my mentor and dissertation advisor, Dr. Michael R. Bruchas. I am forever grateful that Michael agreed to take me on as a rotation student when I was just starting out in graduate school in Washington University in St. Louis and welcomed me with open arms. Not only did he accept me into the research group, but he also offered the opportunity to move with the lab to University of Washington even though I had only formally joined the lab a few months prior. Throughout our years together he has been an incredible mentor and helped me grow so much as a scientist and an intellectual. Being a mentor is hard in the best of times, and certainly it is made even harder by things such as moving research institutions, and by a pandemic. So, to Michael, I have the utmost gratitude and respect.

I would also like to thank my thesis committee, Dr. Garret D. Stuber, Dr. Larry S. Zweifel, Dr. Andre Berndt, Dr. Azadeh Yazdan-Shahmorad, and Dr. Sheri J.Y. Mizumori, for their expertise, support, and guidance. Together they helped to shape this thesis and provided me with valuable insight and guidance during the completion of my project.

I would also like to extend my gratitude to all the members of the Bruchas Lab, who have been an incredible group to work with. We have been able to form such a diverse, close-knit community within this lab, and I am so proud of us for coming together

in the face of adversities like the pandemic to become better scientists and people, and I am so grateful I have had the opportunity to work with all of you. Specific thanks go out to our lab managers, Chris Stander, and Dr. Azra Suko, as well as to our various lab technicians, who helped keep things running smoothly in the lab, allowing me to focus strictly on science during my time in lab. I would like to thank Dr. Daniel C. Castro, who was my mentor during my rotation in the lab, for teaching me so much and for his endless patience during my initial learning period. I want to thank Dr. Dong-oh Seo, who served as a source of great knowledge as I integrated myself into this research area. I would also like to thank Dr. Sean C. Piantadosi, who has proved an invaluable source of guidance during my research and provided many ideas and inspiration during my thesis work. Your kindness, work ethic, and patience will serve as a model for how I aim to behave as a mentor in the future. I would also like to thank my undergraduate students Bryce K. Kan, and Grace S. Saglimbeni, for their dedication and hard work. Without them, many of the experiments and data collected would not have been possible.

I would also like to thank Dr. Yi Zhang and Dr. Guangfu Wu at the University of Connecticut, with whom I have had the pleasure of collaborating. Together, we have been able to develop cutting edge new tools which can be used to further the field of neuroscience, and it has been a unique experience that has pushed me to step out of my comfort zone.

Of course, that only covers the professional side of all the support I received. I owe so much to my wonderful family, who have supported me from the moment I was born and will continue to support me in all of my future endeavors. My parents instilled in me so many positive values from an early age, including my interest in science and math,

and my proclivity for asking questions and exploring the unknown. Thank you to my dad Ji Zhang, who showed me the value of hard work and dedication, thank you to my mom Wenli Hu, who has always been there for me and taken such good care of me, and thank you to my sister Gina Zhang, who is always there for me whenever I need an ear to listen to me, or a funny video to laugh at. I love all of you so very much, and I could not have done this without you.

I also cannot go without thanking all of my various friends who served as such an amazing support group; without all of you I could not have braved the adversities and lows of my graduate degree, and I could not have celebrated the victories and highs either. To my biomedical engineering PhD cohort at Washington University in St. Louis and my friends in St. Louis, who remained friends with me even when I left them to go to UW. I will cherish the memories of celebrating the passing of qualifying exams with everyone, and the friendships I made during those first two years of graduate school that persist today and continue to grow stronger. To my friends in Seattle, who have been there for me through the ups and downs of trying to conduct research during a pandemic. You served as a constant reminder to value myself as a person independent of my research and my academic career and created so many amazing memories with me. You all are too numerous to name, but I hope you all know how incredible you are, how cherished you are, and how much gratitude I feel for having you all be part of my life.

And lastly, I'd like to thank my partner, Emilee Armstrong, and my dog Chai, who have been some of the most unwavering support systems for me, especially during these last few years of my PhD. Getting a dog was a lifelong dream of mine, and one of the best decisions I've ever made. And to Emilee, who started out as a housemate, then became

a friend, and then became my partner, you help motivate me to constantly strive to be a better person and be the best version of myself I can be. Your constant support has been integral to my achievement of this milestone. I love you so much and can't wait to see what the future holds.

I am truly blessed to have received so much support and guidance from so many different people during the completion of my degree. It has spanned many years and multiple cities, and it is surreal to see it finally coming to an end. I could not have done it without all of you, so from the bottom of my heart, thank you.

Chapter 1. Introduction

1.1 Post-Traumatic Stress Disorder

Post-traumatic stress disorder (PTSD) is one of, if not the most common psychiatric disorder that presents after exposure to and experience of a traumatic event. It has commonly been referred to as a variety of antiquated terms, such as “shell shock” or “battle fatigue”. In the 1980s, it was formally introduced as a disorder in the DSM-III, and since then has become a heavily researched area, particularly with regards to veterans returning from deployment, as well as survivors of sexual violence. Today, according to the American Psychiatric Association, PTSD affects roughly 3.5% of US adults every year, and approximately 8% of adolescents aged 13-18.

In the current DSM-5, the diagnosis of PTSD requires “exposure to actual or threatened death, serious injury, or sexual violence” (American Psychiatric Association, 2013). This may be due to directly experiencing the event, witnessing the event in person, learning that the event happened to a close family member or friend, or due to experiencing repeated exposure to the aversive aspects of a traumatic event. Following experiencing this event, there are four symptom clusters that may manifest. Firstly, the presence of intrusive symptoms associated with the traumatic event, including recurrent, distressing memories of the event, distressing dreams that are similar to the traumatic event, dissociative reactions, also known as flashbacks, to the traumatic event, and marked physiological reactions to cues that are similar to an aspect of the traumatic event. Secondly, there may be a persistent avoidance of stimuli associated with the traumatic event, through avoidance of both distressing memories and of external reminders that may be associated with these distressing memories. Thirdly, there may be negative shifts

in mood associated with experiencing a traumatic event, such as dissociative amnesia, persistent negative beliefs and outlook, feelings of detachment from others, and a persistent inability to experience positive emotions. Lastly, there may be marked alterations in reactivity associated with the traumatic event, including unprovoked outbursts, reckless and self-destructive behavior, hypervigilance, exaggerated startle response, and problems falling and staying asleep. Furthermore, these clusters of symptoms must be present for more than 1 month, cannot be attributable to substance abuse or a medical condition and cause significant distress and impairment in everyday functioning. The DSM-5 also includes a diagnosis for acute stress disorder, which is characterized by stress reactions occurring within the first month following exposure to a traumatic event. While it was intended to be used as a way to identify people who were at high risk of developing PTSD, this has not proven to be particularly predictive (Bryant 2011).

While many people are exposed to traumatic events during their lifetimes, there is a low prevalence rate of PTSD in response to these traumatic events, with rates for women roughly twice as high as men (Bonanno et al., 2015; Kessler et al., 1995). Evidence also suggests that certain traumatic events are more likely than others to cause PTSD, with natural disasters causing significantly lower rates of PTSD than sexual assault and interpersonal violence (Creamer et al., 2001; Forbes et al., 2012; Kessler et al., 1995). There have also been studies reporting higher rates of PTSD in specific ethnic groups, such as in Hispanics and African Americans in the US, although these differences may also be due to socio-economic factors as well as the prevalence of ethnic discrimination (Adams and Boscarino, 2005; DiGrande et al., 2008). Indeed, the risk

factors for developing PTSD include factors such as low socio-demographic background, as well as family history of mental disorders and prior mental disorders (Brewin et al., 2000). Many people suffering from PTSD also display high comorbidity with other disorders, such as depression and substance use disorder (Kessler et al., 1995). Furthermore, greater exposure to traumatic events often results in higher rates of comorbidity in those that develop PTSD.

PTSD is characterized by the dysregulation of fear responses due to abnormal information processing, such as fear overgeneralization (Liberzon and Abelson, 2016). Individuals suffering from PTSD often experience heightened levels of fear in response to cues that remind them of the initial threat. This fear generalization is a critical adaptive behavior to avoid danger in a constantly changing environment. However, excessive fear generalization can cause maladaptive fear responses to innocuous cues and can severely impact daily functioning (Hennings et al., 2020; Siegmund and Wotjak, 2006). In fact, recent studies have shown that generalization in learned contextual fear has greater implications in the etiology of a wide range of PTSD symptoms, such that a safe environmental context may be perceived as a dangerous or threatening context, leading to hypervigilance and exaggerated threat detection (Besnard and Sahay, 2016; Kheirbek et al., 2012; Seo et al., 2021).

The most prevalent theory regarding PTSD involves a model called fear conditioning, by which strong associative learning occurs between cues present at the time of exposure to a traumatic event and the fear response to the traumatic event itself. These associated cues become linked to predicting future threats, and result in output of the same fear responses when exposed to cues that are similar to those that were present

during the trauma (Pitman et al., 2012). Indeed, in clinical studies, it has been reported that PTSD patients fail to perceive both new threats and safe cues accurately, resulting in an impairment in shaping flexible behavioral choices (Liberzon and Abelson, 2016; Lissek et al., 2010). Additionally, hypersensitive and inaccurate fear responses may lead to hypervigilance, due to an inability to accurately attend to threats in various environmental contexts. Recovery from these reactions requires extinction learning, where repeated exposures to the cues associated with the trauma without the consequences of the trauma gradually result in the removal of association of the cues with the traumatic event.

There are several brain regions associated with PTSD that may be involved in this fear conditioning process, including the amygdala, prefrontal cortex, and hippocampus. PTSD has been found to be associated with smaller hippocampus size, although the degree to which this risk factor is predictive is unclear (Smith, 2005). There is also evidence of the same phenomena in other brain regions, primarily those implicated in fear learning (Kitayama et al., 2006). Additionally, previous literature and recent human imaging studies have demonstrated that PTSD patients often show LC hyperactivity (Liberzon and Abelson, 2016; McCall et al., 2015; Valentino and Van Bockstaele, 2008). This type of noradrenergic dysregulation may be key in development of several PTSD-like symptoms, such as re-experiencing of memories, daydreams, and flashbacks associated with the traumatic event (Hendrickson and Raskind, 2016). Currently, treatment options often revolve around modulating this noradrenergic signaling, with prazosin and propranolol, both adrenergic receptor antagonists, having been used in potential treatments of PTSD symptoms and prevention of PTSD (Pitman et al., 2002;

Taylor et al., 2006). However, pharmacological treatments and interventions for PTSD have yielded mixed results, with high potential for adverse side effects and potential relapse following discontinuation of treatment.

Overall, since the introduction of PTSD into the DSM in the 1980s, understanding of the disorder, as well as the neurobiological mechanisms that cause PTSD, has increased exponentially. Several brain regions, such as the dentate gyrus and amygdala, and neurotransmitters, such as norepinephrine, have been implicated in fear conditioning and development of PTSD and PTSD-like symptoms. Despite this, treatment options remain limited, specifically with regards to pharmacological methods. Thus, further work into these areas must be carried out to further our understanding of the neural basis underlying PTSD.

1.2 Dentate Gyrus

The hippocampus is a region of the brain highly linked to learning and memory (Morris, 2006; Squire, 1986). It is divided into the CA1, CA2, CA3, and dentate gyrus (DG) subregions, and the DG, CA1 and CA3 in particular are linked via strong forward connections known as the trisynaptic loop. The DG is also well-known as a site of adult neurogenesis, suggesting a key role in learning and memory (Borzello et al., 2023; Cameron et al., 1993; Kuhn et al., 2018). The DG is composed of three layers: a molecular layer, a granule cell layer (GCL), where adult neurogenesis occurs via development of adult-born granule cells (GCs), and the hilus (Ming and Song, 2011). DG GCs receive strong excitatory inputs from the entorhinal cortex (EC), via both the medial and lateral ECs, in what is known as the perforant path (PP) (Woods et al., 2018). In turn, the DG directs those inputs towards the CA1 region of the hippocampus (Amaral et al., 2007).

These signals are further propagated in the aforementioned trisynaptic loop that affects the processing of circuits that provide inputs to the hippocampus. Within the DG, hilar mossy cells (MCs) receive input from GCs and project to neurons in the molecular layer as well as hilar interneurons, via the associational-commissural pathway (Amaral et al., 2007; Scharfman, 2007; Scharfman, 2016). Additionally, there is some evidence that CA3 pyramidal cells communicate with ventral DG GCs, and that these GCs also communicate with GABAergic neurons in the hilus and CA3 (Acsády et al., 1998; Li et al., 1994; Vivar et al., 2012). Meanwhile, mossy-fiber synapses on CA3 pyramidal cells show high-frequency activity-dependent facilitation, while synapses onto GABAergic interneurons show high initial release probability that is independent of frequency facilitation (Nicoll and Schmitz, 2005; Zucca et al., 2017). This means that higher frequency bursts recruit CA3 pyramidal cells, while lower frequency firing recruits the interneurons, and inhibits CA3 neurons (Henze et al., 2002; Mori et al., 2004).

GC activity in the DG is extremely sparse, with fewer than 5% of GCs active in any given environment during exploration behavior (Chawla et al., 2005; Hainmueller and Bartos, 2018). Typically, DG GCs will fire in response to a specific location, also known as a place field, and many place fields undergo a process called remapping when exposed to similar environments (Danielson et al., 2016). However, when animals are transferred into a different chamber in a different room, a different subset of GCs becomes active, suggesting that there is a graded amount of remapping that occurs based on similarity of environmental contexts (GoodSmith et al., 2017). Additionally, it appears that DG GC place fields remain relatively stable over multiple days, unlike the place fields in CA1 and CA3 (Hainmueller and Bartos, 2018). GCs have also been shown to develop

new place fields when exposed to novel surroundings, through what is theorized to be strengthening of PP input synapses (Diamantaki et al., 2016; Kim et al., 2018; Sheffield et al., 2017).

An area of particular interest with regards to the DG is adult neurogenesis, through which additional granule cells are continuously generated throughout adulthood; the DG is one of the only brain regions in which this type of neurogenesis occurs. These adult-born GCs display heightened excitability and synaptic plasticity and respond more strongly towards external stimuli compared to their mature counterparts, and this appears to be linked with discrimination of similar memories (Denny et al., 2012; Marín-Burgin et al., 2012; Schmidt-Hieber et al., 2004; Zhuo et al., 2016). Following early development, 4- to 6-week-old GCs begin to receive inputs from the LEC and MEC and synapse onto CA3 pyramidal cells and hilar mossy cells (Vivar and van Praag, 2013). During this time, these GCs begin to show enhanced excitability, although they also display less spatial tuning than mature GCs (Danielson et al., 2016).

There are also several GABAergic and glutamatergic inhibitory neuron types in the DG. These include mossy cells, which are glutamatergic interneurons located in the hilar layer (Scharfman, 2016). Mossy cells display excitatory synapses onto other interneurons as well as GCs in the DG, and also contain place fields which change firing rate and location in relation to novelty (Danielson et al., 2017). There are also parvalbumin-expressing interneurons, which inhibit GCs and interneurons, and synchronize network activity during sharp waves-ripples (SWRs), as well as during theta- and gamma-frequency oscillations (Bartos et al., 2002; Szabo et al., 2017). There are also somatostatin-expression interneurons, which inhibit dendrites of GCs and other

interneurons near PP synapses, among other areas (Savanthrapadian et al., 2014). It has also been suggested that somatostatin interneurons play a role in controlling synaptic plasticity (Stefanelli et al., 2016).

Meanwhile, one of the major areas of input into the DG is the entorhinal cortex. The MEC presents spatial information, while the LEC presents non-spatial information to the DG (Hargreaves et al., 2005; Keene et al., 2016). The MEC also contains grid cells and plays a key role in place-field stability in both GCs and CA1 and may also contribute to activation and spatial tuning of GCs as well (Diehl et al., 2019; Mallory et al., 2018). The LEC conveys information relating to time scales, as well as egocentric bearings towards objects and locations (Wang et al., 2018; Ziv et al., 2013). These inputs from the EC are known as the perforant path and play a key role in DG and hippocampal function in memory and learning.

The hippocampus also receives dopaminergic inputs from the ventral tegmental area (VTA) and the locus coeruleus (LC), and also receives noradrenergic inputs from the LC (Seo et al., 2021; Wagatsuma et al., 2018). These projections may help to facilitate memory acquisition and consolidation, as well as contextual discrimination and pattern separation (Seo et al., 2021; Takeuchi et al., 2016). Additionally, LC input has been shown to enhance GC responses to PP input via long-term potentiation (LTP) (Harley et al., 1989). However, the exact relationship between LC-mediated dopamine and norepinephrine on DG function remains unclear.

Thus, many studies have shown that the hippocampus at large is a critical neural structure for processing environmental information during a new episodic event (Lisman et al., 2017; Morris, 2006; O'Reilly and McClelland, 1994). These episodic memories

depict unique experiences, and associate items and events with the spatiotemporal context in which they occurred. In fact, individuals with hippocampal lesions typically display severe memory deficits, particularly related to episodic memories (Nadel et al., 2000). Specifically, these patients struggle with encoding new episodic memories, and recalling the contextual details of previous experiences (Corkin, 2002; Rosenbaum et al., 2000). This is where the DG plays a vital role – association of individuals and places within a contextual domain, and amongst the background details of an experience (Ison et al., 2015; Lisman et al., 2017; McHugh et al., 2007; Miller et al., 2013).

Computational and behavioral studies have further corroborated that the DG has an essential role in this process. This is particularly true when new information is similar to existing knowledge, because the DG engages in sparse coding of incoming information from the entorhinal cortex (EC) (Deng et al., 2013; McHugh et al., 2007; O'Reilly and McClelland, 1994; Treves et al., 2008). During this process, granule cells in the DG send signals to the CA3 region of the hippocampus, where pattern completion, a process that recalls memory through partial cues, occurs (Nakazawa et al., 2002). In this capacity, the DG has been linked to a number of mnemonic functions related to pattern separation, spatial context, and working memory (Lee and Jung, 2017; McNaughton and Morris, 1987; Sasaki et al., 2018; Treves and Rolls, 1994; Xavier and Costa, 2009). The unique anatomical characteristics of the DG have led to the idea that it is a neural structure essential for pattern separation, which is a process that discriminates amongst similar stimuli (Marr, 1971; O'Reilly and McClelland, 1994). Indeed, there have been several models proposed for how the DG can perform pattern separation.

One prevailing theory is that pattern separation occurs via expansion recoding, which was first proposed as a mechanism in the GCL of the cerebellar cortex (Marr, 1969). This theory was then applied to the GCL of the DG (McNaughton and Morris, 1987; Myers and Scharfman, 2011). In expansion recoding, GCs, which receive only a small number of synaptic inputs, fire very sparsely in response to these inputs. Thus, overlapping responses are represented as orthogonal representations in the GCL, increasing the ability of the GCs to learn and store information in a variety of different contexts. Through distinguishing these output representations from their input representations via recruitment of distinct populations of GCs, it becomes possible to recall and disambiguate highly similar experiences from one another (Yassa and Stark, 2011).

Another role of the dentate gyrus is as a site for processing and associating incoming sensory information. The hippocampus receives segregated, parallel processing streams from the medial and lateral EC, which are theorized to process different types of information (Knierim et al., 2006; Nilssen et al., 2019). While LEC activity is thought to convey the content of an experience, MEC activity is thought to convey the context of an experience (Knierim et al., 2014). Thus, by converging in the DG, these two distinct streams are able to combine their information, leading to what is called the binding theory. This binding theory proposes that one of the roles of the DG is to provide highly selective responses to events occurring in specific contexts based on perforant path input, which is key to forming distinct memories for similar experiences.

Additionally, the gate hypothesis suggests a role for local interneurons in the DG, through which GCs are inhibited by local interneurons that are engaged by both

feedforward and feedback inputs from the ECs, GCs, and MCs (Ewell and Jones, 2010; Scharfman et al., 1990). Thus, only extremely potent entorhinal inputs activate GCs, which over time results in LTP of specific EC-GC synapses and weakening of other inputs in the perforant path. Through this strengthening and weakening of specific synapses, distinct subsets of GCs may be reactivated for previous experiences or recruited to distinguish between similar experiences.

The DG also demonstrates high plasticity during learning and memory and generates engrams, physical changes in the brain that support recall (Josselyn et al., 2015). These engrams are created by physiological changes during learning, through which populations of GCs are engaged during recurrence of different experiences, and by which re-activation is sufficient to elicit behavioral outcomes (Hainmueller and Bartos, 2020; Sun et al., 2020). This theory posits that different learned experiences re-engage distinct populations of neurons in the DG, which results in recall of previous similar experiences. There is also evidence that the DG makes use of adult neurogenesis to tune immature adult-born GCs to specific experiences (Miller and Sahay, 2019; Teyler and DiScenna, 1986). Once these neurons mature, they are specifically activated by future instances of similar experiences, resulting in indexing of distinct populations of DG neurons towards specific memories. Additionally, recent evidence shows that this may be facilitated by gradual activity changes in these DG granule cells, rather than by completely distinct sets of neurons (Hainmueller and Bartos, 2018; Senzai and Buzsáki, 2017).

There is also an element of temporal dynamics that may help facilitate distinct representations of contextual and environmental information in the DG. It has been suggested that temporally selective encoding in the DG may allow for preferential

encoding of information present during formation and development of immature, adult-born GCs (Rangel et al., 2014). These neurons may be tuned to temporally proximal events during their development, and the constant turnover and emergence of new GCs results in an enhanced ability to engage temporally distinct populations of GCs. This aligns with the notion that immature adult-born GCs show enhanced excitability but less spatial tuning than mature GCs (Danielson et al., 2016).

In order to study DG pattern separation, contextual discrimination learning is often used (Seo et al., 2021). The hippocampus has been implicated in aversive contextual learning and this type of pattern separation may also rely on inputs and activity of MEC neurons and PP axons (Fanselow, 2000; Kitamura et al., 2015). It has also been suggested that DG-mediated pattern separation may play a role in both encoding and recall of contextual fear conditioning related information (Baker et al., 2016; Bernier et al., 2017). Thus, it is likely that DG output is necessary for successful contextual discrimination at multiple stages of memory. Another paradigm often used in studying the DG is location discrimination learning, which requires pattern separation processes to distinguish between distinct locations within an environment (Clelland et al., 2009). Similar to contextual discrimination, adult-born GCs are required in this process, and formation of precise location-based memories requires mapping of cues to a spatial representation (Lee and Jung, 2017).

Lastly, the DG has also been the subject of something known as novelty detection theory, wherein the DG plays a key role in the encounter of new experiences, or when new information must be incorporated into previous experiences. Responses in the DG are then modulated by influences such as norepinephrine, which has a role in fearful and

novel experiences (Amaral and Campbell, 1986; Hunsaker et al., 2008; Prince et al., 2016). Moreover, during new experiences, DG GCs and MCs demonstrate enhanced excitatory responses to EC inputs, as well as enhanced LTP of EC projections onto GCs (Harley, 2007). This increased activity during new experiences suggests that the DG is heavily involved in processing novelty.

To date, there exist several theories as to how the DG works to modulate pattern separation, episodic memories, and contextual learning. However, the exact mechanisms by which the DG functions in these tasks remains unclear, with uncertainties arising regarding the distinct phases of memory that the DG is engaged in, as well as how spatiotemporal dynamics of DG ensembles are involved. Further research must be done to further elucidate DG function and the corresponding behavioral outputs and enhance our understanding of DG influence upon learning and memory.

1.3 Locus Coeruleus and Norepinephrine

With regards to behaviors involving novelty, attention and memory, and arousal, the locus coeruleus (LC) plays a key role (Berridge and Waterhouse, 2003; Schwarz and Luo, 2015). The LC, also known as the 'blue spot', is a small brain region located in the brainstem, and traditionally has been viewed as a largely homogenous structure, whose main purpose is the production of norepinephrine (NE) in the mammalian brain and the distribution of NE via extensive projections throughout the brain (Aston-Jones and Bloom, 1981; Poe et al., 2020; Robertson and Plummer, 2013). Norepinephrine is one of the four main neuromodulators in the brain and is responsible for regulating a variety of behavioral and sensorimotor functions (Breton-Provencher et al., 2021). Because of its small size and shape, the LC has proven challenging to discreetly target, and manipulations of LC

projections may target multiple brain regions. However, as this brain region garners more interest, more research is uncovered that furthers our understanding of its many diverse roles in behavior.

There are approximately 3,000 LC neurons in the rodent brain, and approximately 50,000 in the human brain, making the LC an extremely small brain region (Sara, 2009; Sharma et al., 2010). While all LC neurons contain NE, two distinct types of NE cells, large multipolar and smaller fusiform cells, have been observed (Grzanna and Molliver, 1980; Swanson, 1976). While both are present throughout the LC, fusiform cells appear to be located more prominently in the dorsal LC, while multipolar cells are more plentiful in the ventral LC (Swanson, 1976). In addition, there is high expression of galanin in LC neurons, which is responsible for modulating wake/sleep states, nociception, and feeding (Holets et al., 1988; Lang et al., 2015). There are also smaller amounts of expression of Neuropeptide Y, dopamine, brain-derived neurotrophic factor (BDNF), and other co-transmitters located in LC-NE neurons (Castren et al., 1995; Holets et al., 1988; Koylu et al., 1999). LC neurons also contain several adrenergic receptor (AR) subtypes, as it is itself responsive to NE release (Young 3rd and Kuhar, 1980). Of these subtypes, α_2 is the most abundant in the LC. In total, there are nine known AR subtypes: α_{1A}, α_{1B}, α_{1D}, α_{2A}, α_{2B}, α_{2C}, β_1, β_2, and β_3 (Strosberg, 1993). These AR subtypes are found across the brain and spinal cord on neurons, glia, immune cells and brain vasculature, and further work must be done to characterize the density and distribution of these subtypes (MacDonald and Scheinin, 1995; Molinoff, 1984). LC neurons also express receptors for a variety of other neurotransmitters and neuropeptides, including opioid receptors (Mansour et al., 1994). Local LC circuits extend into a pericoerulear (peri-LC) region, which also contains

GABAergic, glutamatergic, neuropeptide-S-expressing, and cholinergic neurons (Boucetta et al., 2014; Cox et al., 2016; Xu et al., 2004). GABAergic neurons in the peri-LC area inhibit LC-NE activity and are highly active during wakefulness (Breton-Provencher and Sur, 2019, Cox et al., 2016).

Nearly all brain regions receive projections from the LC, with notable exceptions including the nucleus accumbens and substantia nigra, which by contrast receive dense dopaminergic inputs. LC neurons have been shown to collateralize throughout the brain, even across long distances, although this work primarily has been limited to two brain regions at a time (Nagai et al., 1981). Recent studies have also begun to delve into potential functional heterogeneity within the LC, with optogenetic activation of differing populations of LC neurons able to modulate distinct behaviors in rodents (Hickey et al., 2014). Meanwhile, LC neurons projecting to forebrain regions such as the hippocampus are primarily located in dorsal LC, while cerebellum- and spinal cord-projecting LC neurons are more commonly found in ventral LC. Additionally, there appears to be output-specific organization along the anterior-posterior axis (Schwarz et al., 2015). Further coordination of LC projections has been seen in the anterior cingulate and amygdala in coordinating aversion and anxiety, as well as in the spinal cord to promote analgesia (Hirschberg et al., 2017; McCall et al., 2017; Uematsu et al., 2017; Waterhouse and Chandler, 2016). There have also been studies implicating LC-NE in motor function (Zerbi et al., 2019). However, there is still much that remains unknown regarding LC heterogeneity, and recent developments in scientific tools may help answer more of these questions.

The LC also receives inputs from many distinct brain regions, although the exact number is unclear (Cedarbaum and Aghajanian, 1978; Schwarz et al., 2015). The peri-LC has long been an area of focus regarding local regulation of LC activity (Breton-Provencher and Sur, 2019; Shipley et al., 1996). Brainstem inputs to the LC have also been postulated to result in LC activation following salient stimuli, while inputs from prefrontal cortex and amygdala may modulate the intensity of LC activity (Jones and Yang, 1985; McCall et al., 2015). Additionally, LC neurons appear to be innervated by regions in the forebrain, with inputs to peri-LC distinct from inputs to the LC core (Breton-Provencher and Sur, 2019; Luppi et al., 1995).

LC neurons also appear to undergo postnatal development, with LC responsiveness to somatosensory stimuli enhanced in newborns, which may contribute to infantile safety and threat learning, and more tuned towards noxious stimuli in later life (Debiec and Sullivan, 2017; Nakamura, 1987). LC neurons during early development also appear to have slower conduction velocities, as well as synchronized activity until postnatal day 21 (Christie, 1997; Marshall et al., 1991). Additionally, the LC-NE system may play a role in protecting and preserving other neurons, as NE denervation has been shown to reduce BDNF protein and activate TrkB receptors in the ventral midbrain (Hassani et al., 2020).

It has also been suggested that LC-NE systems are important in modulating synaptic plasticity, strengthening connectivity in order to mediate adaptive learning (Bezin et al., 2000). This is supported by findings that LC is involved in habituation, long-term depression, and depotentiation (Hagena et al., 2016; Poe et al., 2010; Vankov et al., 1995). One method by which LC-NE may influence neural circuitry is through glutamate

amplification, in which LC-NE mediated activity is modulated by glutamate activity (Mather et al., 2016). In this model, glutamate circuits compete for resources, with suppression and enhancement of losing and winning circuits dependent upon NE concentrations, leading to salient inputs becoming prioritized.

Behaviorally, LC-NE has been shown to modulate arousal and wakefulness via firing rate (Carter et al., 2010; Foote et al., 1980). Arousal and vigilance states are one of the primary outputs of LC-NE activity, with LC-NE neurons largely silent during REM sleep, and demonstrating high activity during wakefulness (Aston-Jones and Bloom, 1981; Swift et al., 2018). Additionally, the LC has been implicated in stress-related behaviors (Berridge and Waterhouse, 2003; McCall et al., 2015). These behaviors appear to be differentially modulated by tonic and phasic firing, where tonic activity is exemplified by low rates of firing (0.1-5 Hz), and phasic bursting is characterized by 10-20 Hz bursts of activity (Devilbiss and Waterhouse, 2011). Tonic activity has been implicated in arousal levels and wake/sleep states, while phasic bursting is often triggered by novel or salient stimuli (Aston-Jones and Bloom, 1981; Berridge and Waterhouse, 2003; Foote et al., 1980). However, uncontrolled LC-NE firing leads to high anxiety states, and there exists an inverted-U-relationship between brain function and NE activity levels (Aston-Jones and Cohen, 2005; McCall et al., 2015; Valentino and Van Bockstaele, 2008).

The role of the LC-NE system extends beyond arousal and attention; indeed, it also plays a role in learned behaviors and cognition (Bouret and Sara, 2004). It has been shown that blockade of LC activity diminishes reward seeking behaviors, while increases in LC firing rate are associated with behavioral responses in operant conditioning (Jahn et al., 2018; Varazzani et al., 2015). LC-NE is also heavily implicated in learning and

memory, with projections to the hippocampus, amygdala, and prefrontal cortex (Kempadoo et al., 2016; McCall et al., 2017; Takeuchi et al., 2016; Uematsu et al., 2017; Wagatsuma et al., 2017). Projections to prefrontal cortex have been implicated in 'executive' functions including attention and working memory, and projections to the amygdala have been implicated in emotional memory (Arnsten, 2011; McGaugh, 2004). These attention-based processes work through the inverted-U-shaped curve, where moderate NE concentrations lead to optimal results, with deviations from this resulting in decreasing effectiveness (Berridge and Spencer, 2016). Furthermore, LC neurons appear to be involved in learning during conditioning tasks, responding to novel stimuli and rewards, or changes that require behavioral adaptation (Aston-Jones et al., 1999; Sara and Segal, 1991). Phasic bursting during task-related decision making has also been observed, with strong correlations to effort in the task (Kalwani et al., 2014; Varazzani et al., 2015).

Meanwhile, projections to the hippocampus have been found to be active during spatial memory tasks, as well as in discrimination and navigation-based tasks (Glennon et al., 2019; Kaufman et al., 2020). This LC-NE modulation may also be due to concentration-dependent effects, where phasic and tonic LC firing may lead to differential outcomes (Grella et al., 2019). Moreover, NE release in the hippocampus results in enhancements to contextual learning and everyday memory, as well as changes in synaptic plasticity via β-AR dependent modulation (Hansen and Manahan-Vaughan, 2015; Takeuchi et al., 2016; Wagatsuma et al., 2018). The DG in particular receives dense neuromodulatory input from NE cell projections in the locus coeruleus (Blackstad et al., 1967). The LC is highly active during stressful events in rodents and primates and

promotes behavioral responding under a gradient of arousal states (McCall et al., 2015; Valentino and Van Bockstaele, 2008). Physiological studies suggest that NE is involved in perforant path synaptic plasticity via modulating neuronal activities of dentate granule cells and/or local interneurons. This supports the hypothesis that the LC-NE system plays a role in DG-dependent learning and memory (Harley, 2007; Rose and Pang, 1989; Seidenbecher et al., 1997; Seo et al., 2021; Walling and Harley, 2004). It has also been hypothesized that LC-NE activity may influence learning via encoding of environmental novelty, where increases in LC activity are associated with novel and salient stimuli (Breton-Provencher and Sur, 2019; Takeuchi et al., 2016;).

There are several theories regarding the role of LC in behavior. The first, adaptive-gain theory, suggests that phasic activity is responsible for optimal behavioral performance and facilitates decision-making processes, while tonic firing increases the gain of a network, leading to poor performance due to over responsiveness to stimuli (Aston-Jones and Cohen, 2005; Usher et al., 1999). Through this tradeoff between phasic and tonic firing, LC-NE undergoes adaptive gain, and optimizes behavioral switches between exploitation and exploration behaviors. This model places high emphasis on the temporal dynamics of LC activation to drive optimal behavior. A similar model emphasizes the different affinities of NA receptors in driving optimal performance, wherein intermediate levels of NE bind to high-affinity α_2-ARs in support of executive functions, and higher concentrations of NE result in activation of α_1- and β-ARs to promote flight-or-flight behaviors (Arnsten, 2000; Arnsten, 2011). Another prevailing theory is the network reset theory, which suggests that LC-NE neurons are activated in contexts that necessitate a change in behavior (Bouret and Sara, 2005; Yu and Dayan, 2005). In these

contexts, LC-NE neurons induce widespread arousal and reset network activity to enable an update of priors (Yu and Dayan, 2005). This prioritizes bottom-up signals, enabling learning and behavioral optimization.

Recently, more work has been done that increasingly supports the functional heterogeneity of LC organization, suggesting that LC function may be more complex than initially theorized. These findings suggest that although all LC neurons are involved in arousal, distinct groups of LC neurons may have differing functions, resulting in highly specific targeting of downstream brain regions to modulate behavioral outputs. However, further research must be done using newer, more precise approaches to explore LC activity and dynamics during different sensory and behavioral contexts and provide insights into the influence of LC-NE in functions including cognition, attention, and learning, while overcoming the unique challenges of LC characterization.

Chapter 2. LC-DG Circuit Excitation and Inhibition Drive Opposing Learning States

2.1 Introduction

Post-traumatic stress disorder (PTSD) and other anxiety disorders are commonly characterized by the dysregulation of fear responses due to abnormal information processing, such as fear overgeneralization (Liberzon and Abelson, 2016). This fear generalization is a critical adaptive behavior to avoid danger in a constantly changing environment. However, excessive fear generalization can cause maladaptive fear responses to innocuous cues and can severely impact daily functioning (Hennings et al., 2020; Siegmund and Wotjak, 2006).

Many studies have shown that the hippocampus is a critical neural structure for processing environmental information during a new episodic event (Lisman et al., 2017; Morris, 2006; O'Reilly and McClelland, 1994). Computational and behavioral studies have suggested that the dentate gyrus (DG), a subregion of the hippocampus, has an essential role in this process. The unique anatomical characteristics of the DG have led to the idea that it is a neural structure essential for pattern separation, which is a process that discriminates amongst similar stimuli (Marr, 1971; O'Reilly and McClelland, 1994). However, it is currently unknown how specific neuromodulators alter DG activity during aversive experiences and contribute to overgeneralization of fear.

The DG receives dense neuromodulatory input from norepinephrine (NE) cell projections in the locus coeruleus (LC) (Blackstad et al., 1967). Furthermore, the LC is highly active during stressful events in rodents and primates and promotes behavioral responding under a gradient of arousal states (McCall et al., 2015; Valentino and Van Bockstaele, 2008). Physiological studies suggest that NE is involved in perforant path

synaptic plasticity via modulating neuronal activities of dentate granule cells and/or local interneurons. This supports the hypothesis that the LC-NE system plays a role in DG-dependent learning and memory (Harley, 2007; Rose and Pang, 1989; Seidenbecher et al., 1997; Walling and Harley, 2004).

Despite these converging lines of molecular and physiological data, the precise relationship between the function of the DG, and neuromodulation by the LC-NE system in processing fear-related information remains unclear. In this chapter, I use an integrated neuromodulatory circuit analysis approach, combining viral tracing, optogenetic tools, and a well-established Pavlovian contextual fear discrimination (CFD) paradigm in which animals were placed in two similar, but different, contexts daily to further elucidate the relationship between the LC-NE system and DG-dependent contextual processing in anxiety and stress-related disorders (Danielson et al., 2016; Lovett-Barron et al., 2014; McHugh et al., 2007).

2.2 Methods

2.2.1 Animals

Adult (25-35 g) male *TH*-IRES-Cre mice and Cre (-) littermate control mice were used for projection mapping and *in vivo* experiments after backcrossing to C57BL/6J mice for at least 10 generations. Mice were group housed, given access to food pellets and water *ad libitum*, and maintained on a 12:12-hour light/dark cycle (lights on at 7:00 a.m.). Animals were held in a sound attenuated holding room facility in the lab starting at least one week prior to surgery, as well as post-surgery and throughout the duration of behavioral assays to minimize stress from transportation and disruption from foot traffic. All mice were handled and, where appropriate, connected to fiber optics two times a day

for one week prior to behavioral experimental testing. All experimental procedures were approved by the Animal Care and Use Committee of Washington University and the Animal Care and Use Committee of University of Washington and conformed to NIH guidelines.

2.2.2 Stereotaxic surgery

All surgeries were performed under 4% isoflurane anesthesia (Piramal Healthcare, Maharashtra, India). For initial projection mapping, adult male mice were injected unilaterally with 800 nl of AAV5-EF1α-DIO-ChR2-eYFP virus (WUSTL Hope Center Viral Core, St. Louis, MO) into the LC (AP: -5.44 mm, ML: +1.25 mm, DV: -3.8 mm) using a Hamilton syringe with beveled needle (Reno, NV). For retrograde tracing, 300-400 nl of Cholera Toxin B (CTB), rAAV2-retro was injected into the DG (AP: -2.2 mm, ML: +1.4 mm, DV: -2.1) using a Hamilton syringe with blunted needle. For functional LC-DG necessity and sufficiency behavior experiments, adult male mice were injected bilaterally with 800 nl of AAV5-EF1α-DIO-ChR2-eYFP, or AAV5-EF1α-DIO-ArchT-eGFP virus (WUSTL Hope Center Viral Core, St. Louis, MO) into the LC (AP: -5.45 mm, ML: ±1.25 mm, DV: -3.8 mm) using a Hamilton syringe with a beveled needle. For transgenic controls, adult mice were injected bilaterally with 800 nl of AAV5-EF1α-DIO-eYFP into the LC (AP: -5.45 mm, ML: ±1.25 mm, DV: -3.8 mm) using a Hamilton syringe with a beveled needle. Four to five weeks after virus injection, fiber optic ferrules were chronically implanted above the DG (AP: -2.2 mm, ML: ±1.4 mm, DV: -1.65 mm), and dental cement (Lang Dental, Wheeling, IL) was applied to hold the ferrules in place. Mice were allowed to recover for at least six weeks following infusion of virus prior to further behavioral

testing or perfusion for projection mapping to ensure optimal viral expression and implant placement location (**Fig. S2A**).

2.2.3 Contextual fear discrimination behavioral task

We used a well-established Pavlovian contextual fear discrimination (CFD) paradigm in which animals were placed in two similar, but different, contexts daily (Danielson et al. 2016; Lovett-Barron et al., 2014; McHugh et al., 2007). Fear conditioning took place in Med-Associates conditioning chambers that consisted of one clear plexiglass wall, three aluminum walls, and a stainless-steel grid as a floor. The training chamber was housed in a sound attenuated cubicle. The conditioning chambers could be configured into three distinct contexts: A, B, and C. Context A was rectangular, with floors made of stainless-steel rods (2 mm diameter, spaced 5 mm apart), walls of aluminum and acrylic, and cinnamon extract scent, and was cleaned with 70% ethanol between runs. Context B differed from context A in that it had a white acrylic floor and a wall decorated with a black and white striped pattern. Context B was cleaned with multi-purpose surface cleaner (Method, UPC: 817939000106) between runs, and scented with peppermint extract. Context C also had a white acrylic floor, however it differed from context B in that the chamber walls were covered with circular plastic inserts, and the cubicle fan was turned off. Context C was cleaned with multi-purpose surface cleaner (Method, UPC: 817939000106) between runs, and scented with peppermint extract. All sessions were recorded from the side using a digital camera and were scored for freezing by an investigator blind to the genotype of the animal.

Mice were handled for 5 minutes per day for a week prior to training. Contextual fear discrimination training took place in the apparatus described above. In context A

(unsafe context), animals were placed in the conditioning chamber and allowed to freely explore for 180 seconds, after which they received a single 2 second foot shock of 0.50 mA. Mice were taken out 15 seconds after termination of the foot shock and returned to their home cage. In context B (safe context), mice were allowed to freely explore the context for 197 seconds, the same amount of total time that they were in context A, and then returned to their home cage. In this context, no foot shock was delivered. All freezing in both contexts was assessed for the first 180 seconds, and the last 17 seconds were not included in the behavioral analysis. Freezing was done in a double-blind fashion to avoid bias in manual scoring.

On the first day (Day 0) of CFD training, all animals were placed in context A and received a foot shock. The next day (Day 1), for LC-DG activation (**Fig. 2.2C**) experiments, mice were run first in context B with no foot shock, then in context A with a foot shock. There was a minimum 3-hour period between exposure to context A and context B. This training protocol was repeated daily for 9 days. For the LC-DG inhibition (**Fig. 2.2F**) experiment, the order of the exposed contexts (A and B) during training was randomized to make the training more challenging. For the discrimination training (**Fig. S1M, Fig. S1P**), the training procedure followed the same schedule as the LC-DG activation or inhibition experiments, with context C (dissimilar context) replacing context B.

For the stress-modulated CFD training (**Fig. 2.2G-I**), mice were immobilized in modified disposable conical tubes once for 5 minutes and were then immediately transferred to their home cages. Animals were subjected to CFD as described above. To evaluate whether the stress-induced behavioral outcome was due to cognitive impairment

or changes in pain sensitivity, the unconditioned response to foot shock was assessed by estimating horizontal distance traveled during the shock. Horizontal distance was estimated by quantifying crossings of a 4-cell grid superimposed over the conditioning chamber (**Fig. S1K**).

2.2.4 Optogenetic manipulation of LC-DG circuit

Following stereotaxic surgery and implantation of a fiber optic implant above the DG, mice were connected to either a 473 nm or 532 nm diode-pumped solid-state laser (OEM Laser Systems). Laser power was adjusted to obtain ~15 mW transmittance into the brain. For excitation of the LC-DG circuit using ChR2, 473 nm wavelength light was used at 8 Hz frequency, while for inhibition of the LC-DG circuit using ArchT, 532 nm wavelength light was used continuously.

For optogenetic controls during behavior tests, a rotating optical commutator (Doric) was positioned on top of the training chamber and connected to a 473 nm or 532 nm diode-pumped solid-state laser (OEM Laser Systems; see **Fig. 2.1A, 2.2D, 4.2E, 4.2H**). Fibers were attached to the implants on the mouse for every training session.

2.2.5 Statistical analysis

All data are expressed as mean ± SEM. Behavioral data were analyzed with JMP12 Pro (SAS institute, Cary, NC, RRID:SCR_014242) and GraphPad Prism 8.0. *Student's t*-test, one-way or two-way ANOVAs were used to analyze between-subjects designs. Repeated-measures designs were analyzed using mixed-effects restricted maximum likelihood (REML) model. Tukey was used for *post-hoc* pairwise comparisons. The null hypothesis was rejected at the $p < 0.05$ level. Statistical significance was taken

as *p < 0.05, **p < 0.01, ***p < 0.005, *n.s.* represents not significant. All statistical information is listed in Table S1.

2.3 Results

The LC is highly active during stressful events, so we first photo-activated LC-DG projections during CFD training. Cre-recombinase dependent viral vectors containing the light-sensitive cation channel channelrhodopsin-2 (ChR2) were injected unilaterally into the LC of Th-cre mice (**Fig. 2.1A**). We have previously reported that >98% of ChR2-eYFP cells in the LC of Th-cre mice co-express dopamine-beta-hydroxylase, the precursor for

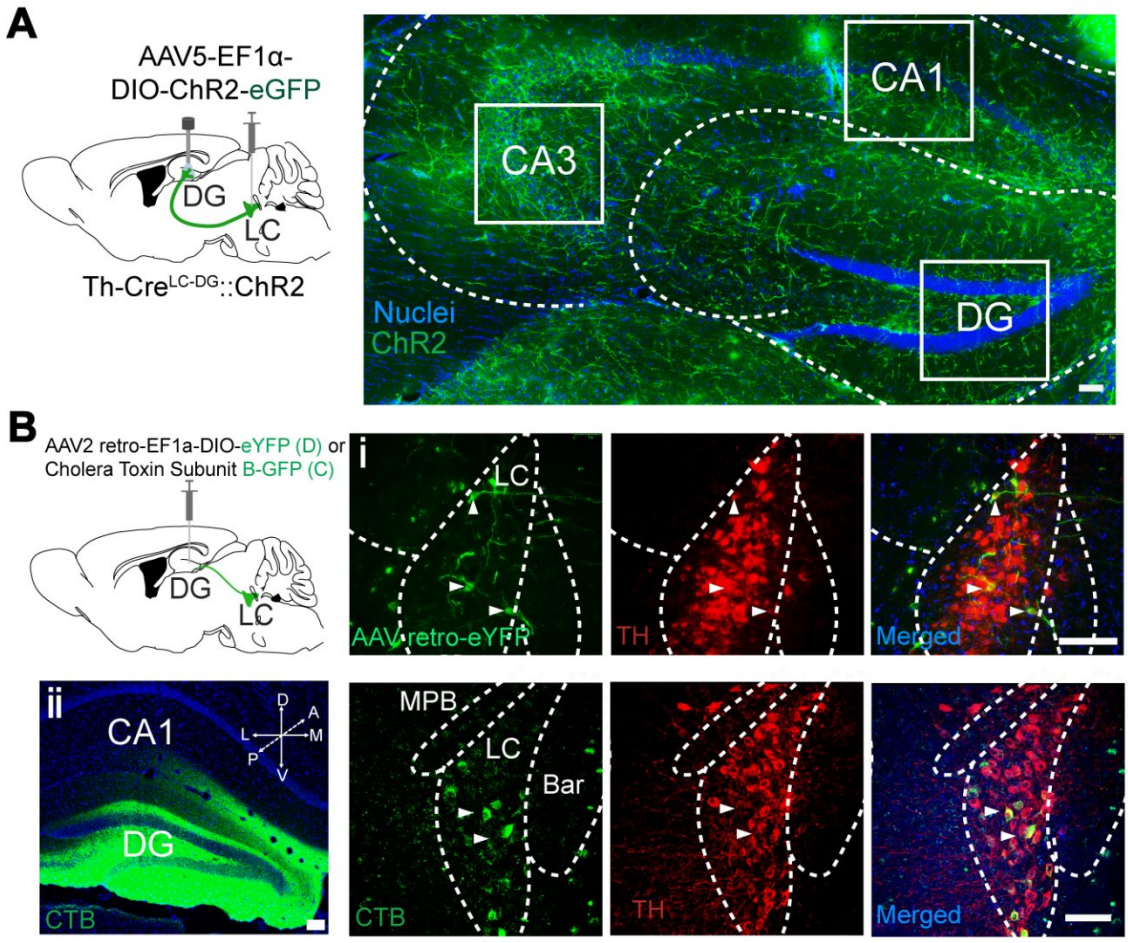

Figure 2.1. Viral tracing of LC-DG noradrenergic circuitry
(**A**) Schematic of experimental approach depicts infection of locus coeruleus-norepinephrine (LC-NE) cells using Th-Cre mouse line with channelrhodopsin (Th-Cre$^{LC\text{-}DG}$::ChR2). ChR2^{+} fibers indicate axons in the dorsal hippocampus originating from the TH^{+}-LC cells. Scale bar = 50 µm. (**B**) Retrograde tracing from the DG using Retro-AAV (top) or Green-CTB (bottom). Arrows indicate cells projecting to the DG that coexpress with TH. Scale bars = 100 µm.

NE synthesis (McCall et al., 2015). To examine the axonal projection of the ChR2$^+$ LC cells into the hippocampus, we imaged ChR2-eYFP-expressing fibers and quantified the density of the ChR2$^+$ axons in the sub-regions of the hippocampus. ChR2$^+$ LC fibers were observed throughout dorsal hippocampus (**Fig. 2.1A-B**). The major sub-regions of the hippocampus (DG, CA1, and CA3) showed similar density of ChR2$^+$ fibers (**Fig 2.2A**). To anatomically confirm the LC to DG projection circuit and potential tropism issues, we conducted a series of complimentary retro-viral tracing techniques, injecting either Cholera Toxin B subunit (CTB) or a retrogradely trafficked adeno associated virus (AAV) into the DG (Tervo et al., 2016). This DG-specific retrotracing revealed that Th$^+$ LC neurons are indeed a pre-synaptic input (**Fig. 2.1B**).

To mimic the 'high-tonic' LC cell firing that occurs in stressful events (McCall et al., 2015; Valentino and Van Bockstaele, 2008), 8 Hz-pulsed photostimulation was delivered bilaterally above the DG during contextual fear conditioning (**Fig. 2.2B**). A control group of mice (ChR2(-)) lacking Cre-recombinase and mice with acute activation of the LC-DG projection (Th-Cre$^{LC\text{-}DG}$::ChR2) were tested in this paradigm. Freezing levels between context A (unsafe) and context B (safe) were compared for both groups of mice across training days 1, 5, and 9 to reveal interactions between optogenetic treatment and contexts across CFD training. While no differences between Th-Cre$^{LC\text{-}DG}$::ChR2 and ChR2(-) mice were present in the beginning of training paradigm, there were significant and robust differences in freezing behavior at the end of training (**Fig. 2.2C**). Only the control group of animals successfully discriminated between the two similar contexts, while Th-Cre$^{LC\text{-}DG}$::ChR2 animals demonstrated impaired performance in discrimination on days 5 and 9 of training. Comparison of freezing levels for all training days showed a

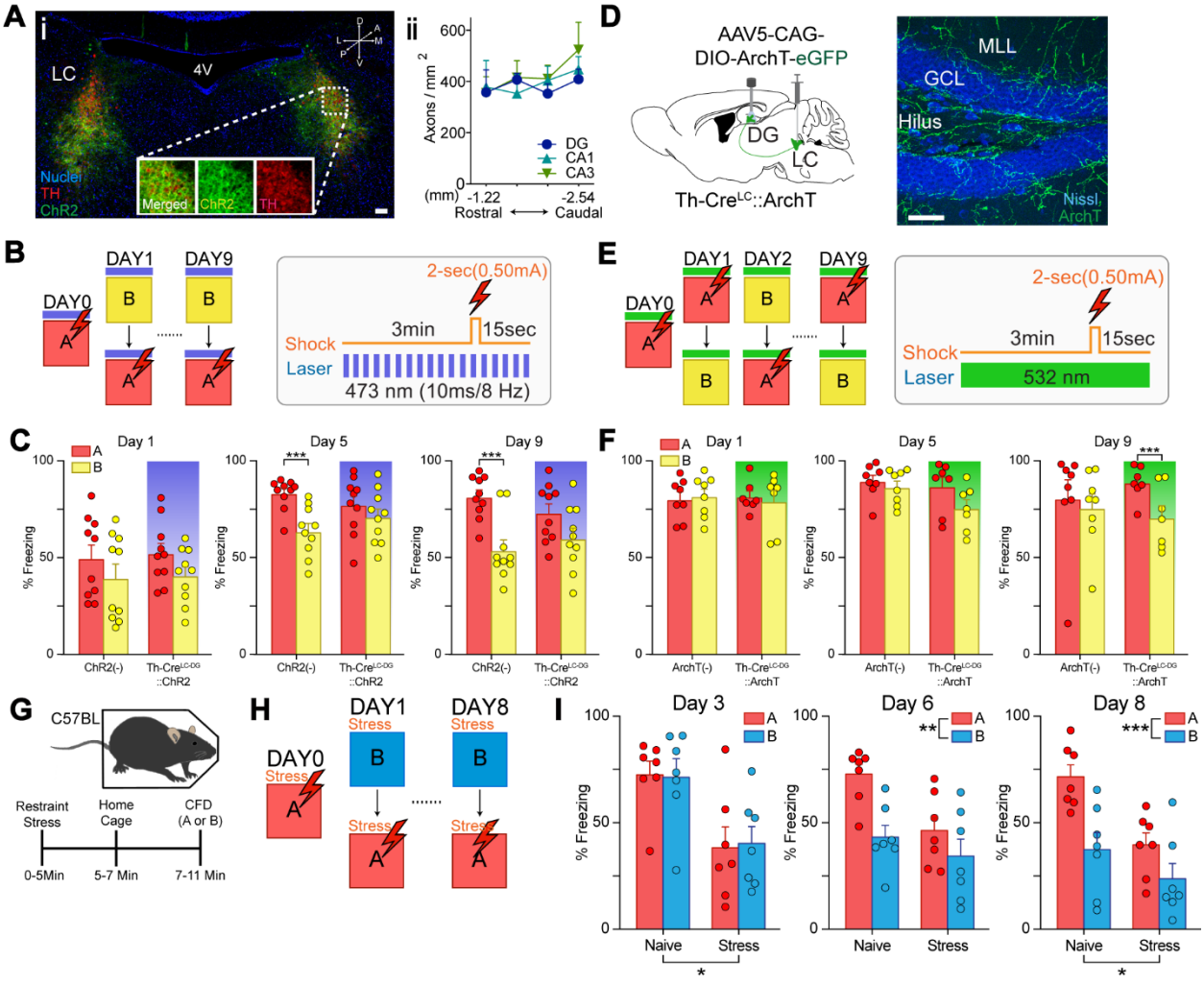

Figure 2.2. Optogenetic manipulation of the LC-DG circuit in contextual fear discrimination. (**A**) ChR2-expressing LC-NE cells coexpressed tyrosine hydroxylase (TH). Scale bar = 100 µm. The density of ChR2$^+$ fibers in the DG in hippocampal subregions: dentate gyrus (DG), CA1, and CA3. (**B**) CFD task with optogenetic activation of the LC-DG projection. Animals received a shock in context A (red), but not in context B (yellow) for nine days (left). Pattern of laser stimulation and shock (only in context A) during CFD (right). (**C**) Acute activation of the LC-DG projection impairs behavioral pattern separation in mice expressing ChR2 in LC-DG projections (Th-Cre$^{LC\text{-}DG}$::ChR2, n = 10), but not in wild-type controls (ChR2(-), n = 10). ChR2(-) controls were able to discriminate on the fifth and ninth days of training, while Th-Cre$^{LC\text{-}DG}$::ChR2 could not discriminate on those days. Both groups received optogenetic light during trial, shaded bar denotes successful stimulation of opsin. (**D**) Schematic of experimental approach depicts infection of LC-NE cells using Th-Cre mouse line with archaerhodopsin (Th-Cre$^{LC\text{-}DG}$::ArchT). Expression of ArchT in the DG regions (right). Scale bar = 50 µm. (**E**) CFD task with optogenetic inhibition of the LC-DG projection. Animals received a shock in context A (red), but not in context B (yellow) for nine days (left). Pattern of laser stimulation and shock (only in context A) during a CFD session (right). (**F**) Acute inhibition of LC-DG projection resulted in enhancement of behavioral pattern separation in mice expressing ArchT in LC-DG projections (Th-Cre$^{LC\text{-}DG}$::ArchT, n = 8), but not in wild-type controls. Both groups received optogenetic light during trial, shaded bar denotes successful stimulation of opsin. (**G**) Depiction of experimental protocol. Wild-type mice either received restraint stress or were handled normally for approximately 5 minutes, then placed back in the home cage for another 5 minutes prior to contextual fear discrimination (CFD) training. (**H**) CFD task with restraint stress administration replacing optogenetic activation. (**I**) Analysis of progressive days of training show that naïve animals successfully began to discriminate context A from context B, while stress-treated animals were unable to successfully discriminate. Additionally, stress-treated animals showed significantly lower freezing levels than naïve animals in the early part of training. However, significant differences are seen at the end of training. All data are mean ± SEM. *$p < 0.05$, ***$p < 0.005$.

Additionally, there were no significant differences in freezing in context A when comparing wild-type controls to Th-Cre$^{LC\text{-}DG}$::ChR2 mice. These results suggest that activation of LC-DG projections facilitates contextual fear generalization without affecting the ability to learn the aversive association. This fear generalization persisted even when animals were subjected to CFD training using two very different contexts (**Fig. S1M-Q**) and was likely not due to differences in basal anxiety level of the transgenic background (**Fig. S2B-E**). By comparison, mice injected with a control fluorophore showed freezing levels similar to ChR2(-), indicating that differences in freezing levels were not due to the viral injection procedure (**Fig. S1E-G**). Further, when contexts were presented in a randomized order, animals again showed an impairment of CFD throughout training with the LC activation (**Fig. S1P-Q**). These results indicate that the LC-DG circuit is associated with disambiguating similar contexts (**Fig. S1M-O**).

Next, to test whether the LC-NE system is necessary for modulating DG function in contextual fear discrimination, we optogenetically inhibited LC-DG projections using archaerhodopsin (ArchT), a light-sensitive proton pump (**Fig. 2.2D**) (Han et al., 2011). To engage the facilitation effect of discrimination, the contextual fear conditioning paradigm was made more difficult by randomizing the order of the two similar contexts (**Fig. 2.2E**). With this randomly ordered CFD task, there were no significant differences through the middle phase of training, likely due to the removal of the predictive cue of daily context order. However, by the end of training, there was a significant difference in behavior between wild-type controls (ArchT(-)) and mice with acute inhibition of the LC-DG projection (Th-Cre$^{LC\text{-}DG}$::ArchT) (**Fig. 2.2F**). In this CFD paradigm, control groups of mice struggled to discriminate between the two similar contexts, while Th-Cre$^{LC\text{-}DG}$::ArchT mice

froze significantly more in context A (unsafe) than in context B (safe). Freezing levels between context A and B were compared across all training days, again showing a difference in freezing between Th-Cre$^{LC\text{-}DG}$::ArchT mice and wild-type controls (**Fig. S1C-D**). On the other hand, in the one-trial contextual fear conditioning paradigm, the LC-DG inhibition affected neither acquisition nor retrieval of the contextual information itself (**Fig. S1H-I**). These results indicate that inhibition of the LC-DG projections reduces contextual fear generalization and facilitates disambiguation.

The LC-NE system is highly responsive to stress (McCall et al., 2015; Valentino and Van Bockstaele, 2008). The facilitation effect of contextual fear generalization modulated by the LC-DG circuit is evolutionarily beneficial to survival in stressful contexts. For example, it would be more advantageous to generalize a potentially dangerous context or cue to increase one's chance of survival (Kaouane et al., 2012). We tested if stress exposure mimics the impairment of CFD as we have seen in the manipulation of the LC-DG system (**Fig. 4S-T**). Indeed, when animals were treated with restraint stress before the CFD task, they showed impairment in the CFD task consistent with our LC-DG activation experiment, indicated by results that the naïve group of animals showed the significant interaction of Training x Context in freezing, but not Stressed group (**Fig. S1J-L**). It is important to indicate that there were overall reductions in freezing level in the stressed group, which was not observed in the LC-DG specific manipulation (**Fig. 2.2I**). The freezing reduction in the stressed group indicates that the stress manipulation may also recruit other modulators that influence the performance of fear processing (e.g. glucocorticoid, which impair fear memory processing). These results are consistent with our overarching hypothesis that stressful events activate the LC-NE system, and that

stress facilitates contextual fear generalization. In addition, these results further support the more recently proposed functional heterogeneity hypothesis of LC function, and that specific projections to the DG facilitate contextual fear generalization. These results also further support the more recently proposed functional heterogeneity hypotheses of the LC circuit network (Seo and Bruchas, 2017; Uematsu et al., 2017).

2.4 Discussion

Here, we report that the LC-DG noradrenergic circuit modulates CFD. We found that photo-activation of the LC-DG projection in Th-Cre$^{LC\text{-}DG}$::ChR2 mice led to an impairment in performance as CFD training progressed with similar contexts, but not with more pronounced differences between two contexts. Although this remains consistent with the notion that the DG is involved in distinguishing new information that is similar to existing information, our results are somewhat contradictory to the general role of the LC-NE system enhancing memory formation as shown in recent studies demonstrated that optogenetic activation of LC-CA1 and CA3 circuits enhances memory formation (Kempadoo et al., 2016; Takeuchi et al., 2016; Wagatsuma et al., 2018).

Classically, the DG-GC is thought to assist hippocampal processing of a new experience, rather than retrieval, recruiting different subgroups of GCs when the new experience is similar to a past experience. In a one-trial contextual fear conditioning task we performed, LC-DG manipulation affected neither acquisition nor retrieval of the contextual information itself (**Fig. S1H-I**). The results we present here indicate that rather than being associated with rapid processing of new episodic memories, the LC-DG circuit is likely to be more involved in differentiating between a prior and new event as they are repeatedly presented. On the other hand, other studies have supported the notion that

the adrenergic nervous system mediates emotion-related memory consolidation and reconsolidation (Gazarini et al., 2013; Otis et al., 2015). Recent studies have also reported that LC-NE axons projecting to the hippocampus release dopamine, resulting in enhanced memory consolidation (Kempadoo et al., 2016; Takeuchi et al., 2016; Wagatsuma et al., 2018). In our current study, we sought to control the LC-DG circuits only during the training period, when the contexts were posed to animals. Therefore, it is not clear if the LC-DG system also contributes to the consolidation phase of the learning process, and future studies focused on different phases in memory dynamics (e.g., consolidation, reconsolidation, or after completing long-term CFD) will help to clarify the LC-DG circuit mechanism on the memory process.

With regards to LC-NE inhibition, developing an ideal inhibitory optogenetic tool has been challenging. The light sensitive chloride pump Halorhodopsin (NpHR) was one of the popular tools used in rapidly silencing the activity of neurons. However, it has been reported that NpHR can cause problematic changes in synaptically evoked spiking activity in the period following light activation (Raimondo et al., 2012). Another popular optogenetic silencing tool is archaerhodopsin-3 (Arch), a light-driven outward proton pump, which we chose to use to inhibit the LC-DG circuit in the current study. A recent study reported that sustained Arch photo-activation gradually increased spontaneous neurotransmitter release in the neuronal terminals (Mahn et al., 2016). However, LC-DG terminal inhibition in this report had opposing effects to the activation experiment using ChR2, likely because the rebound effect is low for stimulus durations under a few minutes in length, or differently affected by experimental settings such as light intensity.

Recent discoveries indicate that neuromodulatory input from LC to hippocampus contributes to processing information pertaining to environmental novelty and spatial tuning (Kempadoo et al., 2016; Takeuchi et al., 2016; Wagatsuma et al., 2018). With the more recent discovery of functional heterogeneity in LC neural circuits, we speculate that LC cells projecting to the DG modulate the DG-dependent pattern separation process, contributing to contextual fear generalization, while LC input to the CA3/CA1 may be involved in the rapid processing of novel contextual information (Wagatsuma et al., 2018). Functional heterogeneity along the septotemporal axis in the hippocampus has also been proposed, and although the basic micro circuitry within the hippocampus is remarkably similar between dorsal and ventral regions, their intersectional connection to the extra-hippocampal structures and their implicated functions on behavior are known to be quite different along the dorso-ventral axis (i.e. spatial Vs. emotional information). Furthermore, the functional heterogeneity in the DG is also associated with adult hippocampal neurogenesis, a process by which new GCs in the DG are generated and integrated into hippocampal circuitry. An important aspect of hippocampal adult neurogenesis is the distinct physiological characteristics of newborn neurons depending on their age. A recent study monitoring adult newborn neuron using *in vivo* two-photon calcium imaging within a contextual discrimination task found that young adult born neurons (<6 weeks) display higher rates of neuronal firing than matured neuron, and lower tuning specificity with contextual changes, while mature neurons show more spatial tuning characteristics than young neurons, suggesting that young neurons are more involved in novelty detection rather than spatial tuning (Danielson et al., 2016). They also demonstrated that optogenetic inhibition of the young neurons during exposure to the

safe context but not the unsafe context resulted in impairment of contextual fear discrimination, suggesting that young neurons in the dorsal DG are involved in processing the novel safe context. Taken together, it will be important to investigate how LC-NE system functionally modulates the different developmental stages of adult born neurons along dorso-ventral axis.

Chapter 3. *In Vivo* Calcium Imaging During Contextual Fear Discrimination Reveals Changes in DG Ensemble Dynamics

3.1 Introduction

Classically, the DG-GC is thought to assist hippocampal processing of a new experience, recruiting different subgroups of GCs when the new experience is similar to a past experience. Moreover, our work indicates that rather than being associated with rapid processing of new episodic memories, the LC-DG circuit is likely to be more involved in differentiating between a prior and new event as they are repeatedly presented. We also report that bidirectional manipulation of the LC-DG circuit results in opposing learning states, with activation of LC-NE terminals in the DG resulting in contextual generalization and inhibition of these projections leading to facilitation of contextual disambiguation (Seo et al., 2021). In this chapter, we aim to elucidate the mechanisms by which the LC-NE system modulates DG neural ensemble activity during aversive contextual processing.

The DG granule cell layer (GCL) has been well documented by existing research as a site of adult neurogenesis, suggesting a key role in learning and memory (Borzello et al., 2023; Cameron et al., 1993; Kuhn et al., 2018). These adult-born granule cells (GCs), which are continuously generated throughout adulthood, display heightened excitability and synaptic plasticity, and respond more strongly towards external stimuli compared to their mature counterparts, and this appears to be linked with discrimination of similar memories (Denny et al., 2012; Marín-Burgin et al., 2012; Schmidt-Hieber et al., 2004; Zhuo et al., 2016). There is also evidence that the DG makes use of adult neurogenesis to tune immature adult-born GCs to specific experiences (Miller and Sahay, 2019; Teyler and DiScenna, 1986). Additionally, GC activity in the DG is extremely

sparse, with fewer than 5% of GCs active in any given environment during exploration behavior (Chawla et al., 2005; Hainmueller and Bartos, 2018). Typically, DG GCs will fire in response to a specific location, also known as a place field, and many place fields undergo a process called remapping, when exposed to similar environments (Danielson et al., 2016). However, when animals are transferred into a different chamber in a different room, a different subset of GCs becomes active, suggesting that there is a graded amount of remapping that occurs based on environmental contexts (GoodSmith et al., 2017). Furthermore, GCs have been shown to develop new place fields when exposed to novel surroundings, through what is theorized to be strengthening of PP input synapses (Diamantaki et al., 2016; Kim et al., 2018; Sheffield et al., 2017).

Several theories exist regarding how DG pattern separation occurs. One postulates that because GCs receive only a small number of synaptic inputs, and fire very sparsely in response to these inputs, overlapping responses are represented as orthogonal representations in the GCL, increasing the ability of the GCs to learn and store information in a variety of different contexts. Through distinguishing these output representations from their input representations via recruitment of distinct populations of GCs, it becomes possible to recall and disambiguate highly similar experiences from one another (Yassa and Stark, 2011). Another model suggests that through the strengthening and weakening of specific synapses, distinct subsets of GCs may be reactivated for previous experiences or recruited to distinguish between similar experiences (Ewell and Jones, 2010; Scharfman et al., 1990). It is also possible that different learned experiences re-engage distinct populations of neurons in the DG, which results in recall of previous similar experiences. Additionally, recent evidence shows that this may be facilitated by

gradual activity changes in these DG granule cells, rather than by completely distinct sets of neurons (Hainmueller and Bartos, 2018; Senzai and Buzsáki, 2017). Lastly, the DG is often implicated in novelty detection theory, and responses in the DG are modulated by influences such as norepinephrine, showing increased activity during new experiences (Amaral and Campbell, 1986; Harley, 2007; Prince et al., 2016). However, it remains unknown how LC-NE modulation of the DG impacts DG neural ensemble activity.

In this chapter, we conduct an integrated neuromodulatory circuit analysis approach, combining chemogenetic tools and *in vivo* Ca^{2+} imaging with a well-established Pavlovian contextual fear discrimination (CFD) paradigm in which animals were placed in two similar, but different, contexts daily (Danielson et al. 2016; Lovett-Barron et al., 2014; McHugh et al., 2007). Through the use of these techniques, we elucidate the role of DG neural ensemble dynamics in contextual fear discrimination, and the impact of the LC-NE system on modulating changes in neural ensemble recruitment during aversive contextual processing.

3.2 Methods

3.2.1 Animals

Adult (25-35 g) male *TH*-IRES-Cre mice, *Dbh*-Cre mice, and Cre (-) littermate control mice were used for *in vivo* experiments after backcrossing to C57BL/6J mice for at least 10 generations. Mice were group housed, given access to food pellets and water *ad libitum*, and maintained on a 12:12-hour light/dark cycle (lights on at 7:00 a.m.). Animals were held in a sound attenuated holding room facility in the lab starting at least one week prior to surgery, as well as post-surgery and throughout the duration of behavioral assays to minimize stress from transportation and disruption from foot traffic.

All mice were handled and, where appropriate, connected to a miniscope two times a day for one week prior to behavioral experimental testing. All experimental procedures were approved by the Animal Care and Use Committee of Washington University and the Animal Care and Use Committee of University of Washington and conformed to NIH guidelines.

3.2.2 Stereotaxic surgery

All surgeries were performed under 4% isoflurane anesthesia (Piramal Healthcare, Maharashtra, India). For in vivo Ca^{2+} imaging experiments, we first tested several dilutions of AAV5-CaMKIIα-GCAMP6f (1.31x1013 VG/ml, 1:1,1:3,1:10) to ensure optimal expression within the DG to ensure accurate sparse labeling for ideal imaging conditions (1:3). We then injected unilaterally with 400 nl of AAV5-CaMKIIα-GCAMP6f into the DG area (AP: -2.15, ML: +1.4, DV: -2.1) using a Hamilton syringe with blunted needle, and 800 nl of AAV5-Syn-DIO-HM3D(Gq)-mCherry into the LC using a Hamilton syringe with beveled needle. After waiting at least two weeks to allow for viral spread, we implanted a microendoscopic GRIN lens (1mm diameter x 4mm in length) 100 microns above the previously injected dorsal DG (AP: -2.15, ML: +1.4, DV: -2.0) using the previously described protocol (Resendez et al., 2016). Briefly, using a trephine drill bit, a circular portion of the skull was removed from above the viral injection site and exposed tissue was washed with saline. The GRIN lens was then slowly lowered (100μm/min) into place with a stable stereotaxic holder attachment. Superglue was used to fix the lens in place and prevent movement during imaging, and a dental cement wall was built on the skull surrounding the lens with 2-3 anchor screws inserted into surrounding areas of the skull for support. The lens was then covered with silicone elastomer sealant (Kwik-Cast) for 1-

2 weeks before checking for visibly fluorescent cells. Once the best focus was obtained, a baseplate (Inscopix) was mounted with superglue on top of the skullcap, surrounding the lens at the optimal focal distance for imaging.

3.2.3 Contextual fear discrimination behavioral task

We used a well-established Pavlovian contextual fear discrimination (CFD) paradigm in which animals were placed in two similar, but different, contexts daily (Danielson et al. 2016; Lovett-Barron et al., 2014; McHugh et al., 2007). Fear conditioning took place in Med-Associates conditioning chambers that consisted of one clear plexiglass wall, three aluminum walls, and a stainless-steel grid as a floor. The training chamber was housed in a sound attenuated cubicle. Context A was rectangular, with floors made of stainless-steel rods (2 mm diameter, spaced 5 mm apart), walls of aluminum and acrylic, and cinnamon extract scent, and was cleaned with 70% ethanol between runs. Context B differed from context A in that it had a white acrylic floor and a wall decorated with a black and white striped pattern. Context B was cleaned with multi-purpose surface cleaner (Method, UPC: 817939000106) between runs, and scented with peppermint extract. All sessions were recorded from the side using a digital camera and were scored for freezing by an investigator blind to the genotype of the animal.

Mice were handled for 5 minutes per day for a week prior to training. Contextual fear discrimination training took place in the apparatus described above. In context A (unsafe context), animals were placed in the conditioning chamber and allowed to freely explore for 180 seconds, after which they received a single 2 second foot shock of 0.50 mA. Mice were taken out 15 seconds after termination of the foot shock and returned to their home cage. In context B (safe context), mice were allowed to freely explore the

context for 197 seconds, the same amount of total time that they were in context A, and then returned to their home cage. In this context, no foot shock was delivered. All freezing in both contexts was assessed for the first 180 seconds, and the last 17 seconds were not included in the behavioral analysis. Freezing was done in a double-blind fashion to avoid bias in manual scoring.

On the first day (Day 0) of CFD training, all animals were placed in context A and received a foot shock. The next day (Day 1), mice were run first in context B with no foot shock, then in context A with a foot shock. There was a minimum 3-hour period between exposure to context A and context B. This training protocol was repeated daily for 9 days.

3.2.4 *In vivo* calcium imaging in freely moving mice

After allowing at least 1 week of recovery following baseplate surgery, a dummy scope weighing 2g was attached to the baseplate to acclimate the mice to the weight of the microscope and habituated to the attachment of the microscope. In order to attach the microscope securely to the baseplate, mice were scruffed and the nVista miniscope was connected to the magnetic baseplate and secured with a set screw. During habituation, optimal focus, field of view, and LED power and gain settings were determined visually and optimized for each individual mouse by assessing the presence of clearly defined putative neurons. These settings were then kept constant for each test day. Following optimization of imaging settings, the mice then underwent the contextual fear discrimination task.

3.2.5 Calcium imaging data processing and analysis

nVista acquisition software (Inscopix) was used to acquire images of fluorescence dynamics at 20 frames per second. Fear conditioning control software Video Freeze (Med

Associates) was programmed to trigger the beginning of the imaging session with recording of fear behavior simultaneously.

Mosaic (Inscopix) was used to preprocess Ca^{2+} data from each imaging session as previously described (Jennings et al., 2015; Resendez et al., 2016; Rubin et al., 2015; Ziv et al., 2013). Briefly, for each day, calcium imaging data from context A and context B were down-sampled temporally (2x temporal bin) and spatially (2x spatial bin), concatenated together, and rigid motion correction was applied. After preprocessing, putative single neuron activity was segmented using Constrained Non-negative Matrix Factorization for Endoscopic data (CNMFe) according to established criteria using custom MATLAB (MathWorks, Natick, MA, USA) scripts and sorted manually by a blind observer according to established criteria (Resendez et al., 2016; Zhou et al., 2018). Background components were estimated using the "ring" model, which was chosen after thorough parametrization to limit the presence of non-neuronal signals in our dataset.

Following sorting, individual putative single neurons were tracked between Days 1 and 9 during the CFD task using CellReg (Sheintuch et al., 2017). For each mouse the spatial correlation registration threshold performed best, and optimal correlation thresholds were determined by the algorithm. Final registration utilized the probabilistic model for all mice. To assess the link between cell selectivity and behavior in the CFD task, a Pearson correlation was conducted for Days 1 and 9 for Th-$Cre^{LC\text{-}DG}$::HM3Dq mice as well as wild-type controls (**Fig. 3.1M, Fig. 3.2I**). This Pearson correlation utilized the ratio of cells selective to context A vs. context B compared to the ratio of freezing in context B vs. context A.

To assess changes in ensemble activity over the course of training, we examined neurons classified on day 9 as either responding selectively to context A, context B, or nonselectively as a subset of selectivity on day 1 (**Fig. 3.1P, Fig. 3.2K**). This produced nine subsets: percentage of neurons responsive to A on both days, responsive to A on day 1 and B on day 9, responsive to A on day 1 and nonselective on day 9, etc.

Raw fluorescence traces for individual putative neurons were Z-normalized ($Z = \frac{x-\mu}{\sigma}$) to their session average activity for Day 1 and Day 9 using custom MATLAB code. In order to classify cells as selective for context A, context B, or non-selective, a two-tailed *t*-test comparing event traces during the first 180 seconds (1800 samples) in context A to the subsequent 180 seconds (1800 samples) in context B for each day (**Fig. S3H**). A critical $\alpha \leq 0.05$ was chosen to determine whether a cell was significantly more active in a specific context on a given day. Differences in context specific cell selectivity across training were determined using a chi-squared test.

3.2.6 Pharmacological manipulation of LC-DG circuit

For drug injection experiments, mice injected with DREADD virus were allowed to recover for 4 weeks after surgery before habituation. During habituation, mice received an i.e. injection of saline to habituate them to the injection process, after which they were placed back in the home cage. On each test day, mice received i.p. injections of clozapine-N-oxide (CNO; 5 mg/kg) 30 minutes prior to CFD training, after which they were placed back in their home cage. After 30 minutes, they were placed into the behavioral chamber to undergo CFD training. For transgenic controls, mice were injected with saline instead of CNO i.p. 30 minutes prior to CFD training.

3.2.7 Statistical analysis

All data are expressed as mean ± SEM. Behavioral data were analyzed with JMP12 Pro (SAS institute, Cary, NC, RRID:SCR_014242) and GraphPad Prism. *Student's t*-test, one-way or two-way ANOVAs were used to analyze between-subjects designs. Chi-squared tests (Jimenez et al., 2018; Jimenez et al., 2020) and Kolmogorov–Smirnov tests were used to analyze probability distributions. Repeated-measures designs were analyzed using mixed-effects restricted maximum likelihood (REML) model. Tukey was used for *post-hoc* pairwise comparisons. The null hypothesis was rejected at the $p < 0.05$ level. Statistical significance was taken as $*p < 0.05$, $**p < 0.01$, $***p < 0.005$, *n.s.* represents not significant. All statistical information is listed in Table S1.

3.3 Results

We next examined whether a DG neuronal ensemble encodes the dynamic behavioral states during CFD training, utilizing *in vivo* calcium imaging by injecting an AAV expressing the genetically encoded calcium indicator, GCaMP6f, driven by CamKII promoter, into the DG, followed by the implantation of a micro-endoscopic GRIN lens to monitor neuronal ensemble changes (**Fig. 3.1A-B, Fig. S3A-B**). In addition, while neuronal activity of GCs in the DG was monitored, LC-NE activity was increased by the expression of Cre-dependent excitatory designer receptor exclusively activated by designer drugs (DREADD) infection in LC-NE (Th^+) neurons. The DREADD agonist clozapine-N-oxide (CNO) was then injected prior to imaging (**Fig. 3.2A-C**). Control, wild type mice were treated in the same way with DREADD and CNO during the CFD paradigm (**Fig. 3.1A-C**).

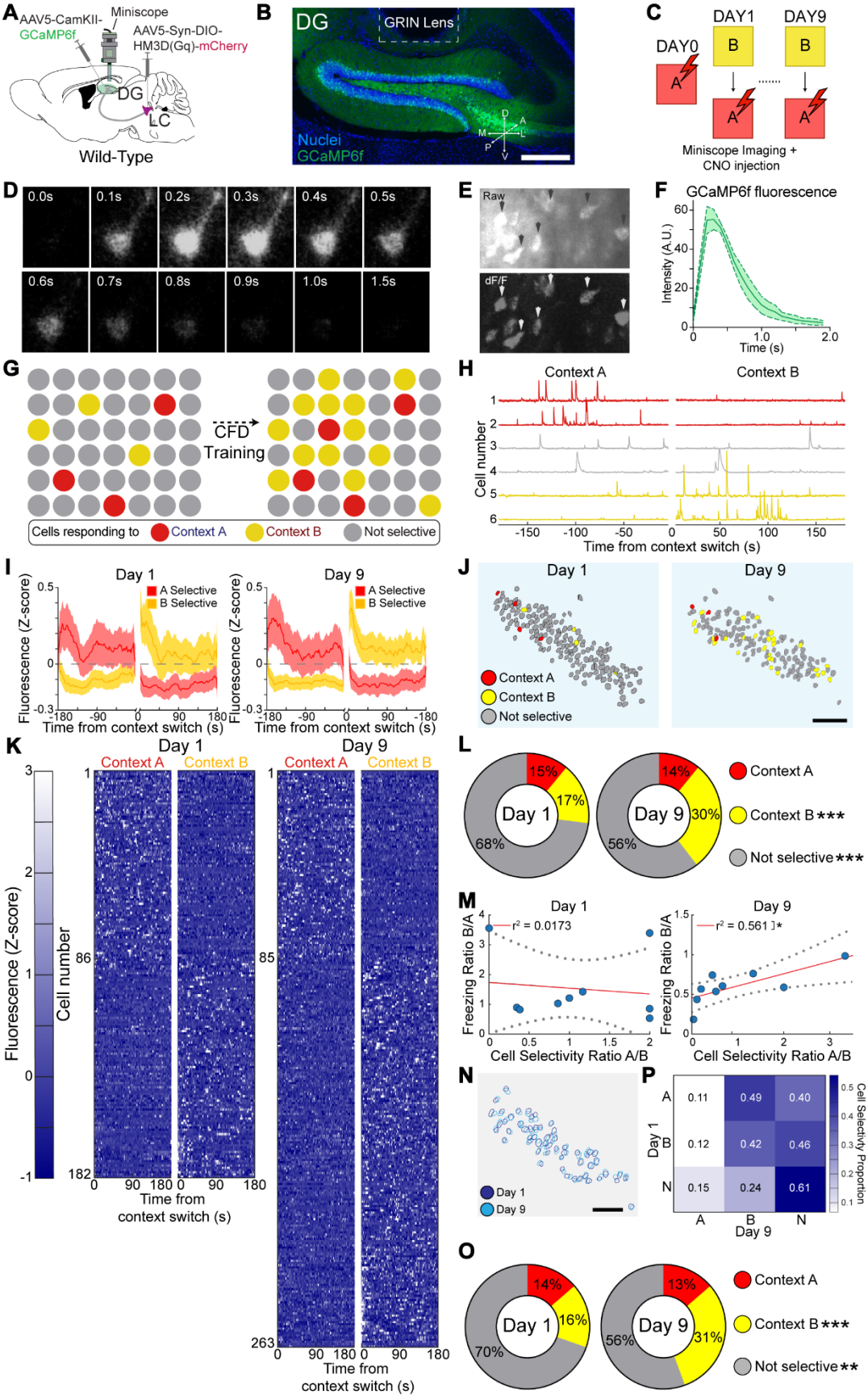
A
AAV5-CamKII-GCaMP6f
Miniscope
AAV5-Syn-DIO-HM3D(Gq)-mCherry
DG
LC
Wild-Type
B
DG
GRIN Lens
Nuclei
GCaMP6f
C
DAY0
DAY1
DAY9
Miniscope Imaging + CNO injection
D
0.0s
0.1s
0.2s
0.3s
0.4s
0.5s
0.6s
0.7s
0.8s
0.9s
1.0s
1.5s
E
Raw
dF/F
F
GCaMP6f fluorescence
Intensity (A.U.)
Time (s)
G
CFD Training
Cells responding to
Context A
Context B
Not selective
H
Context A
Context B
Cell number
Time from context switch (s)
I
Day 1
Day 9
A Selective
B Selective
Fluorescence (Z-score)
Time from context switch (s)
J
Day 1
Day 9
Context A
Context B
Not selective
K
Day 1
Day 9
Context A
Context B
Fluorescence (Z-score)
Cell number
Time from context switch (s)
L
Day 1
Day 9
15%
17%
68%
14%
30%
56%
Context A
Context B***
Not selective***
M
Day 1
Day 9
r² = 0.0173
r² = 0.561)*
Freezing Ratio B/A
Cell Selectivity Ratio A/B
N
Day 1
Day 9
P
A
B
N
0.11
0.49
0.40
0.12
0.42
0.46
0.15
0.24
0.61
Day 1
Day 9
Cell Selectivity Proportion
O
Day 1
Day 9
14%
16%
70%
13%
31%
56%
Context A
Context B***
Not selective**

Figure 3.1. Imaging of DG neural ensemble activity during contextual fear discrimination.
(**A**) Schematic of experimental approach depicts Ca^{2+} indicator (GCaMP6f) injected into the DG, and a microendoscopic GRIN lens implanted above the DG (**B**) Representative image depicting expression of GCaMP6f in the DG driven by CaMKII promoter and location of GRIN lens implant. Scale bar = 100 µm. (**C**) CFD with CNO injection 30 minutes prior to task and imaging during task. (**D**) Time-lapse image sequence of GCaMP6f fluorescence in an individual neuron. (**E**) Example of raw and dF/F *in vivo* epifluorescence images. (**F**) Intensity measurement of fluorescence dynamics from $GCaMP6f^{+}$ neurons (n = 6). (**G**) Schematic depicts hypothetical ensemble changes in the DG during CFD training. (**H**) Representative neurons responding selectively to context A (unsafe, top), context B (safe, bottom), or responding nonselectively (middle). (**I**) Averaged cell activity traces during days 1 and 9 of CFD task for neurons responding selectively to context A or context B. (**J**) Representative map of changes in context selectivity from day 1 (left) to 9 (right) of training in wild-type mice. (**K**) Fluorescence maps of cells identified from wild-type mice as responding selectively to context A (unsafe) and context B (safe) during days 1 (left) and 9 (right) of training (n = 9). There was a minimum 3-hour gap between exposure to context B and context A. Cells were classified using a two-tailed *t*-test comparing Z-normalized fluorescence during the first 180 seconds in each context during Days 1 and 9. (**L**) Distribution of cells responding selectively to A, selectively to B, or nonselectively between days 1 and 9 of training. (**M**) Linear regression using Pearson correlation for ratio of cell selectivity between context A and context B vs. ratio of freezing behavior between context A and context B (Pearson correlation for cell selectivity ratio vs. freezing ratio: Day 1: $r = -0.132$, $r^2 = 0.0173$, $p = 0.737$; Day 9: $r = 0.749$, $r^2 = 0.561$, $p = 0.0202$). (**N**) Schematic depicting matching of reliably tracked neurons recorded both at the beginning and end of training. (**O**) Representation of shifts in cell selectivity between Day 1 and Day 9 of CFD training in reliably tracked neurons. (**P**) Distribution of cells identified at both the beginning and end of training responding selectively to A, selectively to B, or nonselectively between days 1 and 9 of training. All data are mean ± SEM. $*p < 0.05$, $**p < 0.01$, $***p < 0.005$.

When wild-type controls (HM3Dq(-); **Fig. 3.1**) underwent contextual fear conditioning, we successfully recorded and segmented responses of individual neurons in the GCL (**Fig. 3.1D-F**). For each day of training, individual neurons were classified as preferentially active in context A, context B, or not selective for context (**Fig. 3.1H**). This was achieved by conducting a two-sample *t*-test of Z-scored fluorescence traces from context A and context B with an alpha level of $p < 0.05$. To validate this methodology, we compared average activity while in both contexts and response amplitude in both contexts of cells that were classified as either selective to context A or context B. In both cases, neurons showed significant differences in activity preferential towards the context they were classified in (**Fig. 3.1I, Fig. S3F-H**). Cells selective to context A (unsafe) demonstrated markedly higher activity and response amplitude in context A compared to context B (safe), and cells selective to context B displayed the opposite trend in activity,

further substantiating this classification approach. There were no significant context specific shifts in response amplitude among classified cells during the training.

In wild-type controls, we observed an increase in cells selectively responding to context B (safe) over the course of CFD training (**Fig. 3.1K**). This suggests that as mice learn to distinguish between context A (unsafe) and context B (safe), their behavioral output is matched by a subsequent shift in DG-GC ensemble dynamics towards context B (**Fig. 3.1G**). Mice that were able to avoid generalization and encode ambiguous cues separately from threatening cues experienced an increased recruitment in cells responding to context B (safe) (**Fig. 3.1J**). On the first day of training, wild-type controls at first generalized between context A (unsafe) and context B (safe) together and had a similar proportion of neurons responding in each context. However, as they learned to disambiguate cues relating to context B (safe) from threatening cues related to context A (unsafe), a significantly increased population of neurons was recruited to respond in that context (**Fig. 3.1L**). These results suggest that as wild-type mice successfully improve their performance in the CFD task, GC ensemble dynamics in the DG shift to reflect this change in behavior, with an increased recruitment of neurons responding to context B (safe) as the recognition of that context increases.

To quantify this potential correlation, we calculated a ratio between the proportion of cells responding selectively to either context A (unsafe) or B (safe) for each mouse at both the beginning and end of training, as well as the proportion of freezing behavior in context B (safe) compared to context A (unsafe). We used linear regression and Pearson correlation to assess the link between these ratios for both the beginning and end of training (**Fig. 3.1M**). While there is little to no relationship between the two variables at

the beginning of training, by the end of the task this shifts to a significant fit between cell selectivity ratio and freezing ratio in the two contexts. These data further indicate that as mice are better able to disambiguate the two distinct contexts, a corresponding shift in DG-GC ensemble activity occurs proportional in strength to their discrimination ability in the task. It also indicates that the effect seen in the DG ensemble is not driven by a single mouse, but rather that the cohort as a whole show consistent increases in context B cells across training.

We also determined whether the DG ensemble shifted when looking only at cells that were identified both at the beginning and the end of training (**Fig. 3.1N**). Here we report a nearly identical effect occurs compared to the general population of imaged cells, whereby there is an increased population of neurons responding in context B (safe) over the course of the training (**Fig. 3.1O**). In addition, we also examined shifts in individual cell selectivity over the course of the training, to determine whether high percentages of neurons tended to shift from a particular selectivity at the beginning of training to a different selectivity at the end of training (**Fig. 3.1P**). This was done by dividing neurons into nine different categories based on their selectivity on day 1 and day 9 of training. A high percentage (~42%) of neurons responding selectively to context B (safe) at the beginning of training remained selective to that context at the end of training, and a high percentage (~49%) of neurons responded selectively to context A (safe) at the beginning of training and then selectively to context B (safe) by the end of training. These data further corroborate our findings of a shift in DG GC ensemble in wild-type mice during the course of the training.

These results suggest that neurons that responded selectively to context B (safe) at the beginning of training tended to remain selective to that context. However, neurons that responded selectively to context A (unsafe), and neurons that responded nonselectively, at the beginning of training were recruited to respond in context B (safe) as mice disambiguate the cues related to that context.

The use of calcium imaging techniques allowed us to determine that wild-type mice that were able to successfully discriminate between the two similar contexts experience a specific pattern shift of GC ensemble dynamics in the DG. We next sought to understand how increased LC-NE activity, which is sufficient to produce fear generalization (**Fig. 2.2C**), impacts the context specific changes in GC ensemble activity. We utilized *in vivo* calcium imaging in the DG while controlling activity from the LC chemogenetically in Th-Cre mice (**Fig. 3.2A-B, Fig. S3A-B**). These mice then underwent the CFD task following intraperitoneal injections of the DREADD agonist CNO (**Fig. 3.2C**) which allowed us to capture precise neural ensemble dynamics in Th-Cre^{LC-DG}::HM3Dq mice while eliciting increased tonic LC activity Similar to what we observed with optogenetic activation of the LC-DG projection (**Fig. S1A**), we observed that wild-type controls were able to successfully disambiguate the two similar contexts, while Th-Cre^{LC-DG}::HM3Dq mice were unable to do so effectively (**Fig. 3.2D**). These data indicate that the microendoscope implantation and miniature microscope weight did not interfere with the expression of behavior in the CFD task and that tonic LC activation via DREADDs produces context generalization. Additionally, Th-Cre^{LC-DG}::HM3Dq mice treated with saline had lower freezing in context B (safe) compared to context A (unsafe) than Th-Cre^{LC-DG}::HM3Dq mice treated with CNO by the end of training. These results establish

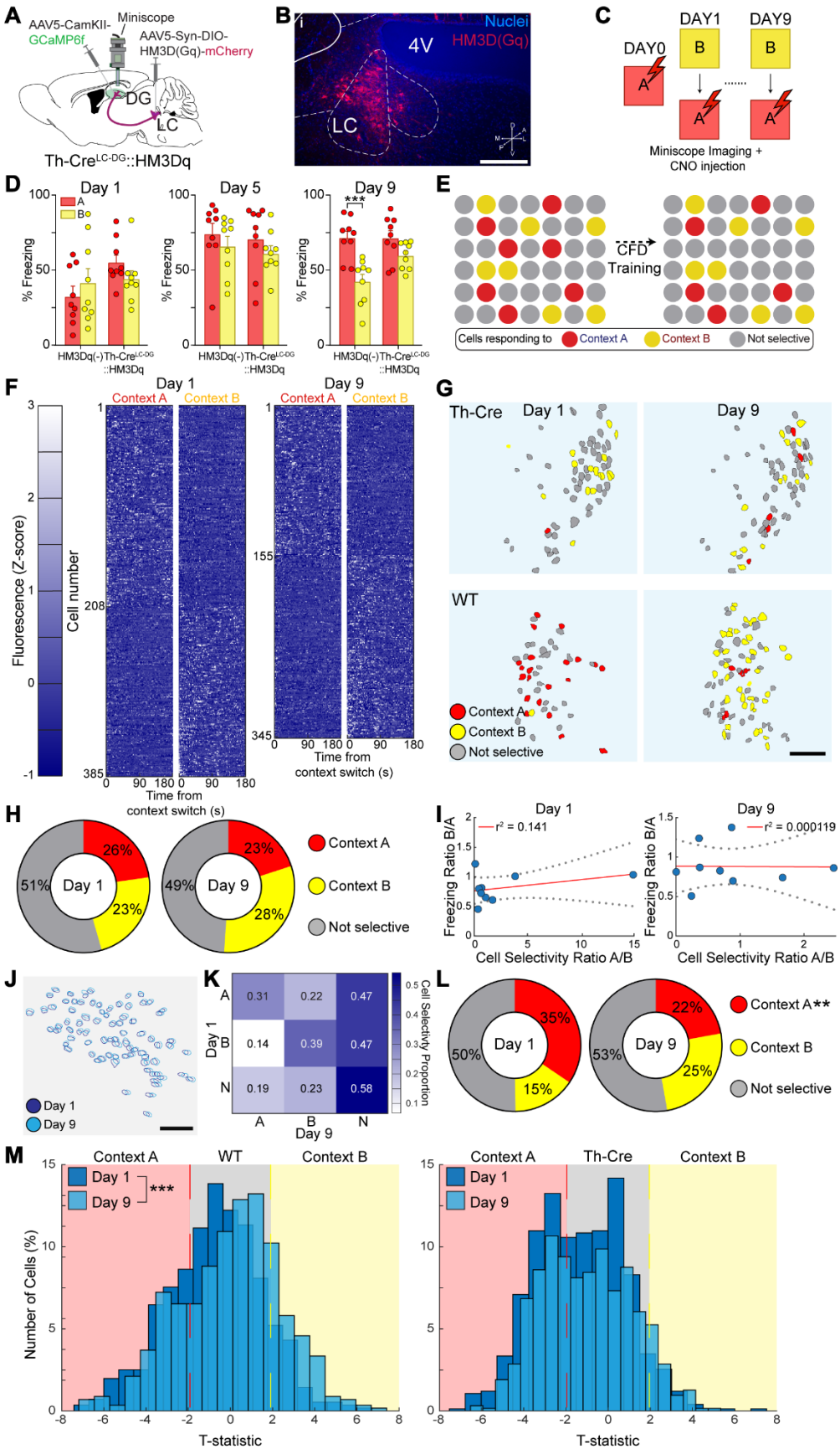
A
AAV5-CamKII-GCaMP6f
Miniscope
AAV5-Syn-DIO-HM3D(Gq)-mCherry
DG
LC
Th-Cre LC-DG ::HM3Dq
B
i
Nuclei
4V
HM3D(Gq)
LC
C
DAY0
DAY1
DAY9
A
B
Miniscope Imaging + CNO injection
D
Day 1
Day 5
Day 9
% Freezing
HM3Dq(-)Th-Cre LC-DG ::HM3Dq
E
CFD Training
Cells responding to
Context A
Context B
Not selective
F
Day 1
Day 9
Context A
Context B
Fluorescence (Z-score)
Cell number
Time from context switch (s)
G
Th-Cre
WT
Day 1
Day 9
Context A
Context B
Not selective
H
Day 1
Day 9
26%
23%
51%
23%
28%
49%
Context A
Context B
Not selective
I
Day 1
Day 9
r² = 0.141
r² = 0.000119
Freezing Ratio B/A
Cell Selectivity Ratio A/B
J
Day 1
Day 9
K
0.31
0.22
0.47
0.14
0.39
0.47
0.19
0.23
0.58
Day 1
Day 9
Cell Selectivity Proportion
L
Day 1
Day 9
35%
15%
50%
22%
25%
53%
Context A**
Context B
Not selective
M
Context A
WT
Context B
Th-Cre
Day 1
Day 9
***
Number of Cells (%)
T-statistic

Figure 3.2. Chemogenetic activation of LC-NE neurons alters DG neural ensemble activity during contextual fear discrimination.
(**A**) Schematic of experimental approach depicts infection of LC-NE cells using Th-Cre mouse line with DREADD system activating HM3Dq signaling chemogenetically (Th-Cre$^{LC\text{-}DG}$::HM3Dq), as well as Ca^{2+} indicator (GCaMP6f) injected into the DG, and microendoscopic GRIN lens implanted above the DG. (**B**) Representative image depicting expression of HM3Dq in LC-NE cells of Th-Cre mice. Scale bar = 50 μm (**C**) CFD task with CNO injection 30 minutes prior to task and imaging during task. (**D**) Chemogenetic activation of the LC-NE system impairs behavioral pattern separation in mice expressing HM3Dq in LC-DG projections (Th-Cre$^{LC\text{-}DG}$::HM3Dq, n = 9), but not in wild-type controls (HM3Dq(-), n = 9). HM3Dq(-) controls were able to discriminate on the ninth day of training, while Th-Cre$^{LC\text{-}DG}$::HM3Dq mice were unable to discriminate during the training. (**E**) Schematic depicts hypothetical ensemble changes in the DG during CFD training following activation of LC-NE system. (**F**) Fluorescence maps of neurons identified from Th-Cre mice as responding selectively to context A (unsafe) and context B (safe) during days 1 (left) and 9 (right) of training (n = 9). There was a minimum 3-hour gap between exposure to context B and context A. Cells were classified using a two-tailed *t*-test comparing Z-normalized fluorescence during the first 180 seconds in each context during Days 1 and 9. (**G**) Representative map of changes in context selectivity from day 1 (left) to 9 (right) of training in Th-Cre mice following activation of LC-NE system (top) and in wild-type mice (bottom). (**H**) Distribution of cells responding selectively to context A, selectively to context B, or nonselectively during days 1 and 9 of training. (**I**) Linear regression using Pearson correlation for ratio of cell selectivity between context A and context B vs. ratio of freezing behavior between context A and context B (Pearson correlation for cell selectivity ratio vs. freezing ratio: Day 1: r = 0.375, r^2 = 0.141, p = 0.32; Day 9: r = -0.109, r^2 = 0.0001, p = 0.98). (**J**) Schematic depicting matching of reliably tracked neurons recorded both at the beginning and end of training. (**K**) Representation of shifts in cell selectivity between Day 1 and Day 9 of CFD training in reliably tracked neurons. (**L**) Distribution of cells identified at both the beginning and end of training responding selectively to A, selectively to B, or nonselectively between days 1 and 9 of training (**M**) Normalized distribution of all identified neurons in wild-type controls (left) and Th-Cre$^{LC\text{-}DG}$::HM3Dq mice (right) during days 1 and 9 of training. All data are mean ± SEM. **p* < 0.05, ***p* < 0.01, ****p* < 0.005.

that differences in freezing levels between the two groups were not due to the transgenic background of the mice (**Fig. S3C-E**).

Since Th-Cre$^{LC\text{-}DG}$::HM3Dq mice were not able to differentiate between the two different contexts, we hypothesized that DG-GC ensemble dynamics would not shift during chemogenetic LC activation towards context B (safe), as they did in wild-type controls (**Fig. 3.2E**). Again, we classified cells imaged during a CFD study as selective to context A, selective to context B, or not selective to either context at the beginning and end of training, based on their relative activity levels in each context (**Fig. S3F-H**). In this experimental paradigm, we found that wild-type, CNO-injected controls showed increased recruitment of cells responding in context B (safe), however Th-Cre$^{LC\text{-}DG}$::HM3Dq, CNO-injected mice did not display a similar level of elevated neuronal

recruitment in the GCL. Th-Cre$^{LC\text{-}DG}$::HM3Dq mice had equal amounts of neuronal activity in context A and context B on both the first and last days of training (**Fig. 3.2F**). Th-Cre$^{LC\text{-}DG}$::HM3Dq mice were not able differentiate between the two contexts, while the neuronal ensemble activity underwent no significant changes in recruitment for either context (**Fig. 3.2G-H**). These results indicate that unlike wild-type controls, elevated tonic LC activity in Th-Cre$^{LC\text{-}DG}$::HM3Dq mice produces more homogenous DG ensemble activity, and while cell selectivity was maintained on an individual neuron basis, the ensemble as a whole was not able to clearly disambiguate contextual cues, preventing recruitment of new granule cells in the DG. We next examined the relationship between the behavioral and neural ensemble changes occurring in Th-Cre$^{LC\text{-}DG}$::HM3Dq mice. There was no correlation between A:B cell selectivity ratio and B:A behavioral response ratio in Th-Cre$^{LC\text{-}DG}$::HM3Dq mice on both days 1 and 9, suggesting that poor context discrimination caused by elevated LC activity is associated with a lack of a shift in DG-GC neuron activity towards context B (safe; **Fig. 3.1M**).

We next investigated the DG-GC ensemble shifts in Th-Cre$^{LC\text{-}DG}$::HM3Dq mice when looking only at cells that were identified both at the beginning and the end of training (**Fig. 3.2J**). Within this stably tracked population of neurons, we observed that over the course of training there is a significant decrease in neurons responding to context A (unsafe), and an increase in neurons responding to context B (safe) (**Fig. 3.2L**). We also examined shifts in individual cell selectivity over the course of the training to determine whether neurons tended to shift from a particular selectivity at the beginning of training to a different selectivity at the end of training (**Fig. 3.2K**). This was done by dividing neurons into nine different categories based on their selectivity on day 1 and day 9 of training. A

moderate percentage (~31%) of neurons responding selectively to context A (unsafe) at the beginning of training remained selective to context A at the end of training, while a high percentage (~39%) of neurons responding selectively towards context B remained selective to context B at the end of training. These results corroborate our other findings regarding the failure of the DG GC ensemble to shift towards the safe context over the course of training.

Comparing normalized cumulative distributions of cell selectivity, we found a significant shift in responsiveness towards context B over the course of the CFD task in wild-type controls, but not in Th-Cre$^{LC\text{-}DG}$::HM3Dq mice, whose responsiveness remains stable throughout training. (**Fig. 3.2M**). This further supports the conclusion that elevated LC activity during CFD training prevents recruitment of new DG GCs in context B (safe).

3.4 Discussion

In this chapter, we demonstrate DG neural ensemble recruitment that shifts as mice are able to successfully discriminate between the safe and unsafe contexts in our CFD paradigm. This supports the notion that sparse firing from DG GCs responds to specific environments, and distinct subsets of GCs will respond to different contexts and environmental cues (GoodSmith et al., 2017; Hainmueller and Bartos, 2018). Additionally, it is likely that there are two types of contextual encoding occurring during this CFD task; neurons that remap over the course of training, and recruitment of immature adult-born GCs. Among the neurons that were reliably tracked across multiple days, there was a significantly higher number of neurons that responded selectively to context B on day 9 compared to day 1. Additionally, of these neurons, a large proportion shifted selectivity from responding to context A at the beginning of training, to responding to context B at

the end of training. This suggests that some neurons that responded on day 1 underwent remapping during CFD, as the mice underwent contextual learning. Additionally, DG neural ensemble shifts may also be due to adult neurogenesis, wherein new adult-born GCs, which display heightened excitability and synaptic plasticity and respond more strongly towards external stimuli compared to their mature counterparts, may be aiding in discrimination of similar memories (Denny et al., 2012; Marín-Burgin et al., 2012; Schmidt-Hieber et al., 2004; Zhuo et al., 2016). As the mice undergo CFD, new GCs may be responding selectively to new information that is learned, in this case that context B is the safe context and that there is no foot shock delivered in that context, aiding in successful disambiguation of the two contexts. These findings are consistent with prior research suggesting that not only does DG makes use of adult neurogenesis to tune immature adult-born GCs to specific experiences, but that indexing of distinct populations of DG neurons towards specific memories may be facilitated by gradual activity changes in these DG granule cells, rather than by completely distinct sets of neurons (Hainmueller and Bartos, 2018; Miller and Sahay, 2019; Senzai and Buzsáki, 2017; Teyler and DiScenna, 1986).

We also show a prevention of pattern separation that is evident from differences at the ensemble level in the DG in the reliably tracked and the general population of identified cells (**Fig. 3.1K-P, Fig. 3.2F-M**). These results may suggest that as these mice struggle to disambiguate the cues distinguishing the two separate contexts, the DG ensemble similarly struggles and reacts unpredictably, with many cells switching selectivity in a disorganized fashion. While mice with poor discrimination of the contexts due to chemogenetic excitation did have an overall greater proportion of cells with context

selectivity than wild-type animals, this may be due to a general increase in activation of DG granule cells produced by pretreatment with CNO prior to training. Additionally, when considering the tracked cell population, it is important to note that this likely does not fully capture DG ensemble shifts, as new cells may be recruited over the course of training to recognize distinct contextual cues. Finally, because of imaging variability of different animals with respect to GCaMP viral expression and the high variability of neurons imaged from each mouse, it is difficult to compare across groups to power a statistical analysis of proportions.

Lastly, one of the limitations of this study was the use of chemogenetic tools to activate the LC-NE system. In previous experiments, we were able to selectively target LC-NE terminals in the DG via optogenetic manipulations, leading to either impairment or facilitation in the CFD task via activation or inhibition of these terminals. However, because of the need for the GRIN lens implant and miniscope to conduct 1-photon calcium imaging, it was not possible to repeat those identical manipulations. Thus, the use of DREADDs was required, allowing us to activate the LC-NE system. However, this activation is not as spatiotemporally specific as optogenetic manipulations, meaning that there may be other signaling mechanisms impacting DG neural ensemble recruitment during contextual learning. Further studies must be done with newer technologies that have improved specificity, such as the nVoke system (Inscopix) that allows for simultaneous calcium imaging and optogenetic manipulation, in order to further elucidate the role of LC-NE projections in modulating DG neural ensemble activity during contextual aversive processing.

Chapter 4. Optical Stimulation of β-Adrenergic Receptor-like Signaling On Inhibitory Interneurons Impairs Contextual Fear Discrimination

4.1 Introduction

Thus far, we have demonstrated that bidirectional manipulation of the LC-DG projection results in opposing learning states, and that increased LC-NE activity impairs recruitment of the DG neural ensemble and results in contextual generalization. These findings significantly further our understanding of LC-NE mediated DG pattern separation during aversive contextual processing. Here, we aim to elucidate the role of downstream adrenergic receptor (AR) subtypes in the DG that may be involved in contextual discrimination.

In total, there are nine known AR subtypes: α_{1A}, α_{1B}, α_{1D}, α_{2A}, α_{2B}, α_{2C}, β_1, β_2, and β_3 (Strosberg, 1993). These AR subtypes on found across the brain and spinal cord on neurons, glia, immune cells, and brain vasculature, although further work must be done to characterize the density and distribution of these subtypes (MacDonald and Scheinin, 1995; Molinoff, 1984). β_2 is abundant in the hippocampus, while a genetic variant of this AR subtype has been shown to prolong NE binding and is commonly found in those suffering from PTSD (Liberzon et al., 2014; Poe et al., 2020). Moreover, NE release in the hippocampus results in enhancements to contextual learning and everyday memory, as well as changes in synaptic plasticity via β-AR dependent modulation (Hansen and Manahan-Vaughan, 2015; Takeuchi et al., 2016; Wagatsuma et al., 2018). Other studies have supported the notion that the adrenergic nervous system mediates emotion-related memory consolidation and reconsolidation (Gazarini et al., 2013; Otis et al., 2015). Additionally, one model suggests that different affinities of NA receptors are important in

driving optimal performance in behavioral tasks, wherein intermediate levels of NE bind to high-affinity α_2-ARs in support of executive functions, and higher concentrations of NE result in activation of α_1- and β-ARs to promote flight-or-flight behaviors (Arnsten, 2000; Arnsten, 2011). However, what remains unclear is the specific downstream adrenergic receptor targets of LC-NE in the DG that are involved in pattern separation and aversive contextual processing in PTSD-like behavior.

In this chapter, we conduct an integrated neuromodulatory circuit analysis approach, using slice electrophysiology, and combining opto- and chemogenetic tools with a well-established Pavlovian contextual fear discrimination (CFD) paradigm in which animals were placed in two similar, but different, contexts daily (Danielson et al. 2016; Lovett-Barron et al., 2014; McHugh et al., 2007). We also use a chimeric rhodopsin/β_2 adrenergic receptor (opto-β_2AR) that is similar in dynamics to endogenous β-AR signaling in terms of cAMP generation, MAP kinase activation and receptor internalization (Siuda et al., 2015). Through the use of these techniques, we elucidate the role of β-AR signaling activation on GABAergic interneurons in the DG hilus in aversive contextual processing, wherein binding of NE on these hilar interneurons inhibits DG GCs and impairs aversive contextual processing.

4.2 Methods

4.2.1 Animals

Adult (25-35 g) male *vGAT*-IRES-Cre mice, *vGlut1*-IRES-Cre mice, and Cre (-) littermate control mice were used for projection mapping and all *in vivo* experiments after backcrossing to C57BL/6J mice for at least 10 generations. Mice were group housed, given access to food pellets and water *ad libitum*, and maintained on a 12:12-hour

light/dark cycle (lights on at 7:00 a.m.). Animals were held in a sound attenuated holding room facility in the lab starting at least one week prior to surgery, as well as post-surgery and throughout the duration of behavioral assays to minimize stress from transportation and disruption from foot traffic. All mice were handled and, where appropriate, connected to fiber optics two times a day for one week prior to behavioral experimental testing. All experimental procedures were approved by the Animal Care and Use Committee of Washington University and the Animal Care and Use Committee of University of Washington and conformed to NIH guidelines.

4.2.2 Stereotaxic surgery

All surgeries were performed under 4% isoflurane anesthesia (Piramal Healthcare, Maharashtra, India). To stimulate DG cell types via β-adrenergic receptor signaling, 400 nl of the light sensitive chimeric rhodopsin/β_2-adrenergic receptor AAV5-EF1α-DIO-Opto-β_2AR-YFP was injected bilaterally into the DG (AP: -2.2 mm, ML: ±1.4 mm, DV: -2.1 mm) using a Hamilton syringe with blunted needle. Four to five weeks after virus injection, fiber optic ferrules were chronically implanted above the DG (AP: -2.2 mm, ML: ±1.4 mm, DV: -1.65 mm), and dental cement (Lang Dental, Wheeling, IL) was applied to hold the ferrules in place. For electrophysiological recordings, adult mice were injected bilaterally with 400 nl of AAV5-EF1α-DIO-eYFP into the DG (AP: -2.2 mm, ML: ±1.4mm, DV: -2.1 mm). Mice were allowed to recover for at least six weeks following infusion of virus prior to further behavioral testing to ensure optimal viral expression and implant placement location (**Fig. S2A**).

4.2.3 Contextual fear discrimination behavioral task

We used a well-established Pavlovian contextual fear discrimination (CFD) paradigm in which animals were placed in two similar, but different, contexts daily (Danielson et al. 2016; Lovett-Barron et al., 2014; McHugh et al., 2007). Fear conditioning took place in Med-Associates conditioning chambers that consisted of one clear plexiglass wall, three aluminum walls, and a stainless-steel grid as a floor. The training chamber was housed in a sound attenuated cubicle. Context A was rectangular, with floors made of stainless-steel rods (2 mm diameter, spaced 5 mm apart), walls of aluminum and acrylic, and cinnamon extract scent, and was cleaned with 70% ethanol between runs. Context B differed from context A in that it had a white acrylic floor and a wall decorated with a black and white striped pattern. Context B was cleaned with multi-purpose surface cleaner (Method, UPC: 817939000106) between runs, and scented with peppermint extract. All sessions were recorded from the side using a digital camera and were scored for freezing by an investigator blind to the genotype of the animal.

Mice were handled for 5 minutes per day for a week prior to training. Contextual fear discrimination training took place in the apparatus described above. In context A (unsafe context), animals were placed in the conditioning chamber and allowed to freely explore for 180 seconds, after which they received a single 2 second foot shock of 0.50 mA. Mice were taken out 15 seconds after termination of the foot shock and returned to their home cage. In context B (safe context), mice were allowed to freely explore the context for 197 seconds, the same amount of total time that they were in context A, and then returned to their home cage. In this context, no foot shock was delivered. All freezing in both contexts was assessed for the first 180 seconds, and the last 17 seconds were

not included in the behavioral analysis. Freezing was done in a double-blind fashion to avoid bias in manual scoring.

On the first day (Day 0) of CFD training, all animals were placed in context A and received a foot shock. The next day (Day 1), mice were run first in context B with no foot shock, then in context A with a foot shock. There was a minimum 3-hour period between exposure to context A and context B. This training protocol was repeated daily for 9 days.

4.2.4 Pharmacological and optogenetic manipulation of β-AR and β-AR-like signaling.

When conducting β-AR loss of function experiments (**Fig. 4.1C**), mice injected with DREADD virus were allowed to recover for 4 weeks after surgery before habituation. During habituation, mice received an i.e. injection of saline to habituate them to the injection process, after which they were placed back in the home cage. On each test day, mice were injected with either saline or Propranolol (10 mg/kg, i.p., 1 hour prior) followed by CNO (5 mg/kg, i.p., 30 minutes prior) before CFD training, after which they were placed back in their home cage. After 30 minutes, they were placed into the behavioral chamber to undergo CFD training.

When conducting optogenetic manipulation of Opto-β_2, following stereotaxic surgery and implantation of a fiber optic implant above the DG mice were connected to a 473 nm diode-pumped solid-state laser (OEM Laser Systems). Laser power was adjusted to obtain ~15 mW transmittance into the brain. For mimicking of endogenous β-like signaling via Opto-β_2, 473 nm wavelength light was pulsed for 5s on/off.

4.2.5 Electrophysiological recordings

Coronal brain slices were prepared at 250 μM on a vibrating Leica VT1000S microtome using standard procedures. Mice were anesthetized with Euthasol (Virbac, Westlake Texas), and transcardially perfused with ice-cold and oxygenated cutting solution consisting of (in mM): 93 N-Methyl-D-glucamine (NMDG), 2.5 KCL, 20 HEPES, 10 MgSO4·7H20, 1.2 NaH2PO4, 0.5 CaCl2·2H20, 25 glucose, 3 Na^+-pyruvate, 5 Na^+-ascorbate, and 5 N-acetylcysteine. Following collection of coronal sections, the brain slices were transferred to a 34°C chamber containing oxygenated cutting solution for a 10-minute recovery period. Slices were then transferred to a holding chamber consisting of (in mM) 92 NaCl, 2.5 KCl, 20 HEPES, 2 MgSO4·7H20, 1.2 NaH2PO4, 30NaHCO3, 2 CaCl2·2H20, 25 glucose, 3 Na-pyruvate, 5 Na-ascorbate, 5 N-acetylcysteine and were allowed to recover for ≥ 30 min. For recording, slices were perfused with oxygenated artificial cerebrospinal fluid (ACSF; 31-33°C) consisting of (in mM): 113 NaCl, 2.5 KCl, 1.2 MgSO4·7H20, 2.5 CaCl2·6H20, 1 NaH2PO4, 26 NaHCO3, 20 glucose, 3 Na^+-pyruvate, 1 Na^+-ascorbate, at a flow rate of 2-3ml/min. 50mM Propranolol Hydrochloride and 5mM Isoproterenol Hydrochloride was made fresh each day in ddH_2O and added to either the HEPES or ACSF in a 1:1000 ratio for a final concentration of 50μM and 5μM, respectively.

Fluorescently labeled VGAT+ neurons in the DG were identified using a Thorlabs LEDD1B T-Cube driver at 40x magnification with an immersion objective with differential interference contrast (DIC) microscopy. DG neurons were initially voltage clamped in whole-cell configuration using borosilicate glass pipettes (2-4MΩ). filled with internal solution containing (in mM): 125 K^+-gluconate, 4 NaCl, 10 HEPES, 4 MgATP, 0.3 Na-GTP, and 10 Na-phosphocreatine (pH 7.30-7.35). For all experiments, neurons were

clamped at −70mV and 50 μM picrotoxin (Cayman Chemical, Ann Arbor, Michigan) was included in the patch pipette. Following break-in to the cell, we waited ≥ 3 minutes to allow for exchange of internal solution and stabilization of membrane properties. Neurons with an access resistance of > 30MΩ or that exhibited greater than a 20% change in access resistance during the recording were not included in our datasets. After allowing the neurons to stabilize following break in, they were switched into current-clamp mode for the collection of the data presented in Figure 4.3. Cells that showed spontaneous firing activity or fired prior to depolarization steps were excluded from the data set.

4.2.6 Statistical analysis

All data are expressed as mean ± SEM. Behavioral data were analyzed with JMP12 Pro (SAS institute, Cary, NC, RRID:SCR_014242) and GraphPad Prism 8.0. *Student's t*-test, one-way or two-way ANOVAs were used to analyze between-subjects designs. Repeated-measures designs were analyzed using mixed-effects restricted maximum likelihood (REML) model. Tukey was used for *post-hoc* pairwise comparisons. The null hypothesis was rejected at the $p < 0.05$ level. Statistical significance was taken as $*p < 0.05$, $**p < 0.01$, $***p < 0.005$, *n.s.* represents not significant. All statistical information is listed in Table S1.

4.3 Results

The impairment of contextual discrimination learning with the activation of the LC-NE system was somewhat unexpected, because it contradicts the view that the LC circuit network facilitates cognitive function and hippocampus dependent memory in general (Mair et al., 2005; Kempadoo et al., 2016; Sara, 2009; Takeuchi et al., 2016; Wagatsuma et al., 2018). To that end, we then attempted to understand the specific mechanisms by

which the LC-NE system modulates CFD and hippocampal function. To drive chemogenetic activation of the LC-DG circuit, we used transgenic mice expressing Cre-recombinase driven by dopamine beta-hydroxylase (Dbh-Cre), injected with a Cre-dependent excitatory DREADD (**Fig. 4.1A-B**). In this CFD task, animals were injected with CNO intraperitoneally 30 minutes prior to the task each day and starting on the fifth day animals received intraperitoneal injections of either saline or β-selective antagonist propranolol prior to CNO (**Fig. 4.1C**) (Stadel and Lefkowitz, 1991).

In this CFD task, animals with chemogenetic activation of the LC-DG circuit receiving saline injections were unable to discriminate between context A (unsafe) and

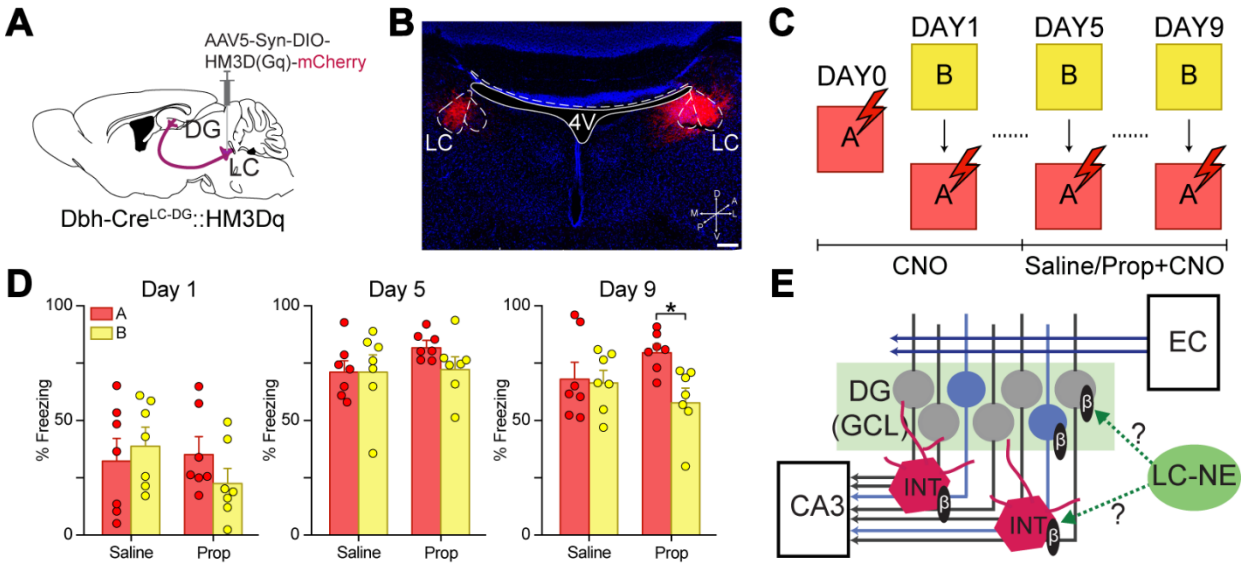

Figure 4.1. Pharmacological modulation of noradrenergic signaling in DG interneurons and GCs during contextual fear discrimination.
(**A**) Schematic of experimental approach depicts infection of LC-NE cells using Dbh-Cre mouse line with DREADD system activating HM3Dq signaling chemogenetically. (**B**) Representative image depicting expression of HM3Dq in LC-NE cells of Dbh-Cre mice. Scale bar = 50 µm. (**C**) CFD task with CNO injection 30 minutes prior to task. Starting on day 5, animals received injection of either saline (Dbh-Cre::Saline) or propranolol (Dbh-Cre::Prop) 30 minutes prior to CNO injection. (**D**) Chemogenetic activation of the LC-NE system impairs behavioral pattern separation in mice receiving saline prior to CNO (n = 7), but not in those that received propranolol prior to CNO (n = 7). Animals receiving propranolol prior to CNO were able to successfully discriminate on the ninth day of training, but animals receiving saline prior to CNO were not. (**E**) Diagram depicts hypothesis regarding potential LC-DG circuitry. Neurons in the Entorhinal Cortex (EC) send projections to the DG through the perforant pathway. The DG sends projections to pyramidal cells in the CA3 through mossy fibers. LC-NE projections may modulate granule cells (GC) directly during a new experience, or may modulate local interneurons (INT), causing strong tonic inhibition of GCs. All data are mean ± SEM. *$p < 0.05$.

context B (safe) across all phases of training (**Fig. 4.1D**). Meanwhile, animals with chemogenetic activation of the LC-DG circuit receiving β-selective antagonist propranolol inje ctions successfully discriminated between the two contexts on day 9 of training. This result suggests that modulation of aversive contextual memory occurs via norepinephrine engagement of β-signaling in the DG, while blocking these receptors leads to recovery of discrimination ability even with activation of the LC-NE system.

Based on the results above, we considered several possible explanations for how the LC-NE system may be influencing the DG neural ensemble during CFD (**Fig. 4.1E**). Evidence exists that β-adrenergic receptors are critical for establishing LC-NE synaptic plasticity in the DG (Lethbridge et al., 2014; Hagena et al., 2016; Walling and Harley, 2004), and thus represent a likely candidate for the altered recruitment of DG ensembles by LC-NE input.

We therefore examined the expression of Adrb2 on different cell types in the DG. *In-situ* hybridization revealed that most $vGAT^+$ interneurons in the DG (~85%) express β_2-AR mRNA, as do most $vGlut1^+$ neurons in the DG-GCL (~85%) (**Fig. 4.2A-B**). Because Adrb2 is heavily co-expressed with both vGat and vGlut1 in the DG, we posited that LC-NE projections synapsing onto one or both cell types could be modulating contextual generalization in response to LC-NE release into the DG. To evaluate the role of selective engagement of β_2-AR signaling on excitatory neurons in the GCL in modulating performance in the CFD task, we used an AAV virus we previously developed with a DIO construct containing the photo-sensitive β_2-AR-YFP (**Fig. 4.2C**). Due to the complexity of expression and temporal limitations of pharmacological approaches in this CFD task to isolate specific receptors in the region, this tool afforded us localized control of signaling,

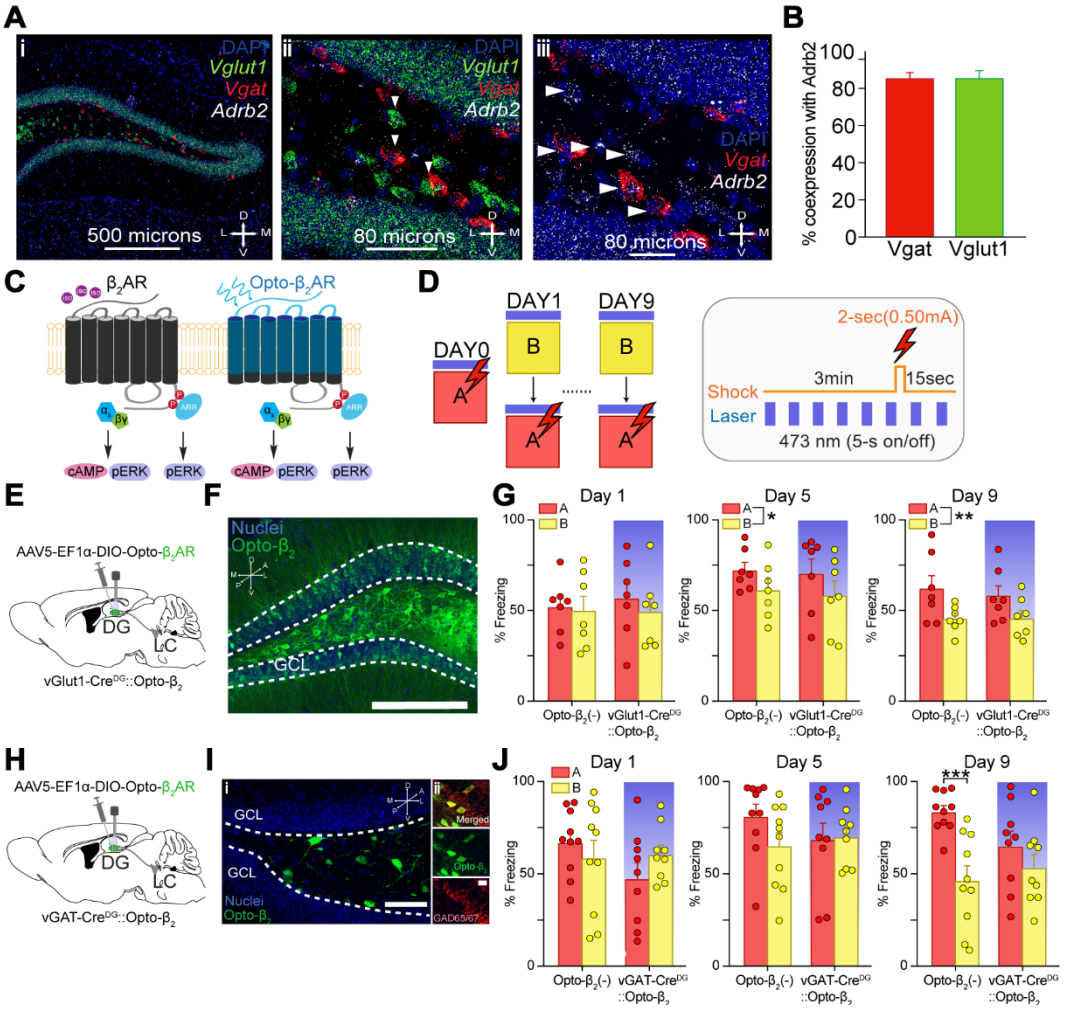

Figure 4.2. Optogenetic modulation of noradrenergic signaling in DG interneurons and GCs during contextual fear discrimination.

(**A**) *In-situ* hybridization depicting coronal images of colocalization of *Adrb2* (white), *Vglut1* (green), and *Vgat* (red) within the DG of wild-type mice. (**B**) Quantification of *Vgat* and *Vglut1* coexpression with Adrb2. (**C**) Diagram depicts intracellular pathway of Opto-β2 adrenergic receptors (ARs). (**D**) CFD task with optogenetic β2-AR modulation of DG GCs or interneurons (left). Pattern of laser stimulation and shock (only in context A) during CFD (right). (**E**) Schematic of experimental approach depicts infection of DG GCs using vGlut1-Cre mouse line with chimeric light-sensitive adrenergic receptors (vGlut1-Cre^{DG}::Opto-β2). (**F**) Opto-β2 ARs were expressed in the GCL. Scale Bar = 200 μm (**G**) Acute photoactivation of Opto-β2 ARs in DG GCs did not impair discrimination in mice expressing Opto-β2 in LC-DG projections or wild-type controls. Opto-β2(-) controls (n = 7) were able to discriminate on the ninth day of training, and vGlut1-Cre^{DG}::Opto-β2 mice (n = 7) were also able to discriminate on the ninth day of training. Both groups received optogenetic light during trial, shaded bar denotes successful stimulation of opsin. (**H**) Schematic of experimental approach depicts infection of DG interneurons using vGAT-Cre mouse line with chimeric light-sensitive adrenergic receptors (vGAT-Cre^{DG}::Opto-β2). (**I**) Opto-β2 ARs were expressed in the hilus area (left) and co-expressed with GAD67 (right). Scale Bars = 50 μm (left), 15 μm (right). (**J**) Acute photoactivation of Opto-β2 ARs in DG interneurons impaired discrimination in mice expressing Opto-β2 in LC-DG projections but not in wild-type controls. Opto-β2(-) controls (n = 10) were able to discriminate on the ninth day of training, while vGAT-Cre^{DG}::Opto-β2 mice (n = 9) were not able to discriminate throughout the training. Both groups received optogenetic light during trial, shaded bar denotes successful stimulation of opsin. All data are mean ± SEM. *$p < 0.05$, ***$p < 0.005$.

and we have previously demonstrated that it mimics β-AR signaling in vitro and in vivo (Siuda et al., 2015). To selectively target vGlut1^{+} neurons in the GCL, we used transgenic mice expressing Cre-recombinase driven by vesicular glutamate transporter 1 (vGlut1-Cre) (**Fig. 4.2D-F**). With this neuromodulatory optogenetic approach, photostimulation of Opto-β_2 acts to mimic β_2-AR signaling in granule cells during the CFD task.

In the CFD task, both the control group (Opto-β_2(-)) and mice with acute activation of the Opto-β_2-AR (vGlut1-Cre^{DG}::Opto-β_2) in GC showed similar levels of freezing in context B (safe) and context A (unsafe) at the beginning of training (**Fig. 4.2G**). However, by the end of training, both groups of mice were able to successfully discriminate between the two separate contexts, with both groups of mice displaying lower levels of freezing behavior in context B (safe) compared to context A (unsafe). Additionally, there were no significant differences in freezing in context A when comparing wild-type controls to vGlut1-Cre^{DG}::Opto-β_2 mice. These results indicate that activation of β_2-signaling in excitatory neurons in the DG GCL is likely not the mechanism by which the LC-NE system alters this behavior.

Considering that GCs in the DG receive strong tonic inhibition from local interneurons, one possible interpretation of the results showing enhanced discrimination is that local interneurons that tonically inhibit GCs are inhibited after suppressing NE release in the LC (**Fig. 4.1E**) (Houser, 2007). This led to the hypothesis that activation of β-adrenergic signaling within interneurons of the DG may act to impair performance in the CFD task. To assess the ability of β-signaling to alter influence the excitability of DG vGAT^{+} neurons, we first performed a series of electrophysiological experiments. Transgenic mice expressing Cre-recombinase driven by vesicular GABA transporter

(vGAT-Cre) and injected with a Cre-recombinase dependent viral vector containing YFP were used to selectively target interneurons in the DG. Using whole-cell patch clamp, we monitored evoked action potential firing in $vGAT^{+}$ neurons (YFP labeled) in the presence of the β-selective agonist isoproterenol, or the β-selective antagonist propranolol (Stadel and Lefkowitz, 1991). We found that isoproterenol significantly increased the excitability of $vGAT^{+}$ neurons at low threshold depolarizations while propranolol diminished the excitability of these neurons (**Fig. 4.3A-C**).

With these findings in mind, we targeted DG interneurons using vGAT-Cre mice in the hilus with Cre-dependent Opto-β_2-YFP (**Fig. 4.2H-I**). The control group (Opto-β_2(-)) showed significantly higher freezing in context A (unsafe) compared to context B (safe) during contextual fear discrimination. However, as training progressed, mice with acute activation of the opto-β_2-AR (vGAT-Cre^{DG}::Opto-β_2) in hilus vGAT interneurons displayed no significant differences in freezing between the two contexts (**Fig. 4.2J**). Further analysis found that, halfway through training, both groups failed to discriminate between the contexts. However, by the end of training, Opto-β_2(-) mice froze more in context A than B, in contrast to vGAT-Cre^{DG}::Opto-β_2 mice (**Fig. 4.2J**). However, vGAT-Cre mice injected with ChR2 instead of Opto-β_2 in the DG displayed a significant difference in freezing between context A and context B over the course of training, as did the corresponding wild-type controls (**Fig. S4C-E**). This indicates that inhibition of freezing in the CFD was not due solely to the presence of optogenetic stimulation, but rather the specific β-signaling driven by Opto-β_2. Additionally, quantification of Opto-β_2 infection in the GCL and hilus of vGlut1-Cre mice and vGAT-Cre mice showed sufficient infection of the GCL and low infection of the hilus in vGlut1-Cre mice, and sufficient infection of the

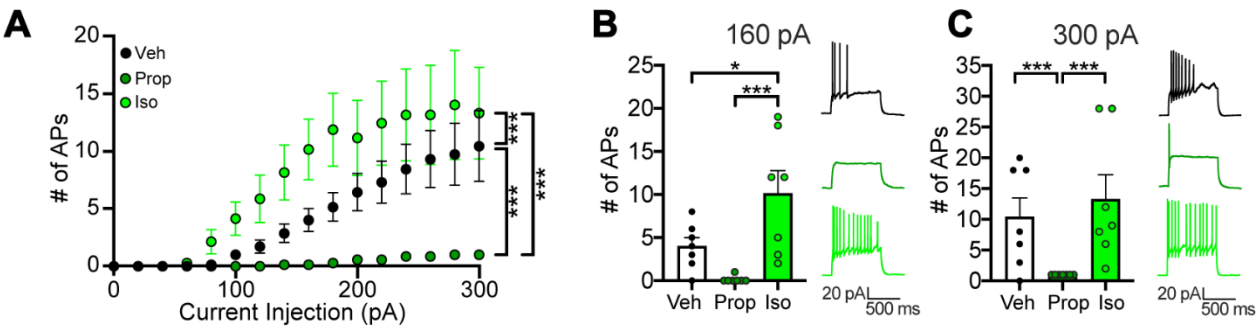

Figure 4.3. Whole cell patch clamp of action potential firing in vGAT^{+} neurons with pharmacological manipulation of adrenergic circuitry.
(**A**) Whole-cell patch clamp recordings of depolarization elicited action potential firing. 5μM Isoproterenol increased ($p<0.0001$) while 50μM Propranolol decreased ($p<0.0001$) the number of depolarization elicited action potentials (Depolarization Step: $F_{(15,288)} = 9.303$, $p<0.0001$; Drug: $F_{(2,288)} = 59.84$, $p<0.0001$; Depolarization Step x Drug: $F_{(30,288)} = 2.207$, $p = 0.0005$). (**B**) Comparison of action potential firing between vehicle, isoproterenol, and propranolol at 160 pA depolarization step (Veh vs Iso: $p=0.0385$; Prop vs Iso: $p=0.0005$). (**C**) Comparison of action potential firing between vehicle, isoproterenol, and propranolol at 300 pA depolarization step (Veh vs Prop: $p=0.0007$; Veh vs Iso: $p=0.2752$; Prop vs Iso: $p<0.0001$). All data are mean ± SEM. *$p < 0.05$, ***$p < 0.005$.

hilus and low infection of the GCL in vGAT-Cre mice (**Fig. S4F-G**). Lastly, we found no significant differences in freezing in context A when comparing wild-type controls to vGAT-Cre^{DG}::Opto-β_2 mice. These results indicate that activation of β-AR signaling on vGAT neurons results in impaired CFD, consistent with the hypothesis that local interneurons in the DG are regulated by noradrenergic signaling, to regulate distinguishing of similar information from prior stressful experiences.

4.4 Discussion

Although the current study suggests that β-adrenergic signaling on inhibitory interneurons plays a major role in the exaggerated fear generalization, the question remains whether β-adrenergic signaling on the interneurons is the exclusive neuromodulatory actor causing fear generalization. Previous studies demonstrated that the primary effect of NE on the GCs in the DG and pyramidal cells in the CA1 is inhibitory and mediated by α_1-adrenergic receptors (Pang and Rose, 1987; Rose and Pang, 1989). It is possible that the failure in discrimination with excessive NE release is due to a

synergistic effect of the activation of both α_1- and β_2-adrenergic pathways resulting in suppression of the GCs overall. These possibilities will need to be tested in future studies at synaptic, cell, and microcircuit levels using high-resolution conditional knockdown approaches. In addition, when we injected ChR2 instead of Opto-β_2 in the DG of vGAT-Cre mice, the modulation effect in CFD was not detected (**Fig. S4C-E**). However, an interesting question remains regarding how this distinct outcome relates to differences in local signaling and resulting physiological changes between the two photo-induced receptors (Opto-β_2 vs. ChR2) in different cell types.

Reports examining catecholamine modulation of prefrontal cortical (PFC) cognitive function have suggested that there is an optimal level of catecholamine to achieve the best cognitive performance. Under stress-free conditions, animals with a pharmacological blockade of α_2-adrenergic receptors (e.g., yohimbine), which have high affinity to the NE in the dorsolateral prefrontal cortex, experienced impaired working memory performance (Arnsten, 2011). Conversely, pharmacological activation of postsynaptic α_2-adrenergic receptors (e.g., guanfacine) in that region improved working memory performance (Franowicz et al., 2002). Meanwhile, the high levels of NE release induced by stressors suppressed neuronal firing in the PFC via α-1 and β-1 adrenergic receptors, which have low affinity for NE and are thus less likely to get activated in an unstressed condition (Arnsten, 2009; Berridge and Spencer, 2016). While extensive studies have supported this inverted U-shaped relationship between the LC-NE system and PFC dependent working memory performance using operant conditioning paradigms, here we provide evidence that the facilitation of LC-NE cells projecting to the DG impairs contextual fear discrimination and facilitates contextual fear generalization.

The fundamental microcircuit structure in the DG involved in pattern separation is likely quite different from recurrent circuits (pyramidal cell to pyramidal cell) in the PFC involved in working memory (**Fig. 4.1E**) (Treves et al., 2008). Therefore, the acting mechanism of the LC-NE system on the DG may be different at the synaptic, cellular, or microcircuit level from the LC-PFC system, and we propose a new mechanism here whereby LC-NE driven inhibitory tone on the GCs prevents pattern separation.

Additionally, there are many studies that implicate β-adrenergic receptors on shaping both LTP and LTD in the DG (Cox et al., 2008; Lethbridge et al. 2014; Milner et al., 2000). Evidence suggests that β-adrenergic activation in the hippocampus induces LTP of perforant path input to the DG (Lethbridge et al., 2014). Few studies have implicated behavioral changes in selected cell types to β-adrenergic signaling in the manner that we have done here. However, it remains unclear the mechanisms by which β-adrenergic signaling modulates hippocampal activity during learning and memory. Recent studies have shown enhanced cognitive performance with LC activation of different regions of the hippocampus, but these studies have not demonstrated the U-shaped curve relationship (Kaufman et al., 2020; Wagatsuma et al., 2018). Therefore, future efforts to understand the relationship that LC-NE release concentration and kinetics have on β-adrenergic signaling onto inhibitory interneurons in the DG. New biosensor tools may help to resolve these issues more definitively (Feng et al., 2019).

The current study provides a better understanding of the neuromodulatory mechanisms underlying fear discrimination and may help guide the development of unique therapeutic strategies using currently available noradrenergic ligands for targeting

psychiatric disorders characterized by generalization such as is the case in PTSD, and schizophrenia (Lisman et al., 2008; Sammer et al., 2011; Shohamy et al., 2010).

Chapter 5. Prolonged Norepinephrine Release in the Dentate Gyrus Modulates Aversive Contextual Processing

5.1 Introduction

Every day, people must consistently engage in contextual learning processes such as pattern separation and contextual discrimination, as they experience new episodic events and compare this novel information to previous experiences. These processes are critical for normal functioning and deficits in this functioning are thought to underlie multiple disease states including post-traumatic stress disorder (PTSD) and schizophrenia (Liberzon and Abelson, 2016; Lisman et al., 2008; Shohamy et al., 2010). These disorders are characterized by a dysregulation of pattern separation, and individuals with these disorders often experience elevated levels of fear and anxiety resulting from failures in contextual processing between incoming episodic information and existing memories, hypervigilance, and exaggerated threat detection (Besnard and Sahay, 2016; Kheirbek et al., 2012; Siegmund and Wotjak, 2006). Current therapeutic strategies to treat the resulting disorders are limited, although adrenergic receptor antagonists are used to some effect (Raskind et al., 2003; Taylor et al., 2008). Therefore, further research must be done to further elucidate the neural mechanisms behind contextual processing to better develop therapeutic treatments for stress-related disorders such as PTSD and schizophrenia.

The hippocampus is a critical neural structure in learning and memory, involved in processing of incoming environmental information (Deng et al., 2013; Lisman et al., 2017; McHugh et al., 2007; Woods et al., 2020). Moreover, the dentate gyrus (DG), a subregion of the hippocampus, has been particularly linked to contextual learning and pattern

separation, wherein information from existing memories is compared to new incoming information (Marr, 1971; Morris, 2006; O'Reilly and McClelland, 1994; Seo et al., 2021). Additionally, the DG is highly modulated by stress and aversive stimuli (Britton et al., 1992; Campeau et al., 2010; Fa et al., 2014). However, it is unclear how exactly disrupted memory retrieval and failures in pattern separation that give rise to contextual generalization occur in response to these aversive stimuli.

One potential source of modulation for the DG is the locus coeruleus (LC), which provides dense innervations to the DG (Blackstad et al., 1967; Ungerstedt, 1971). The LC, also known as the 'blue spot', is a small region located in the brain stem that supplies the mammalian brain with norepinephrine (NE) and has been implicated in regulation of anxiety (McCall et al., 2015; McCall et al., 2017; Uematsu et al., 2017; Valentino and Van Bockstaele, 2008). LC-NE tonic activity increases in response to stressful events, leading to modulation of many brain structures, including the DG (Harley, 2007; Loy et al., 1980; Rose and Pang, 1989; Seidenbecher et al., 1997; Walling and Harley, 2004). However, it is not known the exact mechanisms by which the LC-NE system modulates the DG in memory related disorders, nor what the temporal dynamics are.

Here, we conducted an integrated neuromodulatory circuit analysis approach, combining optogenetic tools, *in vivo* fiber photometry, and a novel NE-specific biosensor with a well-established Pavlovian contextual fear discrimination (CFD) paradigm in which animals were placed in two similar, but different, contexts daily (Lovett-Barron et al., 2014; Seo et al., 2021). Elucidating the spatiotemporal dynamics of LC-NE modulation of DG-dependent aversive contextual processing will provide critical information towards efforts

to combat dysregulation of contextual disambiguation in disorders such as PTSD and schizophrenia.

5.2 Methods

5.2.1 Animals

Adult (20-35 g) *Dbh*-Cre mice, and Cre (-) littermate control mice were used for projection mapping and all *in vivo* experiments after backcrossing to C57BL/6J mice for at least 10 generations. Mice were group housed, given access to food pellets and water *ad libitum*, and maintained on a 12:12-hour reverse light/dark cycle (lights on at 8:00 p.m.). Animals were held in a sound attenuated holding room facility in the lab starting at least one week prior to surgery, as well as post-surgery and throughout the duration of behavioral assays to minimize stress from transportation and disruption from foot traffic. All mice were handled and, where appropriate, connected to fiber optics two times a day for one week prior to behavioral experimental testing. All experimental procedures were approved by the Animal Care and Use Committee of University of Washington and conformed to UW National Institutes of Health guidelines.

5.2.2 Stereotaxic surgery

All surgeries were performed under 4% isoflurane anesthesia (Piramal Healthcare, Maharashtra, India). For *in vivo* fiber photometry experiments, adult mice were injected bilaterally with 800 nl of AAV5/Syn-FLEX-ChrimsonR-td-Tomato (Addgene) into the LC (AP: -5.45 mm, ML: ±1.25 mm, DV: -3.8 mm) using a Hamilton syringe with a beveled needle and injected unilaterally with 400 nl of AAV1-hsyn-GRAB-NE2m (Li Research Lab, Beijing) into the DG (AP: -2.15 mm, ML: +1.4 mm, DV: -2.1 mm) using a Hamilton syringe with a blunted needle. Transgenic controls were injected bilaterally with 800 nl of

AAV5/Syn-FLEX-ChrimsonR-td-Tomato into the LC (AP: -5.45 mm, ML: ±1.25 mm, DV: -3.8 mm) using a Hamilton syringe with a beveled needle and injected unilaterally with 400 nl of AAV5-Ef1a-DIO-EYFP (Addgene) into the DG using a Hamilton syringe with a blunted needle. Dopamine sensor controls were injected unilaterally with 400 nl of AAV9-hsyn-GRAB-DA2m (Li Research Lab, Beijing) into the DG (AP: -2.15 mm, ML: +1.4 mm, DV: -2.1 mm) using a Hamilton syringe with a blunted needle. Mice then received intracranial fiber photometry implants in the DG (AP: -2.15 mm, ML: +1.4 mm, DV: -1.7 mm), which were secured using MetaBond (C & B Metabond). Mice were allowed to recover for at least six weeks following infusion of virus and intracranial implant prior to further behavioral testing or perfusion for projection mapping to ensure optimal viral expression.

5.2.3 Contextual fear discrimination behavioral task

We used a well-established Pavlovian contextual fear discrimination (CFD) paradigm in which animals were placed in two similar, but different, contexts daily (Danielson et al. 2016; Lovett-Barron et al., 2014; McHugh et al., 2007). Fear conditioning took place in Med-Associates conditioning chambers that consisted of one clear plexiglass wall, three aluminum walls, and a stainless-steel grid as a floor. The training chamber was housed in a sound attenuated cubicle. The conditioning chambers could be configured into two distinct contexts: A and B. Context A was rectangular, with floors made of stainless-steel rods (2 mm diameter, spaced 5 mm apart), walls of aluminum and acrylic, and cinnamon extract scent, and was cleaned with 70% ethanol between runs. Context B differed from context A in that it had a white acrylic floor and a wall decorated with a black and white striped pattern. Context B was cleaned with multi-purpose surface

cleaner (Method, UPC: 817939000106) between runs, and scented with peppermint extract. All sessions were recorded from the side using a digital camera and were scored for freezing by an investigator blinded to the genotype and experimental conditions of the animal.

For *in vivo* fiber photometry during behavior tests, a rotating optical commutator (Doric) was positioned on top of the training chamber and connected to a fiber photometry recording rig (ThorLabs). Fibers were attached to the implants on the mouse for every training session.

Mice were handled for 5 minutes per day for a week prior to training. Contextual fear discrimination training took place in the apparatus described above. During a standard CFD experiment, in context A (unsafe context), animals were placed in the conditioning chamber and allowed to freely explore for 180 seconds, after which they received a single 2 second foot shock of 0.50 mA. Mice were taken out 15 seconds after termination of the foot shock and returned to their home cage. In context B (safe context), mice were allowed to freely explore the context for 197 seconds, the same amount of total time that they were in context A, and then returned to their home cage. In this context, no foot shock was delivered. On the first day (Day 0) of CFD training, animals were placed in context A and received a foot shock. The next day (Day 1), mice were run first in context B with no foot shock, then in context A with a foot shock. There was a minimum 3-hour period between exposure to context A and context B. This training protocol was repeated daily for 9 days. All freezing in both contexts was assessed for the first 180 seconds, and the last 17 seconds were not included in the behavioral analysis. Freezing was done in a double-blind fashion to avoid bias in manual scoring.

For CFD experiments using stimulation in place of salient stimuli, mice were placed in context A (unsafe context) and allowed to freely explore for 197 seconds, and received one of three stimulation parameters: low frequency (1-5 Hz) stimulation for 180 seconds, followed by high frequency (20-40 Hz) stimulation for 2 seconds, followed by no stimulation for 15 seconds; low frequency (1-5 Hz) stimulation for 180 seconds followed by no stimulation for 17 seconds; no stimulation for 180 seconds, followed by high frequency (20-40 Hz) stimulation for 2 seconds, followed by no stimulation for 15 seconds; no stimulation for 197 seconds. Mice were removed from the conditioning chamber after termination of the stimulation parameters and returned to their home cage. Stimulation frequencies were calibrated for each individual mouse based on fit to endogenous NE release dynamics in the CFD task during successful contextual discrimination.

5.2.4 Fiber photometry with $GRAB_{NE}$

Fiber photometry recordings were made throughout the entirety of the CFD training sessions. Prior to recording, an optic fiber was attached to the implanted fiber using a ferrule sleeve (Doric, ZR_2.5). Two LEDs were used to excite $GRAB_{NE}$. A 531-Hz sinusoidal LED light (Thorlabs, LED light: M470F3; LED driver: DC4104) was bandpass filtered (470 ± 20 nm, Doric, FMC4) to excite $GRAB_{NE}$ and evoke NE-dependent emission. A 211-Hz sinusoidal LED light (Thorlabs, LED light: M405FP1; LED driver: DC4104) was bandpass filtered (405 ± 10 nm, Doric, FMC4) to excite $GRAB_{NE}$ and evoke NE-independent isosbestic control emission. Prior to recording, a 300s period of $GRAB_{NE}$ excitation with 405 nm and 470 nm light was used to remove the majority of baseline drift. Laser intensity for the 470 nm and 405 nm wavelength bands were measured at the tip of the optic fiber and adjusted to ~50 μW before each day of recording. $GRAB_{NE}$

fluorescence traveled through the same optic fiber before being bandpass filtered (525 ± 25 nm, Doric, FMC4), transduced by a femtowatt silicon photoreceiver (Newport, 2151) and recorded by a real-time processor (TDT, RZ5P). The envelopes of the 531-Hz and 211-Hz signals were extracted in real-time by the TDT program Synapse at a sampling rate of 1017.25 Hz. Optogenetic stimulation was delivered using a 625nm sinusoidal LED light (Thorlabs, LED light: M625F2; LED driver DC4104) to excite LC-DG terminals expression ChrimsonR.

Custom MATLAB scripts were developed for analyzing fiber photometry data in context of mouse behavior and can be accessed via GitHub (https://github.com/BruchasLab). The isosbestic 405 nm excitation control signal was subtracted from the 470 nm excitation signal to remove movement artifacts from intracellular NE-dependent $GRAB_{NE}$ fluorescence (see Figure S3B). Baseline drift was evident in the signal due to slow photobleaching artifacts, particularly during the first several minutes of each hour-long recording session. A double exponential curve was fit to the raw trace and subtracted to correct for baseline drift. After baseline correction, the photometry trace was z-scored relative to the mean and standard deviation of the test session. The post-processed fiber photometry signal was analyzed in the context of animal behavior during contextual fear discrimination task.

5.2.5 Statistical analysis

All data are expressed as mean ± SEM. Behavioral data were analyzed with GraphPad Prism 10.0 (GraphPad, La Jolla, CA). *Student's t*-test, one-way or two-way ANOVAs were used to analyze between-subjects designs. Repeated-measures designs were analyzed using mixed-effects restricted maximum likelihood (REML) model. Tukey was used for

post-hoc pairwise comparisons. The null hypothesis was rejected at the $p < 0.05$ level. Statistical significance was taken as $*p < 0.05$, $**p < 0.01$, $***p < 0.005$, *n.s.* represents not significant. All statistical information is listed in Table S1.

5.3 Results

To elucidate spatiotemporal dynamics of NE in the DG during behavior, we first injected novel biosensor $GRAB_{NE}$, a GPCR activation-based NE sensor with high specificity for NE, into the DG (**Fig. 5.1A-B**) (Feng et al., 2019). We then implanted optic fibers above the injection sites for photometry recordings during behavioral tasks (**Fig. 5.1C**). To ensure proper expression and efficacy of the $GRAB_{NE}$ biosensor, mice underwent tail lift and foot shock tests. During tail lift, we observed a significant increase in $GRAB_{NE}$ fluorescence during the tail lift compared to YFP controls (**Fig. 5.1D-E**). This signal began to rise when the animal was first picked up by the tail, increased continuously while the animal was suspended for 20 seconds, and decreased back to baseline after the animal was returned to the ground. This outcome matches the dynamics seen in the lateral hypothalamus during initial development and characterization of $GRAB_{NE}$ (Feng et al., 2019). During foot shock, we also observed a significant increase in $GRAB_{NE}$ fluorescence compared to YFP controls (**Fig. 5.1F-G**). This signal increased sharply during the 2 second shock and decreased rapidly back to baseline following the termination of the shock. These results indicate successful characterization of $GRAB_{NE}$ for detecting spatiotemporal dynamics of endogenous NE release from LC to DG, allowing for use in our contextual fear discrimination task. Based off these results, we then injected $GRAB_{NE}$ into the DG with optic fibers above the injection site of Dbh-cre mice, which then underwent a contextual fear discrimination task (**Fig. 5.1H**). While on

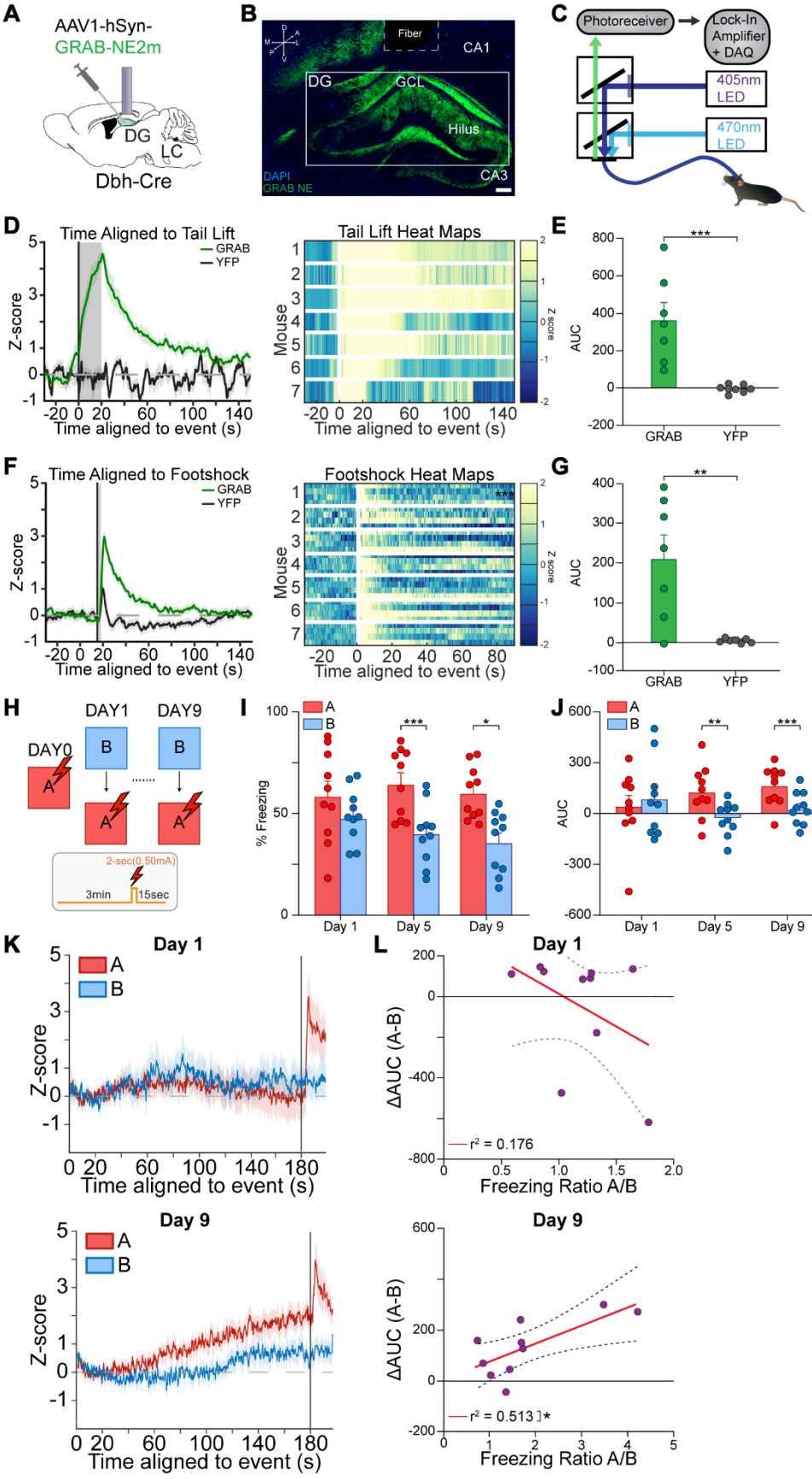
A
AAV1-hSyn-
GRAB-NE2m
DG
LC
Dbh-Cre
B
Fiber
CA1
DG
GCL
Hilus
CA3
DAPI
GRAB NE
C
Photoreceiver
Lock-In
Amplifier
+ DAQ
405nm
LED
470nm
LED
D
Time Aligned to Tail Lift
GRAB
YFP
Z-score
Time aligned to event (s)
Tail Lift Heat Maps
Mouse
Z score
Time aligned to event (s)
E
AUC
GRAB
YFP
F
Time Aligned to Footshock
GRAB
YFP
Z-score
Time aligned to event (s)
Footshock Heat Maps
Mouse
Z score
Time aligned to event (s)
G
AUC
GRAB
YFP
H
DAY0
DAY1
DAY9
A
B
2-sec(0.50mA)
3min
15sec
I
A
B
% Freezing
Day 1
Day 5
Day 9
J
A
B
AUC
Day 1
Day 5
Day 9
K
Day 1
A
B
Z-score
Time aligned to event (s)
Day 9
A
B
Z-score
Time aligned to event (s)
L
Day 1
ΔAUC (A-B)
r² = 0.176
Freezing Ratio A/B
Day 9
ΔAUC (A-B)
r² = 0.513
Freezing Ratio A/B

Figure 5.1. Endogenous NE release in DG during behavior and contextual fear discrimination
(**A**) Schematic of experimental approach depicts infection of dentate gyrus with $GRAB_{NE}$, and optic fiber implanted above the DG. (**B**) Representative image depicting expression of $GRAB_{NE}$ in DG driven by hSyn promoter and location of fiber implant. Scale bar = 100 μm. (**C**) Schematic of fiber photometry setup. (**D**) Left: Averaged trace of $GRAB_{NE}$ and YFP control fluorescence for 20 second tail lift test. Right: individual heat maps of $GRAB_{NE}$ fluorescence for 20 second tail lift test. (**E**) Area under the curve analysis for $GRAB_{NE}$ and YFP control fluorescence for tail lift test. (**F**) Left: Averaged trace of $GRAB_{NE}$ and YFP control fluorescence for 2 second foot shock. Right: individual heat maps of $GRAB_{NE}$ fluorescence for 2 second foot shock. (**G**) Area under the curve analysis for $GRAB_{NE}$ and YFP control fluorescence for 2 second foot shock. (**H**) Contextual fear discrimination (CFD) task. Animals received a shock in context A (red), but not in context B (blue) for nine days. (**I**) Mice successfully discriminated between context A (unsafe), and context B (safe) on the fifth and ninth days of training, but not on the first day of training. (**J**) Area under the curve analysis of $GRAB_{NE}$ fluorescence levels in context A and context B on the first, fifth, and ninth days of training. (**K**) Averages traces of $GRAB_{NE}$ fluorescence in context A (red) and context B (blue) for day 1 (top), and day 9 (bottom). (**L**) Linear regression using Pearson correlation for ratio of freezing behavior between context A and context B vs. difference in AUC between context A and context B (Pearson correlation for freezing ratio vs. ΔAUC: Day 1: r^2 = 0.176, p = 0.227; Day 9: r^2 = 0.513, p = 0.0198). All data are mean ± SEM. *p < 0.05, **p < 0.01, ***p < 0.005.

day 1, there were no significant differences in freezing in context A compared to context B, on day 5 and day 9 there was a significantly greater amount of freezing in context A compared to context B, indicating that mice were able to successfully discriminate between the unsafe and safe contexts following training (**Fig. 5.1I**). This difference in freezing was also accompanied by changes in NE dynamics in the DG. On day 1, these mice show no significant differences in NE dynamics during the first 180 seconds of each context, while on day 9 there is sustained release of NE throughout the duration of time in context A, while no such release is observed in context B (**Fig. 5.1K**). These mice also show increased NE release in response to the 2 second foot shock on both day 1 and day 9 or training. To quantify the amount of NE released in both context A and context B, an area under the curve (AUC) analysis was used, taking the AUC for each mouse in the first 180 seconds of both context A and context B. The amount of NE released in context A was significantly higher than in context B during the middle and late stages of training, while there was no significant difference in AUC between the two contexts in the early stages of training (**Fig. 5.1J**). These findings suggest that as the mice were increasingly

able to distinguish between the safe and unsafe contexts, there was a corresponding increase in NE release in the unsafe context compared to the safe context. To quantify a potential correlation between these two factors, we calculated a ratio between the proportion of freezing behavior in context A (unsafe) compared to context B (safe), and the change in AUC (ΔAUC) in context A (unsafe) compared to context B (safe). We used linear regression and Pearson correlation to assess the link between these parameters for both the beginning and end of training (**Fig. 5.1L**). While there is little to no relationship between the two variables at the beginning of training, by the end of the task this shifts to a significant fit between freezing ratio and ΔAUC in the two contexts. This indicates that mice that were better able to disambiguate between context A and context B also experienced higher amounts of prolonged NE release in the DG during the CFD task while in the unsafe context. These results indicate that successful discrimination between the safe and unsafe contexts in the CFD task is accompanied by a sustained increase in NE release in the DG in the unsafe context in later stages of training, once successful discrimination has occurred. Additionally, there is a significant correlation between performance in the task and amount of NE released into the DG in the unsafe context during CFD.

Following characterization of $GRAB_{NE}$ in the DG during endogenous NE release, we sought to characterize $GRAB_{NE}$ responses to evoked NE release. We injected $GRAB_{NE}$ into the DG, and Cre-recombinase dependent viral vectors containing the red shifted light-sensitive cation channel ChrimsonR into the LC of Dbh-cre mice (**Fig 5.2A-B**) (Klapoetke et al., 2014). We then implanted optic fibers above the injection sites for photometry recordings during behavioral tasks (**Fig. 5.2C**). Following this, 20 Hz pulsed

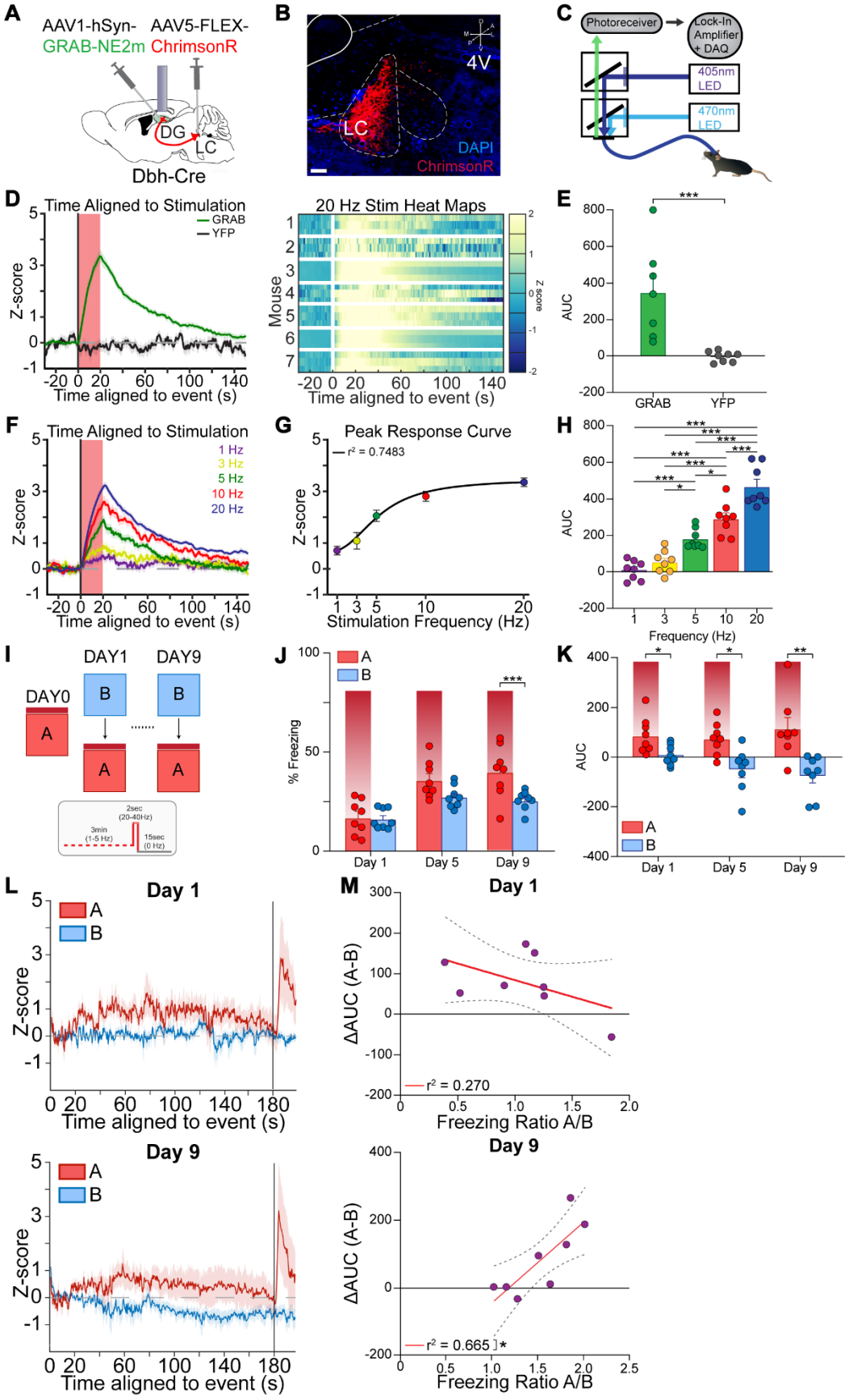
A
AAV1-hSyn-GRAB-NE2m
AAV5-FLEX-ChrimsonR
DG
LC
Dbh-Cre
B
4V
LC
DAPI
ChrimsonR
C
Photoreceiver
Lock-In Amplifier + DAQ
405nm LED
470nm LED
D
Time Aligned to Stimulation
GRAB
YFP
Z-score
Time aligned to event (s)
20 Hz Stim Heat Maps
Mouse
Z score
Time aligned to event (s)
E
AUC
GRAB
YFP
F
Time Aligned to Stimulation
1 Hz
3 Hz
5 Hz
10 Hz
20 Hz
Z-score
Time aligned to event (s)
G
Peak Response Curve
r² = 0.7483
Z-score
Stimulation Frequency (Hz)
H
AUC
Frequency (Hz)
I
DAY0
DAY1
DAY9
A
B
2sec (20-40 Hz)
3min (1-5 Hz)
15sec (0 Hz)
J
% Freezing
A
B
Day 1
Day 5
Day 9
K
AUC
A
B
Day 1
Day 5
Day 9
L
Day 1
A
B
Z-score
Time aligned to event (s)
Day 9
A
B
Z-score
Time aligned to event (s)
M
Day 1
ΔAUC (A-B)
r² = 0.270
Freezing Ratio A/B
Day 9
ΔAUC (A-B)
r² = 0.665 *
Freezing Ratio A/B

Figure 5.2. Evoked LC-DG NE release mimicking endogenous NE dynamics during contextual fear discrimination.
(**A**) Schematic of experimental approach depicts infection of dentate gyrus with $GRAB_{NE}$, optic fiber implanted above the DG, and infection of locus coeruleus with ChrimsonR. (**B**) Representative image depicting expression of ChrimsonR in LC. Scale bar = 100 μm. (**C**) Schematic of fiber photometry setup. (**D**) Left: Averaged trace of $GRAB_{NE}$ and YFP control fluorescence for 20 Hz photostimulation for 20 seconds. Right: individual heat maps of $GRAB_{NE}$ fluorescence for 20 Hz photostimulation for 20 seconds. (**E**) Area under the curve analysis for $GRAB_{NE}$ and YFP control fluorescence for 20 Hz photostimulation for 20 seconds. (**F**) Averaged traces of $GRAB_{NE}$ fluorescence for 1, 3, 5, 10 and 20 Hz photostimulation for 20 seconds. (**G**) Peak response curve for variable photostimulation. (**H**) Area under the curve analysis for $GRAB_{NE}$ fluorescence for variable photostimulation. (**I**) Contextual fear discrimination (CFD) task. Animals received stimulation in context A (red), but not in context B (blue) for nine days. (**J**) Mice successfully discriminated between context A (unsafe), and context B (safe) on the fifth and ninth days of training, but not on the first day of training. (**K**) Area under the curve analysis of $GRAB_{NE}$ fluorescence levels in context A and context B on the first, fifth, and ninth days of training. (**L**) Averages traces of $GRAB_{NE}$ fluorescence in context A (red) and context B (blue) for day 1 (top), and day 9 (bottom). (**M**) Linear regression using Pearson correlation for ratio of freezing behavior between context A and context B vs. difference in AUC between context A and context B (Pearson correlation for freezing ratio vs. ΔAUC: Day 1: $r^2 = 0.270$, $p = 0.187$; Day 9: $r^2 = 0.665$, $p = 0.0137$). All data are mean ± SEM. $*p < 0.05$, $**p < 0.01$, $***p < 0.005$.

photostimulation for 20 seconds was delivered above the DG, during which we observed a significant increase in $GRAB_{NE}$ fluorescence during stimulation compared to YFP controls (**Fig. 5.2D-E**). This signal then decreased back to baseline following termination of the stimulation parameters. We also delivered 1, 3, 5, and 10 Hz pulsed photostimulation for 20 seconds in separate trials and observed increasing levels of $GRAB_{NE}$ fluorescence with increasing levels of pulsed photostimulation of LC-DG terminals, suggesting that we are able to discreetly control evoked release of NE from LC to DG (**Fig 5.2F-H**). These results indicate successful characterization of $GRAB_{NE}$ for detecting spatiotemporal dynamics of evoked NE release from LC to DG, allowing for use in our contextual fear discrimination task. We then sought to understand how this increased and sustained release of NE in the aversive context during CFD affects discrimination and recognition during contextual discrimination. To do this, we again utilized $GRAB_{NE}$ with an optic fiber implanted in the DG, and injected ChrimsonR into the LC of Dbh-cre mice (**Fig. 5.2A-B**). These mice underwent a modified CFD task, in which

the foot shock was replaced by variable stimulation of LC-DG terminals while in context A (**Fig. 5.2I**). During the first 180 seconds of context A, mice received 1-5 Hz pulsed photostimulation, mimicking tonic firing and resulting in sustained NE release. Then, mice received 20-40 Hz pulsed photostimulation for 2 seconds, mimicking phasic bursting seen in response to foot shock. The frequencies of stimulation that mice received were tuned for each individual mouse to mimic endogenous dynamics seen during CFD as closely as possible (**Fig. 5.1J-K**). Mice that underwent this modified CFD task displayed no differences in freezing were seen between contexts in early or middle stages of training and displayed significantly increased freezing in context A compared to context B during the late stages of training, even in the absence of a salient aversive stimuli (**Fig. 5.2J**). To quantify the amount of NE released in both context A and context B, an area under the curve (AUC) analysis was used, taking the AUC for each mouse in the first 180 seconds of both context A and context B. Stimulation occurred across each day of training, with significantly higher NE levels in the aversive context during early, middle and late stages of training, suggesting that the stimulation parameters chosen were sufficient to evoke prolonged NE release in the DG in context A throughout the CFD task (**Fig. 5.2K-L**). These findings point to increased learning over the course of the CFD task, in which mice show disambiguation between the two contexts by freezing more in context A, the “unsafe” context due to increased NE release, even in the absence of an aversive stimuli. To quantify a potential correlation between these two factors, we calculated a ratio between the proportion of freezing behavior in context A (unsafe) compared to context B (safe), and the change in AUC in context A (unsafe) compared to context B (safe). We then used linear regression and Pearson correlation to assess the link between these

ratios for both the beginning and end of training (**Fig. 5.2M**). While there is no significant relationship between the two variables at the beginning of training, by the end of the task there is a significant correlation between freezing ratio and ΔAUC in the two contexts. This shows that mice that received higher amounts of prolonged NE release in the "unsafe" context also performed better by the end of training in the CFD task, learning to disambiguate the two contexts in the absence of an aversive stimuli. Furthermore, mice that received no stimulation in either of the two contexts displayed no significant differences in freezing, AUC, and correlation between freezing ratio and ΔAUC over the course of training (**Fig. S5A-E**).These results indicate that mice experience increased discrimination between two contexts based solely on increased NE release in the DG in one context, and in the absence of a salient aversive stimuli such as foot shock, and that stronger NE release is closely linked with performance in the CFD task.

We next aimed to elucidate the specific spatiotemporal NE release dynamics responsible for causing discrimination between two contexts, in the absence of a salient stimuli. In order to do this, we again utilized $GRAB_{NE}$ with a optic fiber implanted in the DG, and injected ChrimsonR into the LC of Dbh-cre mice for use in fiber photometry (**Fig. 5.3A-B**). We again used our modified CFD task, in which foot shock was replaced by variable stimulation of LC-DG terminals while in context A (**Fig. 5.3C**). In this case, we delivered only 1-5 Hz pulsed photostimulation for 180 seconds, without the 2 seconds of high frequency stimulation afterwards, to mimic only the prolonged NE release seen in context A during CFD (**Fig. 5.1J-K**). We again tuned the frequencies of stimulation that mice received for each individual mouse to mimic endogenous prolonged release dynamics seen during CFD as closely as possible. To quantify the amount of NE released

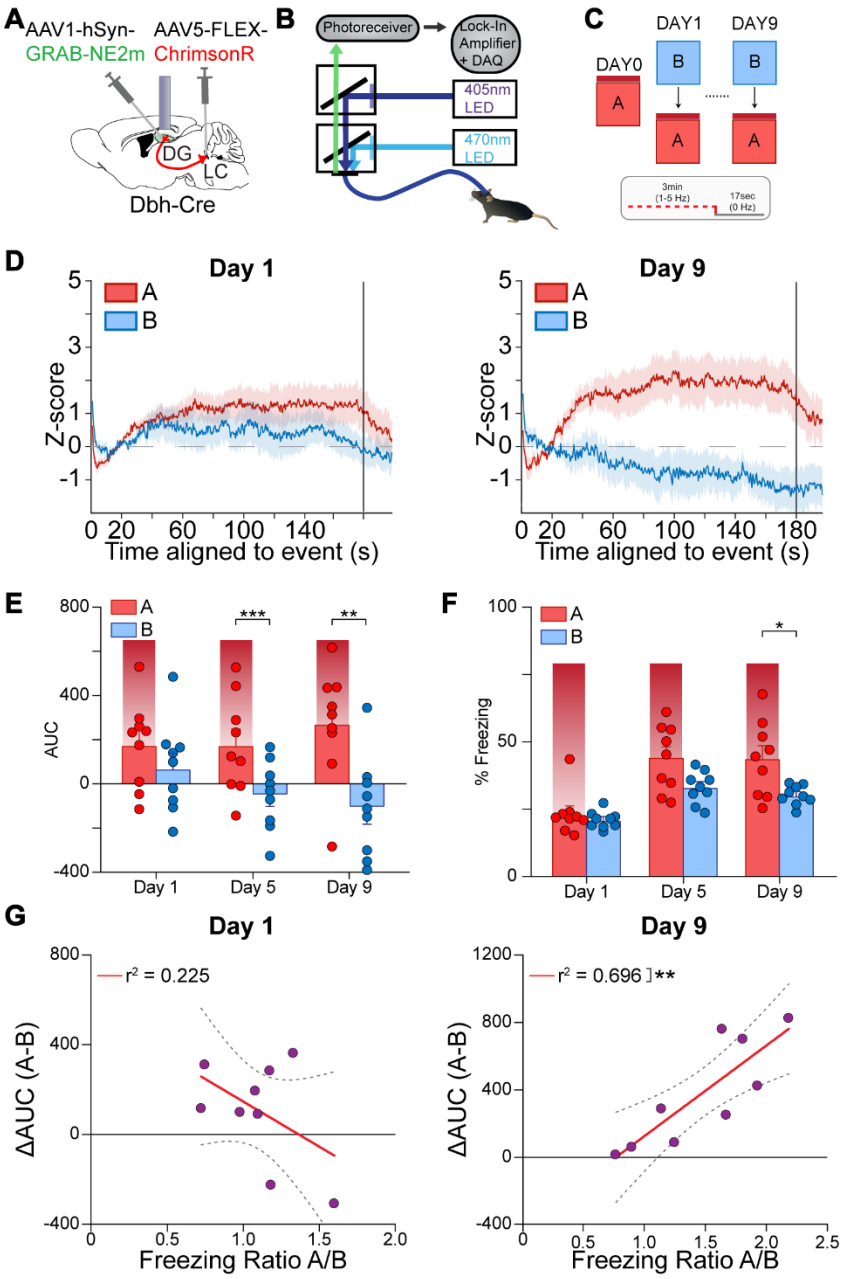

Figure 5.3. Evoked LC-DG NE release mimicking prolonged endogenous DG NE release is sufficient for contextual disambiguation.

(**A**) Schematic of experimental approach depicts infection of dentate gyrus with $GRAB_{NE}$, optic fiber implanted above the DG, and infection of locus coeruleus with ChrimsonR. (**B**) Representative image depicting expression of ChrimsonR in LC. Scale bar = 100 µm. (**C**) Contextual fear discrimination (CFD) task. Animals received stimulation in context A (red), but not in context B (blue) for nine days. (**D**) Averages traces of $GRAB_{NE}$ fluorescence in context A (red) and context B (blue) for day 1 (left), and day 9 (right). (**E**) Mice successfully discriminated between context A (unsafe), and context B (safe) on the fifth and ninth days of training, but not on the first day of training. (**F**) Area under the curve analysis of $GRAB_{NE}$ fluorescence levels in context A and context B on the first, fifth, and ninth days of training. (**G**) Linear regression using Pearson correlation for ratio of freezing behavior between context A and context B vs. difference in AUC between context A and context B (Pearson correlation for freezing ratio vs. ΔAUC: Day 1: $r^2 = 0.225$, $p = 0.197$; Day 9: $r^2 = 0.696$, $p = 0.0052$). All data are mean ± SEM. *$p < 0.05$, **$p < 0.01$, ***$p < 0.005$.

in both context A and context B, an area under the curve (AUC) analysis was used, taking the AUC for each mouse in the first 180 seconds of both context A and context B. Stimulation occurred across each day of training, only in context A, leading to significantly increased NE levels in context A compared to context B across the middle and late stages of training (**Fig. 5.3D-E**). As a result of this increased tonic-like NE release in context A, mice showed significantly increased freezing in context A compared to context B on day 9 of the CFD task, while no differences in freezing were observed on day 1 or day 5 of the task (**Fig. 5.3F**). These findings indicate that over the course of training, mice were able to discriminate successfully between context A and context B via the presence of prolonged NE release in context A, even in the absence of a salient aversive stimuli or a foot shock-like evoked NE response. Moreover, when we delivered only 2 seconds of 20-40 Hz pulsed photostimulation to mimic foot shock related phasic bursting across each day of training without 180 seconds of low frequency stimulation, no differences in freezing were observed by the end of training (**Fig. S5F-H**). These mice also displayed no differences in AUC during the first 180 seconds of training, suggesting no endogenous prolonged NE release was occurring (**Fig. S5F-I**). This suggests that prolonged tonic release of NE in the DG is sufficient to elicit successful contextual processing, while phasic bursting release of NE similar to that seen in response to foot shock is not. To quantify a potential correlation between these two factors, we again calculated a ratio between the proportion of freezing behavior in context A (unsafe) compared to context B (safe), and the change in AUC in context A (unsafe) compared to context B (safe). We used linear regression and Pearson correlation to assess the link between these ratios for both the beginning and end of training (**Fig. 5.3G**). While no significant relationship

between the two variables was observed at the beginning of training, by the end of the task this shifts to a significant correlation between freezing ratio and ΔAUC in the two contexts. Additionally, no relationship was observed between freezing ratio and ΔAUC in mice that received only 2 seconds of 20-40 Hz pulsed photostimulation throughout training in both the first and last days of training (**Fig. S5J**). These results suggest that tonic firing in response to contextual cues is the driving factor behind contextual discrimination between a safe and unsafe context, rather than phasic bursting related to the aversive stimuli. Moreover, these results support our previous findings that increased NE release in the DG is sufficient to elicit contextual discrimination, even in the absence of salient aversive stimuli.

5.4 Discussion

In this study, we report that increased LC-NE release into the DG results in successful discrimination between a safe and unsafe context in an aversive contextual discrimination task, likely through tonic firing in response to environmental cues. We observe sustained NE release in an aversive context during successful contextual disambiguation in a contextual fear discrimination task and are able to cause contextual disambiguation using evoked NE release. These results indicate that the LC-DG circuit is not only highly involved in differentiating between new and previous events, but also drives responses to contextual differences based on spatiotemporal dynamics of NE release.

Previous work has implicated prolonged phasic dopamine signals in striatum as important in signaling proximity and value of reward (Howe et al., 2013). In this study, it is postulated that ramping dopamine signals may provide a continuous estimate of

distance and size of reward and maintaining motivation towards that reward. Additionally, further work implicates burst stimulation of ventral tegmental area (VTA) neurons in causing a prolonged increase of dopamine in the nucleus accumbens and prefrontal cortex (Lohani et al., 2018). Here however, we demonstrate prolonged norepinephrine release in response to contextual discrimination, in which this NE ramping occurs in the time leading up to delivery of the foot shock in the CFD task, during which the animal must rely on contextual cues to disambiguate the unsafe and safe contexts. In addition, while the prolonged dopamine ramping occurred for up to 10 seconds, the NE ramping seen here lasted for 180 seconds, followed by delivery of the foot shock. This suggests a longer time scale function for NE release, especially during pattern separation, where continuous processing on contextual clues may be necessary for successful discrimination to occur. Further work must be done to better understand how these prolonged dynamics are involved in contextual learning, and whether these prolonged NE release dynamics are involved in specific phases of memory such as encoding, consolidation, or extinction. In addition, given that the hippocampus also receives strong dopaminergic inputs from the LC that are important in contextual learning, it is important to further study the specific methods by which dopamine and norepinephrine regulate contextual discrimination, and the roles of these neurotransmitters in DG function (Wagatsuma et al., 2018).

Additionally, during the modified CFD task used here wherein mice received one of the four different stimulation parameters, there appeared to be gradual decreases in NE release (quantified by AUC analysis) over the course of training in context B, where no stimulation occurred (**Fig. 5.2K, Fig. 5.3L, Fig. S5B, Fig. S5G**). This may be due to

the LC's role in novelty encoding as well as contextual learning (Hunsaker et al., 2008; Prince et al., 2016). We postulate that during this contextual fear discrimination task, and in the absence of an aversive stimuli, mice undergo increased NE release in both contexts during the initial stages of training, as they experience these novel contexts for the first time. However, as these mice become habituated to the contexts, this novelty encoding decreases, leading to decreased amounts of NE in the DG during the CFD task, which is then overcome in context A via increased evoked NE release due to photostimulation of LC-DG terminals.

Chapter 6. Conclusions and Future Directions

Since the classification of PTSD in the DSM in 1980, interest in the fundamental neurobiological mechanisms of this disorder has greatly increased. While the hippocampus and locus coeruleus (LC) noradrenergic systems have long been implicated in PTSD, PTSD-like symptoms, and fear learning and conditioning, the full role of these neural circuitry has remained incomplete. Researchers have extensively investigated these complex systems, to elucidate how these brain regions and neuromodulators interact in aversive contextual processing.

During my doctoral research, I focused on a specific projection from the LC to the dentate gyrus (DG), a subregion of the hippocampus. I illustrate the importance of these brain regions in aversive contextual processing and contextual fear discrimination, and how LC-modulation of the DG creates different behavioral outcomes. Additionally, I elucidate the spatiotemporal dynamics of NE release in the DG, and how distinct dynamics may play a role in contextual generalization or disambiguation.

In Chapter 1, I introduce and define PTSD, and summarize the history, diagnosis, symptoms, and current knowledge of this disorder. PTSD has emerged as a prevalent anxiety disorder, especially among returning veterans and those who have experienced sexual violence. It is characterized primarily by exposure to a traumatic event, followed by symptoms such as recurrent memories and flashbacks to the trauma, as well as physiological changes in response to the trauma including negative affect. Consequently, it has become increasingly researched, with areas such as the DG and LC implicated as having potential roles in fear conditioning.

The DG has long been implicated in functions such as learning and memory, as well as pattern separation and contextual disambiguation. It is the site of adult neurogenesis wherein new cells mature and grow even during adulthood. While the DG is composed of three layers, the granule cell layer, where adult neurogenesis primarily occurs, has been a particular area of interest in the context of pattern recognition and processing of episodic memories. There have been several theories proposed regarding the exact function of the DG and how it is involved in these processes, with most revolving around its sparse coding during episodic events, GC neurogenesis, as well as enhanced LTP in the hippocampus.

The locus coeruleus, or 'blue spot', supplies the mammalian brain with norepinephrine, a neurotransmitter that is implicated in the modulation of attention, arousal, and learning. While historically it has been viewed as a homogenous structure, more recent developments have begun to demonstrate the functional heterogeneity of this small brain region, with distinct populations of LC neurons responsible for influencing cognitive processes such as decision making, anxiety, and memory. Additionally, the LC supplies the hippocampus with dense noradrenergic and dopaminergic projections, and recent research has implicated these LC-hippocampal circuitry in contextual learning, suggesting a key role in development of PTSD and PTSD-like symptoms.

In Chapter 2, I introduce the contextual fear discrimination (CFD) paradigm used throughout this work. This paradigm involves 10 days of training, with repeated exposures to an unsafe context (context A), in which the animal receives a foot shock, and a safe context (context B), in which the animal does not receive a foot shock. These two contexts are similar, but distinct in several ways. In this CFD paradigm, elevated freezing levels by

the end of training in the unsafe context compared to the safe context signifies successful contextual disambiguation, wherein the animal recognizes that they are receiving the shock in one context, but not the other.

Additionally, I demonstrate functional connectivity between the LC-NE system and the DG, via several tracing experiments showing dense noradrenergic projections in the DG. Moreover, I demonstrate that bidirectional modulation of LC-NE projections to the DG results in opposing learning states in this CFD task. Through the use of optogenetics, which enables optical modulation of select neurons, I showed that excitation of the LC-DG circuit results in impairment of contextual discrimination, while inhibition of the LC-DG circuit results in facilitation of contextual discrimination. These results suggest that modulation of LC-DG noradrenergic circuitry impacts aversive contextual learning.

In Chapter 3, I introduce the use of *in vivo* 1-photon calcium imaging to record DG GCL ensembles during contextual fear conditioning. Through the use of 1-photon calcium imaging and the use of the Inscopix nVista miniscope, I demonstrate the ability to record distinct neuron activity in the DG during the CFD task. In animals that successfully undergo the CFD task and are able to disambiguate the safe and unsafe contexts, there is a distinct shift in DG ensemble recruitment, with more neurons responding selectively to context B, the safe context, compared to context A, the unsafe context. I hypothesize that as mice learn that context B is the safe context, there is an increased recruitment of DG GCs responding to that context and the new information regarding that context, over the course of training.

Meanwhile, I also demonstrate successful chemogenetic excitation of the LC-NE system through DREADDs, allowing me to mimic increased LC-NE activity. Doing so

results in impairment in performance in the CFD task, in a similar fashion to optogenetic excitation of LC-DG terminals. Additionally, during this impaired performance, mice that do not successfully discriminate between context A and B also do not undergo a shift in their DG neural ensembles. This signifies that performance in aversive contextual processing is linked to DG neural activity, and that shifts in ensemble activity may be necessary in the processing of new information when comparing these incoming cues to previous experiences.

In Chapter 4, I further explore the role of adrenergic receptors (ARs) on DG neurons in modulating aversive contextual processing. Through the use of chimeric opsin Opto-β_2, I was able to selectively mimic β-AR-like signaling in specific cell types in the DG GCL and hilus. Through *in situ* analysis, I determined that the primary cell types that may be responsible for modulating aversive contextual processing through adrenergic receptor signaling would be GABAergic interneurons in the hilus or glutamatergic neurons in the GCL of the DG.

While mimicking β-like signaling in DG glutamatergic neurons in the GCL did not result in any changes in performance in the CFD paradigm, there was an impairment of performance in the CFD paradigm in mice that underwent β-like signaling in DG hilar interneurons using Opto-β_2. In addition, applying β-AR agonist isoproterenol and β-AR antagonist propranolol onto DG GABAergic neurons in *ex vivo* slice electrophysiology yielded increases and decreases in action potentials, respectively. These findings suggest a key role for β-ARs on DG hilar interneurons in modulating aversive contextual processing, whereby increased NE release into DG and activation of DG hilar

interneurons results in inhibition of DG GCs during aversive contextual processing, causing contextual generalization.

In Chapter 5, I use *in vivo* fiber photometry in conjunction with novel biosensor $GRAB_{NE}$ to measure and further understand the temporal dynamics of NE release in the DG during aversive contextual processing. Through the use of $GRAB_{NE}$, which is able to detect real time changes in NE levels, I found that there was prolonged NE release in the DG in the unsafe context in the CFD task at the end of training, when mice were able to successfully discriminate between the two contexts.

From this, I sought to elucidate how temporal dynamics of NE release may be crucial in contextual discrimination and pattern separation. When mimicking endogenous prolonged tonic and phasic bursting NE release via LC-NE terminal stimulation in the DG, mice displayed increase freezing in the context they received photostimulation in, even in the absence of a salient aversive stimuli in that context. Furthermore, mimicking only the prolonged tonic firing was sufficient to cause this same effect while mimicking the phasic bursting associated with a foot shock was not, indicating that this prolonged NE release was sufficient to cause contextual disambiguation, and may play a fundamental role in contextual discrimination and pattern separation.

The work presented here supports the hypothesis that LC-NE hyperactivity in PTSD patients may modulate hippocampal function via specific adrenergic receptors on GABAergic interneurons in the DG hilus, and its association with contextual information processing potentially leading to context-related PTSD symptoms including hypervigilance. We also provide evidence that the DG GCL neural ensemble undergoes shifts in activity in conjunction with successful contextual learning. Additionally, we

demonstrate that prolonged NE release in the DG during aversive contextual processing plays a role in development of PTSD-like symptoms, and potential failures in contextual processing and pattern separation. Together, this work helps significantly advance our knowledge and understanding of LC-NE projections to the DG, the spatiotemporal dynamics of NE release in the DG, and the role of this circuit in aversive contextual processing, and development of PTSD.

From these findings, there are several future directions that remain unanswered which could help further our understanding of how the LC-NE system modulates DG pattern separation in aversive contextual processing. It should be noted that while we used β-like signaling to mimic endogenous β-signaling in the DG, we did not investigate whether this signaling was due to β_1- or β_2-adrenergic receptors in the DG. Furthermore, we also did not investigate the role of α-adrenergic receptors in the DG in pattern separation. It is possible that each of these receptors could play a vital role in NE binding in the DG during contextual disambiguation and aversive contextual processing. Future work into determining the exact role of these various adrenergic receptors could help improve our understanding of how the DG is involved in PTSD and identify potential targeted pharmacological treatments for those suffering from PTSD.

Additionally, this work does not explore the importance of other areas of the hippocampus, including the CA1 and CA3 regions, as well as the entorhinal cortex. Given the DG's connectivity with each of these other brain regions, it is reasonable to infer that these regions also play a key role in aversive contextual processing and fear learning, and other research in the field continues to explore the exact mechanisms by which the hippocampus modulates pattern separation. Further understanding of the trisynaptic loop

of the hippocampus, as well as the perforant pathway, may yield further insights into the exact role of the DG in aversive contextual processing.

Furthermore, this research does not delve into the roles that other brain regions may play in modulating aversive contextual processing. The LC supplies NE to many distinct brain regions, including the prefrontal cortex and amygdala, both of which have also been implicated in fear learning and extinction. The hippocampus also has strong connectivity with each of these brain regions, suggesting that they may each play a distinct role in modulation of aversive contextual processing. Further research must be conducted to elucidate the exact mechanisms by which the PFC, amygdala, and hippocampus interact to modulate pattern separation, fear conditioning, and aversive contextual processing.

Finally, the hippocampus also receives strong dopaminergic inputs from areas including the ventral tegmental area (VTA), and this dopaminergic circuitry has also been implicated in promoting attention, episodic memory formation, spatial learning, and synaptic plasticity. More research must be done on the specific interactions of NE and dopamine during aversive contextual processing, and whether the two control distinct mechanisms of contextual learning. This is especially relevant given that LC releases both dopamine and NE into the hippocampus. While the contents of this research do not cover the effects of dopamine on contextual fear learning, and PTSD, more work in this area would greatly benefit our knowledge regarding the role of distinct neurotransmitters in the development and symptoms of PTSD.

Overall, this work presents key findings regarding the role of LC-NE projections to the DG in modulating aversive contextual processing. I demonstrate bidirectional

modulation of LC-DG circuitry resulting in opposing learning states. Additionally, I show that successful fear discrimination is accompanied by a corresponding shift in the DG neural ensemble, while no such shift in the ensemble occurs during contextual generalization. Next, I uncover the role of β-adrenergic receptor signaling on DG hilar interneurons in contextual fear discrimination, while β-adrenergic receptor signaling on DG GCs does not appear to be involved. Finally, I implicate prolonged NE release in the DG during aversive contextual processing in contextual disambiguation, and that this elevated NE release is sufficient for discrimination even in the absence of an aversive stimuli. Altogether, the findings of this research provide a strong framework for continued understanding of the underlying neural mechanisms behind fear conditioning, aversive contextual learning, and PTSD.

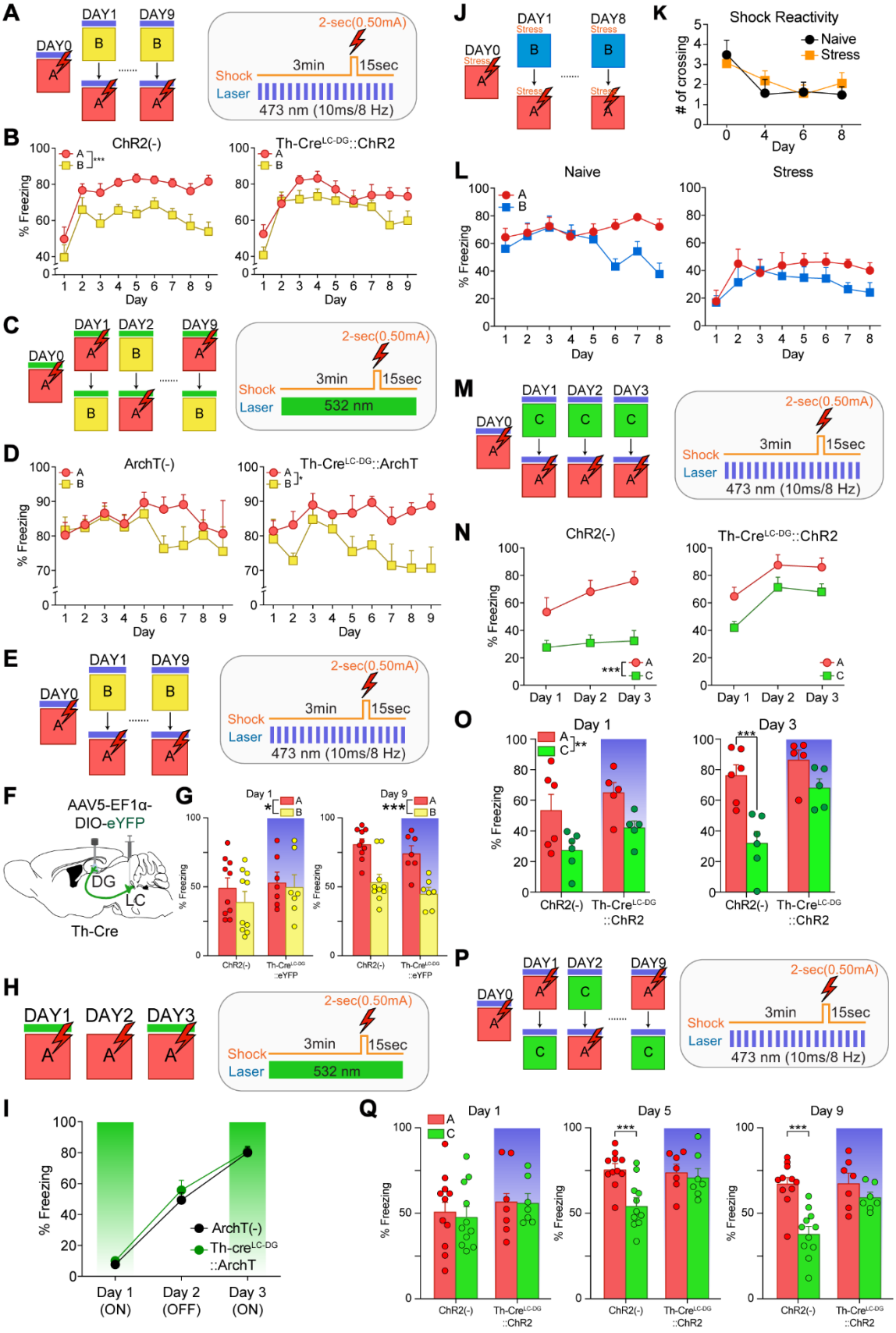
A
DAY0
DAY1
DAY9
B
2-sec(0.50mA)
Shock
3min
15sec
Laser
473 nm (10ms/8 Hz)
B
ChR2(-)
Th-Cre LC-DG ::ChR2
% Freezing
Day
C
DAY2
532 nm
D
ArchT(-)
Th-Cre LC-DG ::ArchT
E
F
AAV5-EF1α-
DIO-eYFP
DG
LC
Th-Cre
G
Day 1
Day 9
ChR2(-)
Th-Cre LC-DG ::eYFP
H
I
ArchT(-)
Th-cre LC-DG ::ArchT
Day 1 (ON)
Day 2 (OFF)
Day 3 (ON)
J
DAY8
Stress
K
Shock Reactivity
Naive
Stress
# of crossing
L
M
N
O
P
Q
Day 5

Figure S1. Monitoring of freezing behavior in CFD under different optogenetic and behavioral manipulations.
(**A**) Contextual fear discrimination (CFD) task with optogenetic activation of the LC-DG projection. Animals received a shock in context A (red), but not in context B (yellow) for nine days (left). Pattern of laser stimulation (both contexts) and electrical foot shock (only in context A) during a CFD session (right). (**B**) Analysis of progressive days of training in CFD. Acute activation of LC-DG projection impairs behavioral pattern separation in mice expressing ChR2 in LC-DG projections (**C**) CFD task with optogenetic inhibition of the LC-DG projection. Animals received a shock in context A (red), but not in context B (yellow) for nine days (left). Pattern of laser stimulation and electrical foot shock (only in context A) during a CFD session (right). (**D**) Analysis of progressive days of training in CFD. Acute inhibition of LC-DG projection resulted in enhancement of behavioral pattern separation in mice expressing ArchT in LC-DG projections (**E**) CFD task with optogenetic stimulation. Animals received a shock in context A (red), but not in context B (yellow) for nine days (left). Pattern of laser stimulation and shock (only in context A) during CFD (right). (**F**) Schematic of experimental approach depicts infection of LC-NE cells using Th-Cre mouse line with fluorescent reporter virus. (**G**) Mice expressing the reporter (Th-Cre^{LC-DG}::eYFP) were able to discriminate between the two contexts in a similar fashion to wild-type controls**.** Both groups received optogenetic light during trial, shaded bar denotes successful stimulation of opsin. (**H**) Th-Cre^{LC-DG}::ArchT mice were subjected to one-shock contextual fear conditioning before contextual fear discrimination task (right). Pattern of laser stimulation and electrical foot shock during a CFD session (right). (**I**) Th-cre^{LC-DG}::ArchT mice (n = 7) did not differ from ArchT(-) controls (n = 8) even with LC-DG optogenetic inhibition during both the acquisition and retrieval stage. Both groups received optogenetic light during trial, shaded bar denotes successful stimulation of opsin. (**J**) CFD task with restraint stress administration replacing optogenetic activation. (**K**) Restraint stress did not affect shock reactivity (indirect measure of pain sensitivity). (**L**) Acute restraint stress impairs performance in CFD (n = 7), while naïve animals successfully discriminated between the two contexts (n = 7). (**M**) Contextual fear discrimination (CFD) task with optogenetic activation of the LC-DG projection, with a dissimilar context C (green) replacing context B. Animals received a shock in context A (red), but not in context C, for three days (left). Pattern of laser stimulation (both contexts) and electrical foot shock (only in context A) during a CFD session (right). (**N**) Acute activation of LC-DG projection still impairs behavioral pattern separation in mice expressing ChR2 but not in wild-type controls. (**O**) Although both groups successfully discriminated on the first day of training, Th-Cre^{LC-DG}::ChR2 mice failed to discriminate between contexts in later training sessions**.** Both groups received optogenetic light during trial, shaded bar denotes successful stimulation of opsin. (**P**) Contextual fear discrimination (CFD) task with optogenetic activation of the LC-DG projection, with a dissimilar context C (green) replacing context B, and alternating order of presentation of contexts during training. Animals received a shock in context A (red), but not in context C, for nine days (left). Pattern of laser stimulation (both contexts) and electrical foot shock (only in context A) during a CFD session (right). (**Q**) Acute activation of LC-DG projection impairs behavior in mice expressing ChR2 (n = 7) but not in wild-type controls (n = 11). Both groups received optogenetic light during trial, shaded bar denotes successful stimulation of opsin. All data are mean ± SEM. *$p < 0.05$, **$p < 0.01$, ***$p < 0.005$.

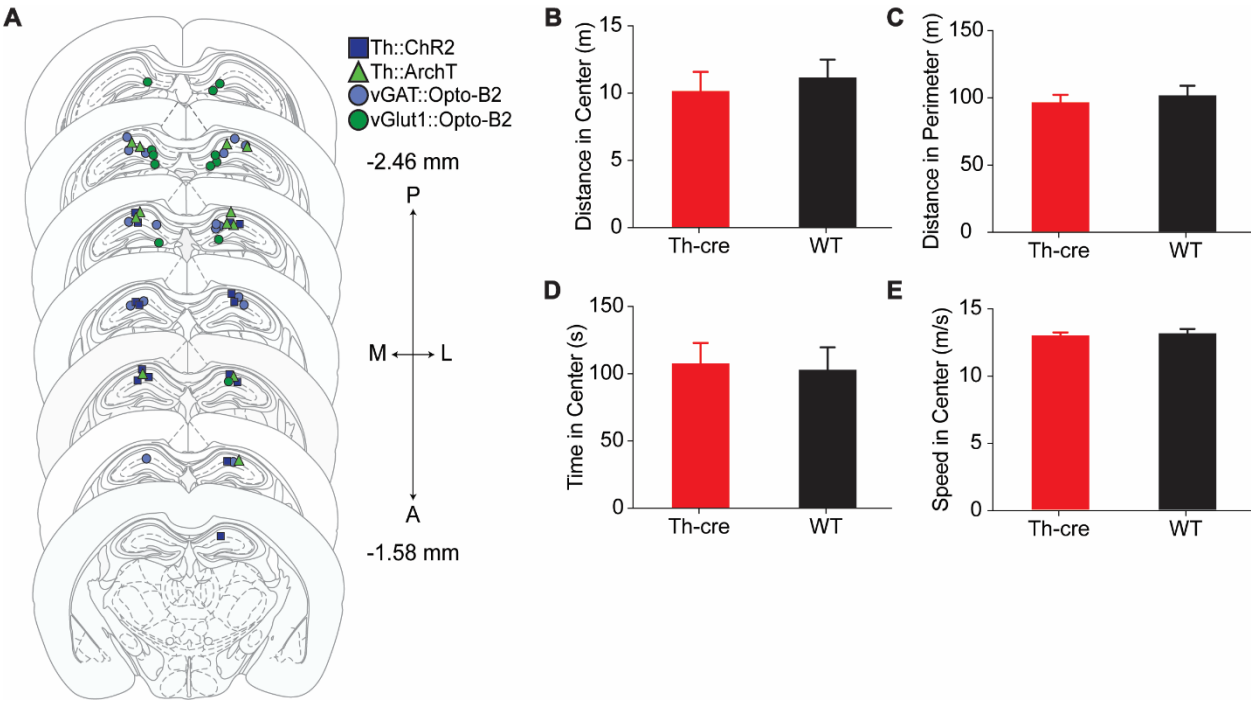

Figure S2. Validation of injection and implant sites and unmodulated behavior.
(**A**) Reconstruction of approximate locations of fiber-optic implant tips for Th-Cre$^{LC\text{-}DG}$::ChR2, Th-Cre$^{LC\text{-}DG}$::ArchT. vGlut1-Cre^{DG}::Opto-β_2 mice and vGAT-Cre^{DG}::Opto-β_2 mice. (**B**) Distance traveled in center of open field assay by Th-Cre and wild-type control animals without any circuit manipulations ($t_{(18)}$ = -0.5002; p = 0.6230). (**C**) Distance traveled in perimeter of open field assay by Th-Cre and wild-type control animals without any circuit manipulations ($t_{(18)}$ = -0.6720; p = 0.5101). (**D**) Time spent in center of open field assay by Th-Cre and wild-type controls without any circuit manipulations ($t_{(18)}$ = 0.2176; p = 0.8301). (**E**) Speed in center of open field assay by Th-Cre and wild-type control animals without any circuit manipulations ($t_{(18)}$ = -1.3705; p = 0.1874). No significant differences in terms of motor control and behavior were detected between Th-Cre (n = 11) and wild-type controls (*n* = 9). All data are mean ± SEM. *ns.*

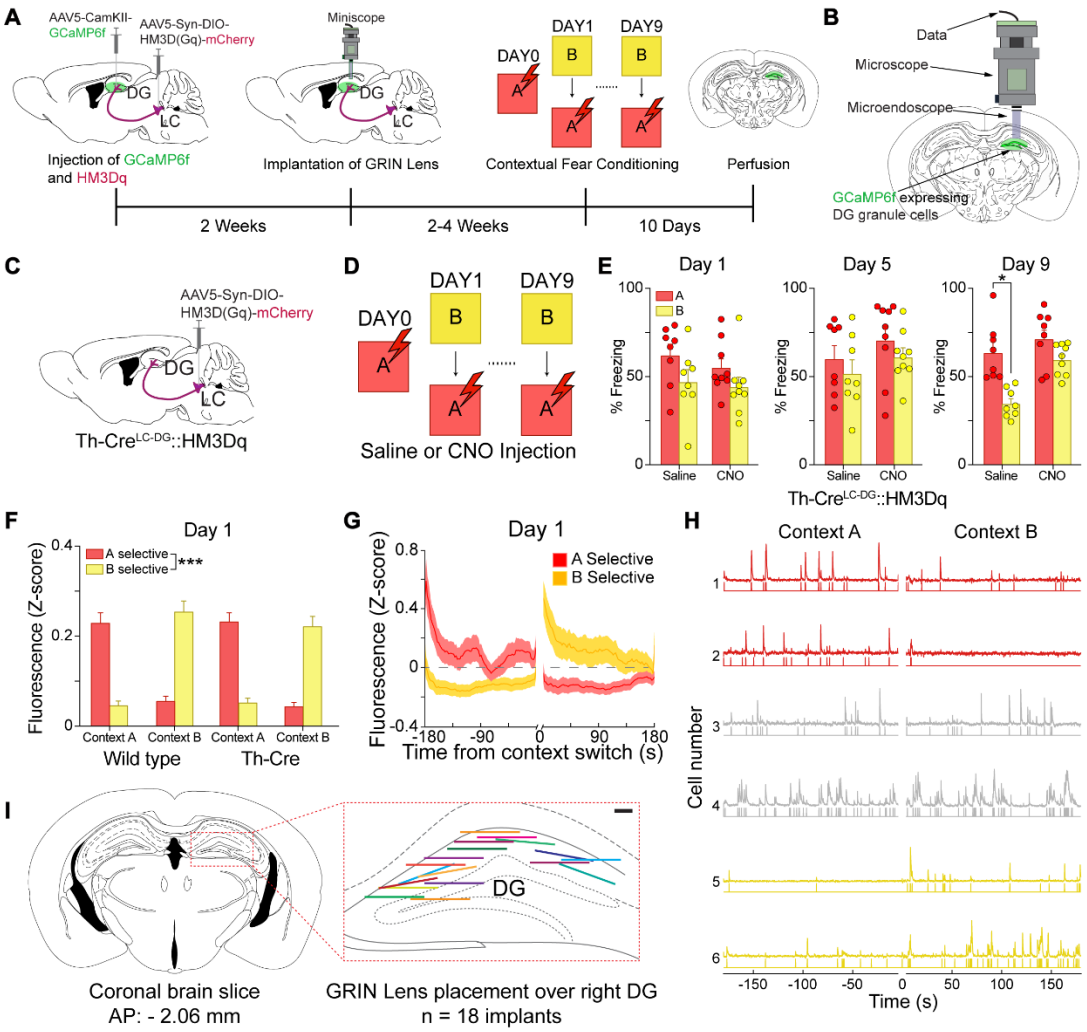

Fig. S3. Timeline of imaging technique and supplementary imaging analysis.
(**A**) Schematic depicting procedural timeline for *in vivo* imaging of DG neuronal ensemble in contextual fear conditioning (CFD). Th-Cre mice and wild-type controls were injected with HM3Dq in LC to enable increased modulation of LC-NE cells chemogenetically (Th-Cre^{LC-DG}::HM3Dq), and Ca^{2+} indicator (GCaMP6f) in the DG to enable imaging of the neural ensemble. Microendoscopic GRIN lenses were implanted above the DG in the same mice 2 weeks post-injection. 2 weeks post-implant, mice were trained in CFD. Following 10 days of training, mice were sacrificed for immunohistochemistry. (**B**) Schematic depicts placement of GCaMP6f injection and GRIN lens implant, as well as mini-microscope used during imaging. (**C**) Schematic of experimental approach depicts infection of LC-NE cells using Th-Cre mouse line with HM3Dq. (D) CFD with saline or CNO injection in Th-Cre^{LC-DG}::HM3Dq mice 30 minutes prior to task. (**F**E Th-Cre^{LC-DG}::HM3Dq mice injected with saline (n = 8) prior to CFD task are able to discriminate between the two contexts on day 9 of training, while Th-Cre^{LC-DG}::HM3Dq mice injected with CNO (n = 9) prior to CFD task are not. (**F**) Average response amplitude of neurons responding selectively to context A or context B in both wild-type controls and Th-Cre^{LC-DG}::HM3Dq mice, at the beginning and end of training. (**G**) Averaged cell activity traces for cells imaged from Th-Cre^{LC-DG}::HM3Dq mice during day 1 of CFD task for neurons responding selectively to context A or context B. (**H**) Representative neurons responding selectively to context A (unsafe, top), context B (safe, bottom), or responding nonselectively (middle). For each neuron the binarized calcium event trace is plotted below, and the raw calcium trace is plotted above (Context Selectivity: $F_{(3,1126)} = 73.6$, $p < 0.0001$; Group: $F_{(1,1126)} = 0.513$, $p = 0.474$; Group x Selectivity: $F_{(3,1126)} = 0.452$, $p = 0.716$). (**I**) Reconstruction of approximate locations of GRIN lens implants in both wild-type controls and Th-Cre^{LC-DG}::HM3Dq mice Scale bar = 300 µm. All data are mean ± SEM. *$p < 0.05$, ***$p < 0.005$.

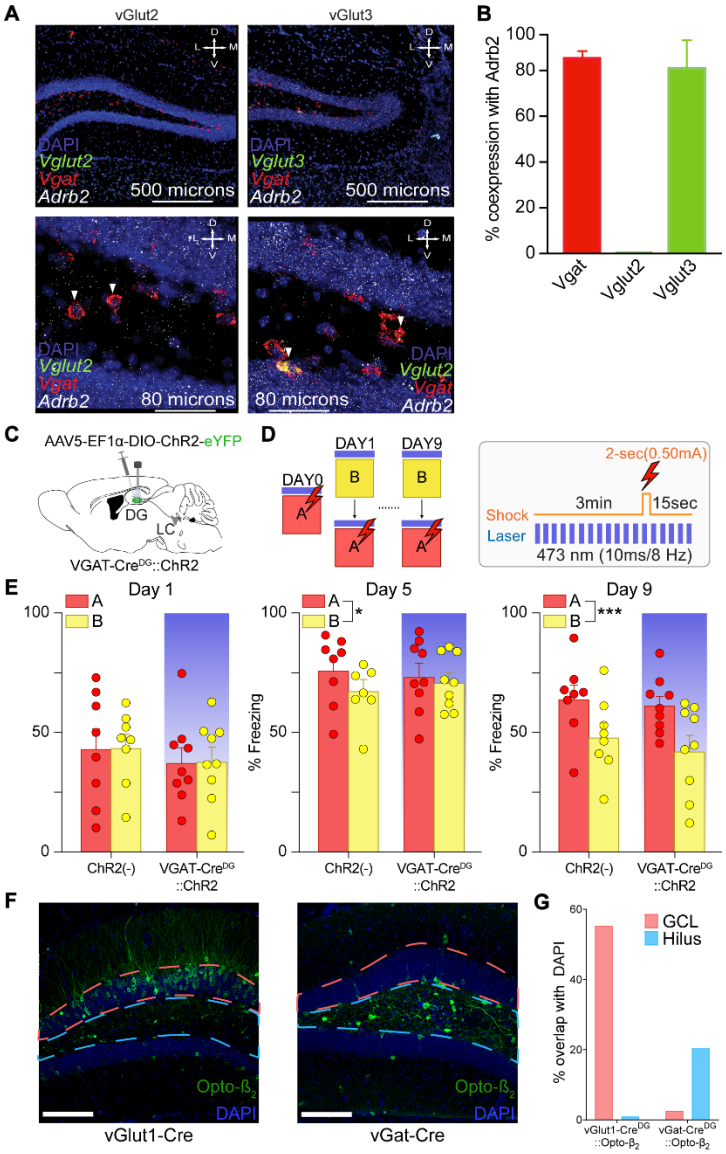

Figure S4. In situ hybridization and control experiment proving specific effect of Opto-β$_2$ in CFD and quantification of Opto-β$_2$ transfection.

(**A**) *In-situ* hybridization depicting coronal images of colocalization of the following: Left column: DAPI (blue), *Adrb2* (white), *Vgat* (red), *Vglut2* (green) within the dentate gyrus of wild-type mice; Right column: DAPI (blue), *Adrb2* (white), *Vgat* (red), *Vglut3* (green) within the dentate gyrus of wild-type mice. (**B**) Quantification of colocalization percentage of *Vgat*, *Vglut2*, and *Vglut3* with *Adrb2* showed high colocalization of *Adrb2* with *Vgat*, and *Vglut3*, but not *Vglut2.* (**C**) Schematic of experimental approach depicts infection of DG interneurons using vGAT-Cre mouse line with channelrhodopsin (vGAT-Cre^{DG}::ChR2). (**D**) Contextual fear discrimination (CFD) task with optogenetic activation of the DG interneurons. Animals received a shock in context A (red), but not in context B, for nine days (left). Pattern of laser stimulation (both contexts) and electrical foot shock (only in context A) during a CFD session (right). (**E**) Mice expressing channelrhodopsin (vGAT-Cre^{DG}::ChR2, n = 9) were able to discriminate between the two contexts in a similar fashion to wild-type controls (n = 8). Both groups received optogenetic light during trial, shaded bar denotes successful stimulation of opsin. (**F**) Representative image depicting expression of Opto-β$_2$ in DG hilus and GCL in vGlut1-Cre mice and vGAT-Cre mice. Scale bar = 100 μm. (**G**) Quantification of overlap between DAPI and Opto-β$_2$ shows higher infection of GCL in vGlut1-Cre mice, and higher infection of hilus in vGAT-Cre mice. Representative from 17 mice in two cohorts. All data are mean ± SEM. *p < 0.05, ***p < 0.005.

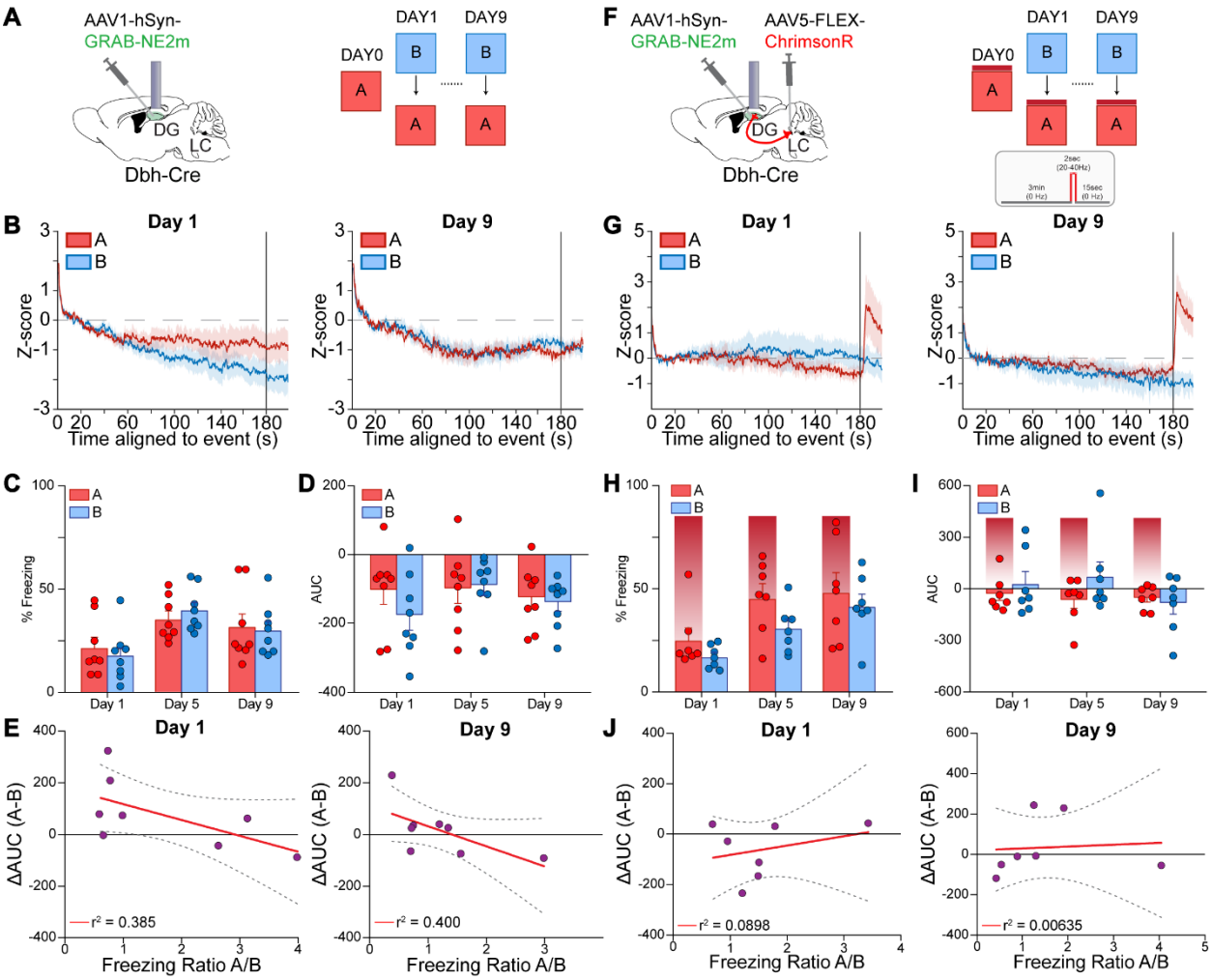

Figure S5. Contextual fear discrimination task while recording NE release in DG.
(**A**) Schematic of experimental approach depicts infection of dentate gyrus with GRAB$_{NE}$, and optic fiber implanted above the DG and contextual fear discrimination (CFD) task. (**B**) Average traces of GRAB$_{NE}$ fluorescence in context A (red) and context B (blue) for day 1 (left), and day 9 (right). (**C**) Mice were unable to discriminate between context A and B in early, middle, and late stages of training. (**D**) Area under the curve analysis of GRAB$_{NE}$ fluorescence levels in context A and context B on the first, fifth, and ninth days of training (**E**) Linear regression using Pearson correlation for ratio of freezing behavior between context A and context B vs. difference in AUC between context A and context B. (**F**) Schematic of experimental approach depicts infection of dentate gyrus with GRAB$_{NE}$, optic fiber implanted above the DG, and infection of locus coeruleus with ChrimsonR, and contextual fear discrimination (CFD) task. (**G**) Average traces of GRAB$_{NE}$ fluorescence in context A (red) and context B (blue) for day 1 (left), and day 9 (right). (**H**) Mice were unable to discriminate between context A and B in early, middle, and late stages of training. (**I**) Area under the curve analysis of GRAB$_{NE}$ fluorescence levels in context A and context B on the first, fifth, and ninth days of training (**J**) Linear regression using Pearson correlation for ratio of freezing behavior between context A and context B vs. difference in AUC between context A and context B. All data are mean ± SEM. *n.s.*

Table S1. Statistical analysis.

TABLE S1

Figure		Experimental Variables	Statistical Test	Results	Results (post-hoc)
2.2	C	Optogenetic Stimulation (ChR2)	REML	Day 1: Group: $F_{(1,18)} = 0.055$, p = 0.818; Context: $F_{(1,18)} = 16.885$, p < 0.001; Days × Context: $F_{(1,18)} = 6.076$, p = 0.786	N/A
				Day 5: Group: $F_{(1,18)} = 0.012$, p = 0.913; Context: $F_{(1,18)} = 30.608$, p < 0.001; Days × Context: $F_{(1,18)} = 8.034$, p = 0.011	ChR2(-), A vs B, p < 0.001; Context A, ChR2(-) vs. Th-Cre$^{LC\text{-}DG}$::ChR2, p = 0.709
				Day 9: Group: $F_{(1,18)} = 0.040$, p = 0.843; Context: $F_{(1,18)} = 36.016$, p < 0.001; Group × Context: $F_{(1,18)} = 4.463$, p = 0.049	ChR2(-), A vs B, p < 0.001; Context A, ChR2(-) vs. Th-Cre$^{LC\text{-}DG}$::ChR2, p = 0.608
	F	Optogenetic Stimulation (ArchT)	REML	Day 1: Group: $F_{(1,13)} = 0.025$, p = 0.878; Context: $F_{(1,13)} = 0.014$, p = 0.907; Group × Context: $F_{(1,13)} = 0.256$, p = 0.621	N/A
				Day 5: Group: $F_{(1,13)} = 2.464$, p = 0.141; Context: $F_{(1,13)} = 4.804$, p = 0.047; Group × Context: $F_{(1,13)} = 1.435$, p = 0.252	N/A
				Day 9: Group: $F_{(1,13)} = 0.027$, p = 0.871; Context: $F_{(1,13)} = 17.03$, p = 0.001; Group × Context: $F_{(1,13)} = 5.39$, p = 0.037	Th-Cre$^{LC\text{-}DG}$::ArchT, A vs B, p < 0.005
	I	Stress/Naive	REML	Day 3: Group: $F_{(1,14)} = 6.137$, p = 0.033	N/A
				Day 6: Group: $F_{(1,9.46)} = 4.044$, p = 0.073; Context: $F_{(1,13.8)} = 21.429$, p < 0.001; Days × Context: $F_{(1,13.8)} = 3.824$, p = 0.071	N/A
				Day 8: Group: $F_{(1,10.39)} = 7.109$, p = 0.023; Context: $F_{(1,14.87)} = 24.6072$, p < 0.001; Days × Context: $F_{(1,14.87)} = 3.322$, p = 0.085	N/A
3.2	I	Context Selectivity	Chi-squared	Context A: Chi-square = 0.166, Bonferonni adj. p-value (p < 0.008) = 0.682	N/A
				Context B: Chi-square = 27.3, Bonferonni adj. p-value (p < 0.008) < 0.001	N/A
				Nonselective: Chi-square = 18.1575, Bonferonni adj. p-value (p < 0.008) < 0.001	N/A
			Unpaired t-test	Context A: $t_{(18)} = 0.398$, p = 0.697	N/A
				Context B: $t_{(18)} = 2.01$, p = 0.0618	N/A
	J	Cell Response-Freezing Response Correlation	Pearson correlation	Day 1: r = -0.132, r^2 = 0.0173, p = 0.737	N/A
				Day 9: r = 0.749, r^2 = 0.561, p = 0.0202	N/A
	M	Context Selectivity	Chi-squared	Context A: Chi-square = 0, Bonferonni adj. p-value (p < 0.008) = 1	N/A
				Context B: Chi-square = 13.9, Bonferonni adj. p-value (p < 0.008) < 0.001	N/A
				Nonselective: Chi-square = 7.54, Bonferonni adj. p-value (p < 0.008) = 0.006	N/A
3.3	D	Treatment (CNQ)	REML	Day 1: Group: $F_{(1,18)} = 2.15$, p = 0.162; Context: $F_{(1,18)} = 0.0566$, p = 0.815; Group × Context: $F_{(1,18)} = 5.20$, p = 0.0366	HMSDq(-), A vs B, p = 0.308; Th-Cre$^{LC\text{-}DG}$::HMSDq, A vs B, p = 0.179
				Day 5: Group: $F_{(1,18)} = 0.207$, p = 0.655; Context: $F_{(1,18)} = 5.06$, p = 0.0389; Group × Context: $F_{(1,18)} = 0.0392$, p = 0.846	N/A
				Day 9: Group: $F_{(1,18)} = 3.46$, p = 0.0811; Context: $F_{(1,18)} = 23.82$, p = 0.0002; Group × Context: $F_{(1,18)} = 4.497$, p = 0.0499	HMSDq(-), A vs B, p < 0.001
	H	Context Selectivity	Chi-squared	Context A: Chi-square = 2.35, Bonferonni adj. p-value (p < 0.008) = 0.125	N/A
				Context B: Chi-square = 6.18, Bonferonni adj. p-value (p < 0.008) = 0.0131	N/A
				Nonselective: Chi-square = 0.883, Bonferonni adj. p-value (p < 0.008) = 0.006	N/A
			Unpaired t-test	Context A: $t_{(18)} = 0.747$, p = 0.469	N/A
				Context B: $t_{(18)} = 1.37$, p = 0.191	N/A
	I	Cell Response-Freezing Response Correlation	Pearson correlation	Day 1: r = 0.375, r^2 = 0.141, p = 0.32	N/A
				Day 9: r = -0.109, r^2 = 0.0001, p = 0.98	N/A
	L	Context Selectivity	Chi-squared	Context A: Chi-square = 8.52, Bonferonni adj. p-value (p < 0.008) = 0.003	N/A
				Context B: Chi-square = 6.98, Bonferonni adj. p-value (p < 0.008) = 0.0082	N/A
				Nonselective: Chi-square = 0.307, Bonferonni adj. p-value (p < 0.008) = 0.580	N/A
	M	Context Selectivity	Kolmogorov-Smirnov test	HMSDq(-): K-stat = 0.771, p < 0.001	N/A
				Th-Cre$^{LC\text{-}DG}$::HMSDq: K-stat = 0.6724, p = 0.0533	N/A
4.1	D	Treatment (Propranolol)	REML	Day 1: Group: $F_{(1,12)} = 0.665$, p = 0.431; Context: $F_{(1,12)} = 0.361$, p = 0.559; Group × Context: $F(_{(1,12)} = 3.29$, p = 0.0947	N/A
				Day 5: Group: $F_{(1,12)} = 1.31$, p = 0.274; Context: $F_{(1,12)} = 1.15$, p = 0.305; Group × Context: $F_{(1,12)} = 1.39$, p = 0.261	N/A
				Day 9: Group: $F_{(1,12)} = 0.109$, p = 0.747; Context: $F_{(1,12)} = 6.34$, p = 0.0271; Group × Context: $F_{(1,12)} = 4.78$, p = 0.0494	Propranolol, A vs B, p = 0.0121
4.2	G	Optogenetic Stimulation (Opto-β2)	REML	Day 1: Group: $F_{(1,13)} = 0.0468$, p = 0.832; Context: $F_{(1,13)} = 1.49$, p = 0.246; Group × Context: $F_{(1,13)} = 0.398$, p = 0.540	N/A
				Day 5: Group: $F_{(1,13)} = 0.0913$, p = 0.768; Context: $F_{(1,13)} = 5.20$, p = 0.0417; Group × Context: $F_{(1,13)} = 0.0151$, p = 0.904	N/A
				Day 9: Group: $F_{(1,13)} = 0.101$, p = 0.757; Context: $F_{(1,13)} = 18.14$, p = 0.0017; Group × Context: $F_{(1,13)} = 0.310$, p = 0.588	N/A
	J	Optogenetic Stimulation (Opto-β2)	REML	Day 1: Group: $F_{(1,17)} = 0.862$, p = 0.366; Context: $F_{(1,17)} = 0.352$, p = 0.561; Group × Context: $F_{(1,17)} = 7.167$, p = 0.016	Opto-β2(-), A vs B, p = 0.275; vGAT-Cre^{DG}::Opto-β2, A vs B, p = 0.074; Context A, Opto-β2(-) vs. vGAT1-Cre^{DG}::Opto-β2, p = 0.270
				Day 5: Group: $F_{(1,17)} = 0.196$, p = 0.664; Context: $F_{(1,17)} = 2.175$, p = 0.159; Group × Context: $F_{(1,17)} = 3.281$, p = 0.088	Context A, Opto-β2(-) vs. vGAT1-Cre^{DG}::Opto-β2, p = 0.996
				Day 9: Group: $F_{(1,17)} = 0.407$, p = 0.532; Context: $F_{(1,17)} = 44.286$, p < 0.001; Group × Context: $F_{(1,17)} = 12.026$, p = 0.003	Opto-β2(-), A vs B, p < 0.001; Context A, Opto-β2(-) vs. vGlut1-Cre^{DG}::Opto-β2, p = 0.257
4.3	A	Action Potentials	REML	Depolarization Step: $F_{(15,285)} = 9.303$, p<0.0001; Drug: $F_{(2,285)} = 59.84$, p<0.0001; Depolarization Step x Drug: $F_{(30,285)} = 2.207$, p = 0.0005	Veh vs Prop: p<0.0001; Veh vs Iso: p<0.0001; Prop vs Iso: p<0.0001
	B			Statistics derived from Two-way ANOVA of the data specified in Figure 4I. Veh vs Prop: p=0.1411. Veh vs Iso: p=0.0185. Prop vs Iso: p=0.0005.	N/A
	C			Statistics derived from Two-way ANOVA of the data specified in Figure 4I. Veh vs Prop: p=0.0007. Veh vs Iso: p=0.2732. Prop vs Iso: p<0.0001	N/A
5.1	E	Behavior (Tail lift)	Unpaired t-test	GRAB-NE vs YFP: $t_{(13)} = 4.35$; p = 0.0008	N/A
	G	Behavior (Foot shock)	Unpaired t-test	GRAB-NE vs YFP: $t_{(12)} = 3.502$; p = 0.0044	N/A
	I	Optogenetic stimulation (ChrimsonR)	Unpaired t-test	GRAB-NE vs YFP: $t_{(13)} = 3.859$; p = 0.002	N/A
	L	Optogenetic stimulation (ChrimsonR)	Tukey's multiple comparisons	1 Hz vs. 3 Hz: p = 0.7718	N/A
				1 Hz vs. 5 Hz: p = 0.0007	N/A
				1 Hz vs. 10 Hz: p < 0.0001	N/A
				1 Hz vs. 20 Hz: p < 0.0001	N/A
				3 Hz vs. 5 Hz: p = 0.0177	N/A
				3 Hz vs. 10 Hz: p < 0.0001	N/A
				3 Hz vs. 20 Hz: p < 0.0001	N/A
				5 Hz vs. 10 Hz: p = 0.0496	N/A
				5 Hz vs. 20 Hz: p < 0.0001	N/A
				10 Hz vs. 20 Hz: p = 0.0005	N/A
5.2	E	Behavior (CFD)	Paired t-test	Day 1: $t_{(9)} = 2.045$, p = 0.0709	N/A
				Day 5: $t_{(9)} = 4.137$, p = 0.0025	N/A
				Day 9: $t_{(9)} = 2.660$, p = 0.0261	N/A
	F	Area Under Curve	Paired t-test	Day 1: $t_{(9)} = 0.519$, p = 0.6163	N/A
				Day 5: $t_{(9)} = 3.355$, p = 0.0085	N/A
				Day 9: $t_{(9)} = 3.774$, p = 0.0044	N/A
	G	Freezing Response-ΔAUC Correlation	Pearson correlation	Day 1: r = -0.4196, r^2 = 0.176, p = 0.2274	N/A
				Day 9: r = 0.7164, r^2 = 0.5133, p = 0.0198	N/A
5.3	E	Behavior (CFD)	Paired t-test	Day 1: $t_{(7)} = 0.4134$, p = 0.6917	N/A
				Day 5: $t_{(7)} = 1.966$, p = 0.0859	N/A
				Day 9: $t_{(7)} = 4.184$, p = 0.0041	N/A
	F	Area Under Curve	Paired t-test	Day 1: $t_{(7)} = 3.111$, p = 0.0170	N/A
				Day 5: $t_{(7)} = 3.033$, p = 0.0190	N/A
				Day 9: $t_{(7)} = 4.025$, p = 0.005	N/A
	G	Freezing Response-ΔAUC Correlation	Pearson correlation	Day 1: r = -0.5167, r^2 = 0.2701, p = 0.1868	N/A
				Day 9: r = 0.8182, r^2 = 0.6545, p = 0.0137	N/A
5.4	E	Behavior (CFD)	Paired t-test	Day 1: $t_{(7)} = 0.9953$, p = 0.3466	N/A
				Day 5: $t_{(7)} = 2.672$, p = 0.0732	N/A
				Day 9: $t_{(7)} = 2.735$, p = 0.0257	N/A
	F	Area Under Curve	Paired t-test	Day 1: $t_{(7)} = 1.335$, p = 0.2187	N/A
				Day 5: $t_{(7)} = 5.359$, p = 0.0007	N/A
				Day 9: $t_{(7)} = 3.611$, p = 0.0069	N/A
	G	Freezing Response-ΔAUC Correlation	Pearson correlation	Day 1: r = -0.4744, r^2 = 0.2250, p = 0.1970	N/A
				Day 9: r = 0.8344, r^2 = 0.6963, p = 0.0052	N/A
S1	B	Optogenetic Stimulation (ChR2)	REML	ChR2(-): Context: $F_{(1,14)} = 2.685$, p = 0.119; Days: $F_{(1,1446)} = 14.568$, p < 0.001; Days × Context: $F_{(8,1446)} = 1.386$, p = 0.206	N/A
				Th-Cre$^{LC\text{-}DG}$::ChR2: Context: $F_{(1,135)} = 19.430$, p < 0.001; Days: $F_{(13,1446)} = 19.942$, p < 0.001; Days × Context: $F_{(8,1446)} = 0.892$, p = 0.525	N/A
	D	Optogenetic Stimulation (ArchT)	REML	ArchT (-): Context: $F_{(1,14)} = 0.681$, p = 0.423; Days: $F_{(8,112)} = 1.885$, p < 0.073; Days × Context: $F_{(8,112)} = 1.251$, p = 0.278	N/A
				Th-Cre$^{LC\text{-}DG}$::ArchT: Context: $F_{(1,17)} = 5.743$, p = 0.034; Days: $F_{(8,96)} = 2.470$, p = 0.018; Days × Context: $F_{(8,96)} = 2.065$, p = 0.045	N/A
	G	Transgenic Background (Th-Cre)	REML	Day 1: Group: $F_{(1,15)} = 0.533$, p = 0.477; Context: $F_{(1,15)} = 5.75$, p = 0.0299 ; Group × Context: $F_{(1,15)} = 1.34$, p = 0.266	N/A
				Day 9: Group: $F_{(1,15)} = 2.28$, p = 0.154; Context: $F_{(1,15)} = 44.94$, p < 0.0001 ; Group × Context: $F_{(1,15)} = 0.0292$, p = 0.867	N/A
	I	Optogenetic Stimulation (ArchT)	Paired t-test	$t_{(14)} = 2.075$; p = 0.1737	N/A
	K	Stress/Naive	REML	Group × Days: $F_{(9,135)} = 1.264$, p = 0.317	N/A
	L	Stress/Naive	REML	Naïve: Context: $F_{(1,7.86)} = 2.790$, p = 0.134; Days: $F_{(7,87.89)} = 2.712$, p = 0.014; Days × Context: $F_{(7,87.89)} = 4.445$, p < 0.001	N/A
				Stress: Context: $F_{(1,12)} = 1.823$, p = 0.201; Days: $F_{(13,84)} = 3.165$, p = 0.005; Days × Context: $F_{(13,84)} = 0.640$, p = 0.721	N/A
	N	Optogenetic Stimulation (ChR2)	REML	ChR2(-): Context: $F_{(1,2)} = 68.1$, p < 0.001; Days: $F_{(2,10)} = 3.071$, p < 0.091; Days × Context: $F_{(2,10)} = 2.433$, p = 0.137	N/A
				Th-Cre$^{LC\text{-}DG}$::ChR2: Context: $F_{(1,4)} = 3.32$, p = 0.142; Days: $F_{(2,8)} = 75.58$, p < 0.001; Days × Context: $F_{(2,8)} = 0.905$, p = 0.442	N/A
	O	Optogenetic Stimulation (ChR2)	REML	Day 1: Group: $F_{(1,3)} = 2.661$, p = 0.137; Context: $F_{(1,3)} = 12.79$, p = 0.006 ; Group × Context: $F_{(1,3)} = 0.055$, p = 0.82	N/A
				Day 3: Group: $F_{(1,3)} = 6.645$, p = 0.0298; Context: $F_{(1,3)} = 48.84$, p < 0.0001 ; Group × Context: $F_{(1,3)} = 8.569$, p = 0.017	ChR2(-), A vs C, p < 0.001
	Q	Optogenetic Stimulation (ChR2)	REML	Day 1: Group: $F_{(1,14)} = 0.611$, p = 0.446; Context: $F_{(1,14)} = 0.363$, p = 0.555; Group × Context: $F_{(1,14)} = 0.114$, p = 0.740	N/A
				Day 5: Group: $F_{(1,14)} = 2.51$, p = 0.132; Context: $F_{(1,14)} = 9.80$, p = 0.0065; Group × Context: $F_{(1,14)} = 5.62$, p = 0.0307	ChR2(-), A vs C, p < 0.001
				Day 9: Group: $F_{(1,14)} = 6.43$, p = 0.0221; Context: $F_{(1,14)} = 18.1$, p = 0.0006; Group × Context: $F_{(1,14)} = 4.97$, p = 0.0406	ChR2(-), A vs C, p < 0.001
S2	B	Th-cre/WT	Paired t-test	$t_{(10)} = -0.5002$; p = 0.6230	N/A
	C	Th-cre/WT	Paired t-test	$t_{(10)} = -0.6720$; p = 0.5101	N/A
	D	Th-cre/WT	Paired t-test	$t_{(10)} = 0.2176$; p = 0.8301	N/A
	E	Th-cre/WT	Paired t-test	$t_{(10)} = -1.3705$; p = 0.1874	N/A
S3	F	Transgenic Background (Th-Cre)	REML	Day 1: Group: $F_{(1,13)} = 0.390$, p = 0.541; Context: $F_{(1,13)} = 0.21.34$, p = 0.0003; Group × Context: $F_{(1,13)} = 0.553$, p = 0.469	N/A
				Day 5: Group: $F_{(1,13)} = 1.44$, p = 0.249; Context: $F_{(1,13)} = 4.47$, p = 0.052; Group × Context: $F_{(1,13)} = 0.0181$, p = 0.895	N/A
				Day 9: Group: $F_{(1,13)} = 12.49$, p = 0.003; Context: $F_{(1,13)} = 25.57$, p = 0.0001; Group × Context: $F_{(1,13)} = 4.68$, p = 0.0471	Saline Treatment, A vs B, p < 0.001
	H	Cell Selective Activity	REML	Context Selectivity: $F_{(3,1128)} = 73.6$, p < 0.0001; Group: $F_{(1,1128)} = 0.513$, p = 0.474; Group x Selectivity: $F_{(3,1128)} = 0.452$, p = 0.716	N/A
S4	E	Optogenetic Stimulation (ChR2)	REML	Day 1: Group: $F_{(1,15)} = 0.467$, p = 0.505; Context: $F_{(1,15)} = 0.0248$, p = 0.877; Group × Context: $F_{(1,15)} = 3.72e\text{-}5$, p = 0.995	N/A
				Day 5: Group: $F_{(1,15)} = 0.0017$, p = 0.968; Context: $F_{(1,15)} = 5.77$, p = 0.0297; Group × Context: $F_{(1,15)} = 1.648$, p = 0.219	N/A
				Day 9: Group: $F_{(1,15)} = 0.438$, p = 0.518; Context: $F_{(1,15)} = 18.2$, p = 0.0007; Group × Context: $F_{(1,15)} = 0.117$, p = 0.737	N/A

Table S2							
Mouse	**Day 1 Total**	**Day 1 A Selective**	**Day 1 B Selective**	**Day 9 Total**	**Day 9 A Selective**	**Day 9 B Selective**	**Matched Cells**
Th-cre 2-1	43	5	15	50	7	19	9
Th-cre 2-2	105	50	13	137	37	15	80
Th-cre 2-3	78	29	17	98	24	35	58
Th-cre 348-1	32	15	1	25	8	9	5
Th-cre 349-2	355	90	85	221	59	68	28
Th-cre 386-2	45	8	12	10	0	3	0
Th-cre 387-4	31	5	12	31	5	21	8
Th-cre 396-1	37	5	8	38	10	6	26
Th-cre 396-3	63	1	14	67	5	14	21
WT 122-1	16	6	3	32	20	6	9
WT 122-2	36	10	5	43	6	9	19
WT 122-3	43	14	12	60	6	30	18
WT 124-2	11	4	2	9	4	3	0
WT 1055-1	46	6	7	49	12	6	24
WT 1055-2	165	4	4	142	3	27	55
WT 1055-3	122	10	29	111	12	23	64
WT 1055-4	93	13	34	107	21	47	51
WT 14-0	39	19	0	45	1	27	17

Table S2. Neurons imaged within individual mice for *in vivo* 1-photon calcium imaging data.

Appendix A. Long-Term *In Vivo* Molecular Monitoring Using Aptamer-Graphene Microtransistors

Introduction

The ability for real-time monitoring of specific molecules in complex biological environments found in vivo has been reported to play an important role in the diagnosis and management of human diseases such as mental health, diabetes, cardiac diseases, acute kidney disease, and cancer (Dauphin-Ducharme et al., 2019; Flynn et al., 2023; Freidel et al., 2023; Parolo et al., 2020; Sempionatto et al., 2022). To date, the design of biosensors for real-time molecular monitoring has faced many of the following technical challenges: (1) the biosensing platform must be generalizable, thereby making it easy to adapt the platform to new targets, (2) it must have sufficient sensitivity and selectivity both for the low (nM) concentrations of biomarkers and be robust to interference from other molecules with similar structures, and (3) it must be resistant to biofoulings and performance degradation for long-term and real-time monitoring.

Electrochemical aptamer-based (EAB) biosensors have demonstrated the potential to address the abovementioned challenges for real-time molecular monitoring in clinically relevant in vivo environments (Arroyo-Curras et al., 2017; Baker et al., 2006; Downs et al., 2022; Ferguson et al., 2013; Wu et al., 2022). Generally, EAB sensors consist of single-stranded DNA or RNA aptamers functionalized on the surface of a gold working electrode (Ferguson et al., 2013). Redox reporters, like methylene blue or ferrocene, are typically functionalized to one end of the aptamers, allowing for charge transfer upon the conformational change of aptamers caused by the binding of targets (Dauphin-Ducharme et al., 2023). More specifically, the binding and dissociation of

target analytes to aptamers cause the conformational rearrangement of aptamers, which changes the electron transfer rate between redox reporters and the working electrode and results in a measurable current change. This current change can be monitored by several electrochemical methods, like square-wave voltammetry and cyclic voltammetry (White et al., 2008). EAB sensors have been widely used for real-time monitoring of multiple therapeutic drugs and metabolites *in vivo* in small animal models (Dauphin-Ducharme et al., 2019; Idili et al., 2021). Nevertheless, the EAB sensors suffer from (1) limited in vivo measurement time and (2) difficulty in miniaturizing the EAB sensors down to micrometer scale (to be comparable with the CGM) considering the tradeoff between the magnitude of measurable current and the microscale sensor dimensions (Downs et al., 2022; Downs et al., 2021; Shaver and Arroyo-Curras, 2022).

Unlike simple electrode-based electrochemical transducers, transistors can simultaneously transduce and amplify the sensor signal, thereby enabling the miniaturization of aptamer-based electrochemical biosensors without sacrificing the signal-to-noise ratio (Bidinger et al., 2022). Among these, graphene field-effect transistor (gFET) has emerged as a high-performance platform for electrochemical biosensing due to the high carrier mobility of graphene and its atomic layer thickness, which enables the detection with high sensitivity (Fu et al., 2017). A graphene field-effect transistor biosensor is typically a three-terminal electronic device, in which source and drain terminals are bridged by sensing material, and current flow between source and drain electrodes is modulated by a gate terminal (Tran and Mulchandani, 2016). When the gate voltage is applied onto the surface of an gFET device through an

electrolyte, positive and negative charges are separated and form an electrostatic double layer, serving as an insulator to tune the conductivity of the device (Reiner-Rozman et al., 2015; Torricelli et al., 2021; Wang et al., 2021). Transistor-based aptamer sensors have been used as the new toolkits for real-time molecular monitoring in vivo (Gao et al., 2022; Wu et al., 2022). Nevertheless, like EAB sensors, these sensors can survive for only several hours in complex in vivo biological environments because of sensor degradation caused by biofouling, which impedes chronic performance (Wu et al., 2022; Zhao et al., 2021).

Here, we report aptamer-graphene microtransistors (AGMs) that incorporate a layer of pyrene(polyethylene glycol)5-alcohol (pyrene-PEG5-alcohol) and DNase inhibitors doped polyacrylamide hydrogel for long-term molecular monitoring in *in vivo* environments. These surface-coated AGMs exhibited the capability to monitor optogenetically evoked dopamine release in vivo in mice over one week. In freely moving mice, they successfully monitored endogenous dopamine release induced by animal behaviors such as the return of righting reflex (RORR) and sucrose consumption even after eight days of implantation. The development of this type of long-term aptamer biosensor for in vivo monoamine monitoring will serve as a benchmark and template for developing aptamer-based biosensors for long-term monitoring of a broad range of molecules in a host of biological environments.

Methods

Animals

Adult DAT-IRES-Cre mice were used in this study. Mice were 8-10 weeks old at the time of test, weighing 20-30 g each, group-housed, given access to food pellets and

water ad libitum, and maintained on a 12:12-hour light/dark cycle (lights on at 7:00 a.m.). Animals were held in a sound attenuated holding room facility in the lab starting at least one week prior to surgery, as well as post-surgery and throughout the duration of behavioral assays to minimize stress from transportation and disruption from foot traffic. All experimental procedures were approved by the Animal Care and Use Committee of the University of Washington and conformed to NIH guidelines.

Stereotaxic surgery

All surgeries were performed under 4% isoflurane anesthesia (Piramal Healthcare, Maharashtra, India). For testing of AGMs, adult mice were injected unilaterally with 600 nL of either AAV5EF1a-DIO-ChR2-eYFP virus (WUSTL Hope Center Viral Core, St. Louis, MO) or AAV5-EF1aDIO-eYFP (WUSTL Hope Center Viral Core, St. Louis, MO) into the ventral tegmental area (AP: -3.25, ML: 0.5, DV: -4.4) using a Hamilton syringe with a blunted needle. Four to five weeks after virus injection, fiber optic ferrules were chronically implanted above the VTA (AP: -3.25, ML: 1.6, DV: -4.3 at 15° angle) and dental cement (Lang Dental, Wheeling, IL) was applied to hold the ferrules in place. The AGM probe was then implanted in the nucleus accumbens shell (AP: 1.45, ML: 0.65, DV: -4.5). For fiber photometry experiments using dLight, adult mice were injected unilaterally with 600 nL of AAV-CAG-dLight1.3b (Lin Tian Lab, UC Davis) into the NAcSh (AP: 1.45, ML: 0.65, DV: -4.5) using a Hamilton syringe with a blunted needle. Four to five weeks after virus injection, fiber photometry ferrules were chronically implanted into the NAcSh (AP: 1.45, ML: 0.65, DV: -4.5). Mice were allowed to recover for at least six weeks following infusion of the virus prior to further behavioral testing to ensure optimal viral expression and implant placement location. All

experimental procedures were approved by the Animal Care and Use Committee of University of Washington and conformed to NIH guidelines.

Open-field test (OFT)

OFT testing was performed in a custom-made white box (50 cm × 50 cm) within a sound attenuated room maintained at 23°C. The 'center' area was defined as a square of 50% of the total OFT area. A light bulb mounted above provided 45 lux illumination, measured in the center of the arena. Mice were handled for 5 minutes per day for a week prior to the OFT testing. On the day of OFT testing, mice were habituated in a holding room for 30 minutes and then they were allowed to explore the entire chamber freely for 25 min. Sessions were recorded via a digital camera, and videos were analyzed offline using Ethovision XT 8.5 (Noldus Information Technologies). The open field was cleaned with 70% ethanol between each trial. Ethovision XT 8.5 (Noldus Information Technologies) quantified the total distance and time spent in the central and peripheral areas. Time spent in the center of the open field was used as a measure of anxiolysis. All experimental procedures were approved by the Animal Care and Use Committee of the University of Washington and conformed to NIH guidelines.

Optogenetic stimulation

Following stereotaxic surgery and implantation of the AGM probe in NAc, mice were connected to a 473 nm diode-pumped solid-state laser (OEM Laser Systems). Laser power was adjusted to obtain ~15 mW transmittance into the brain, at 20 Hz frequency with 5 ms pulse for 20 s. All experimental procedures were approved by the

Animal Care and Use Committee of the University of Washington and conformed to NIH guidelines.

Sucrose intake

Behaviorally tested mice were food deprived (mice still had access to water) for 24 hours prior to testing. Then, animals were given access to ~1 g of sucrose pellets and had free access to these pellets for approximately 15 minutes. After testing, food-deprived animals were returned to an ad libitum diet. Sessions were recorded via a digital camera, and videos were analyzed offline using Ethovision XT 8.5 (Noldus Information Technologies). All experimental procedures were approved by the Animal Care and Use Committee of the University of Washington and conformed to NIH guidelines.

Righting reflex

Behaviorally tested mice were anesthetized in an induction box with 2.5% isoflurane (Piramal Healthcare, Maharashtra, India) for ~5 minutes. Following this, mice were removed from anesthesia and placed into a recovery cage to exposure to the open air, until they exhibited righting reflex. After sufficient recovery time, the mice were returned to their home cage. Sessions were recorded via a digital camera, and videos were analyzed offline using Ethovision XT 8.5 (Noldus Information Technologies). All experimental procedures were approved by the Animal Care and Use Committee of the University of Washington and conformed to NIH guidelines.

Results

To evaluate the biocompatibility of the AGMs coated with DNase inhibitor-doped polyacrylamide hydrogel, we investigated inflammatory responses via measuring

device-induced gliosis, a reactive response to brain injury, within the deep brain AGM sensor implants. The sensors were implanted into the nucleus accumbens medial shell (NAcSh) of mice, and the glial immune response after 1 and 6 weeks of sensor implantation surgery was evaluated by immunohistochemical staining for DAPI (blue), astrocytes (GFAP, red), and activated microglia (Iba1, green) (**Fig. A1b**). Under consistent imaging settings, the post-implantation fluorescence intensity indicates a significant decrease in the immune response over the 6-week recovery period (**Fig. A1c-h**). Moreover, the immune response and tissue lesion area induced by our sensors were equivalent to those induced by other advanced thin-film deep brain implants (Jeong et al., 2015; Lu et al., 2018; Zhang et al., 2019).

We next examined the effects of polyacrylamide hydrogel-coated AGM probe implantation on the basal anxiety state and locomotor activity of mice to determine if the implant scheme would cause any aberrant behavioral effects. We implanted the probe into the NAcSh of mice (a dopamine rich brain region) and monitored their activity in an open field test 1 day prior to implantation and 1, 3, and 7 days after implantation, by recording locomotor activity and velocity (Phillips et al., 2003). The heatmaps for animal movement revealed comparable levels of locomotor activity between the day prior to implantation and seven days after implantation (**Fig. A1i**). Moreover, no significant differences were found over time when comparing preimplantation (1 day) and post-implantation (7 days) in both distance traveled and average velocity (**Fig. A1j-k**). Overall, these results establish that the sensor implantation does not have significant effects on basal anxiety and locomotor activity in the mice over the prolonged duration of the implantation period.

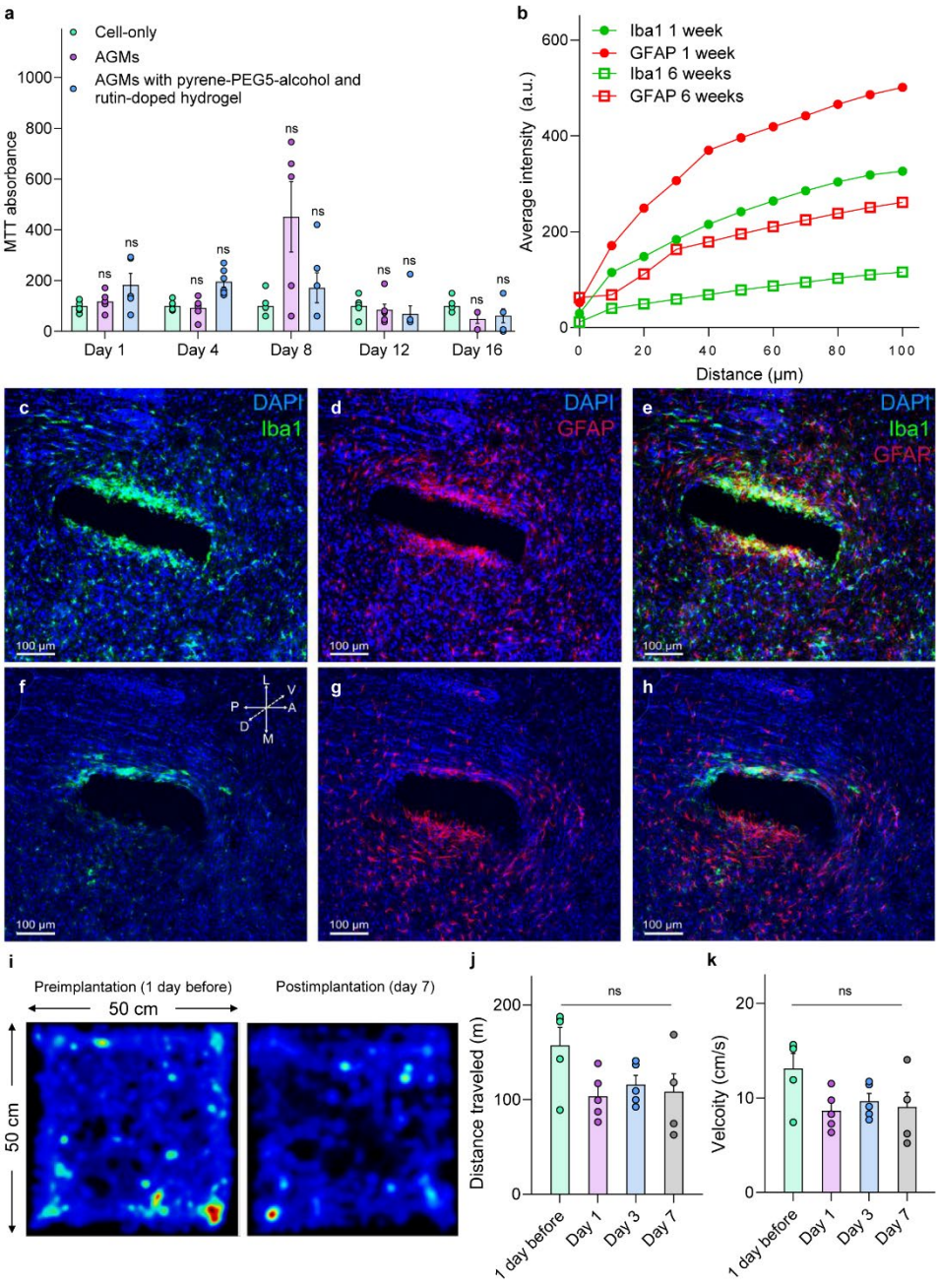

Figure A1. Biocompatibility of DNase inhibitor-doped polyacrylamide hydrogel coatings and the impact of sensor implantation on brain tissue and animal behaviors.
(**a**) MTT absorbance of induced neural progenitor cells (iNPCs) cocultured with AGMs with different coatings. ns refers to not significant. (**b**) Representative changes in intensity within region of interest (ROI) as the distance from sensors increases for both Iba1 (green) and GFAP (red) at 1 week (closed circle) and 6 weeks (open square). (**c-h**) Confocal fluorescence images of horizontal brain slices show immunohistochemical staining for DAPI (blue), astrocytes (GFAP, red), and activated microglia (Iba1, green) and overall lesion from sensor implantation after 1 week (c-e) and 6 weeks (**f-h**). All histological and confocal settings were kept consistent across groups, 20× (Scale bars, 100 μm). (**i**) Animal motion heatmap for preimplantation (1 day before implantation) and postimplantation (after 7 days). (**j**) Total traveling distance and (**k**) velocity for mice in an open-field assay at four different stages: 1 day before implantation, and 1, 3, and 7 days postimplantation. n = 5; ns indicates that the difference of the means is not significant at the 0.05 level. All data are represented as means ± SEM.

Encouraged by the long-term operational characteristics from the AGMs coated with DNase inhibitor-doped polyacrylamide hydrogel in vitro, we next evaluated the capability for long-term monitoring in vivo using a mouse model. Cre-recombinase-dependent viral vectors containing the light-sensitive cation channel channelrhodopsin-2 (ChR2) were unilaterally injected into the ventral tegmental area (VTA) of DAT-cre mice, with a fiber optic ferrule implanted above the VTA and the AGM probe with surface coating implanted into the NAcSh (**Fig. A2a-b**). We then delivered photostimulation to the VTA (20 Hz, 5 ms pulse width), a well-established parameter for inducing phasic dopamine release, while monitoring the resulting dopamine release in the NAcSh using the AGM by performing continuous transfer curve scanning (Kim et al., 2013; Patriarchi et al., 2018; Tsai and Zhang, 2009). As shown in **Fig. A2c**, the transfer curves first shift to the rightward during photostimulation and then shift back to the left after stimulation ends. Accordingly, the sensor response shows a rapid increase during stimulation and a slow decrease following the end of stimulation (**Fig. A2d**). We then investigated the long-term monitoring of optically evoked dopamine release over 10 days (**Fig. A2e**). The AGMs with surface coatings successfully captured the optogenetically evoked dopamine release from day 1 through day 7. The peak response gradually decreased over subsequent days, and no clear response peak was obtained on day 10. This result further highlights the importance of rutin doping to prevent in vivo sensor performance degradation from endogenous nucleases. **Fig. A2f** shows the sensor response before and during photostimulation, in which only the optically evoked dopamine release caused a robust and significant response.

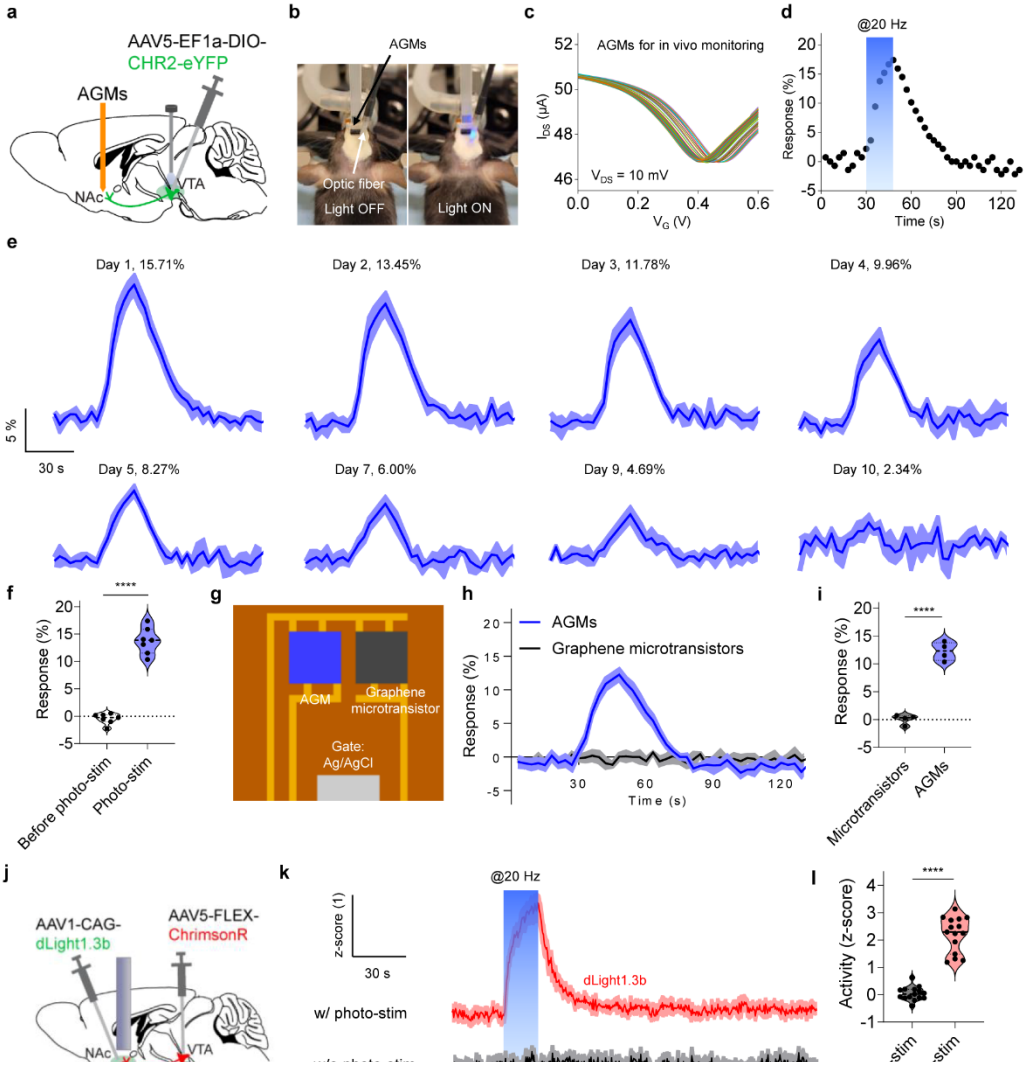

Figure A2. Long-term monitoring of optically evoked dopamine release *in vivo*.
(**a**) Schematic illustration of AGMs implanted in NAcSh with ChR2 injected and optic fiber implanted in VTA. (**b**) Optical images of a mouse implanted with AGMs and optical fiber. (**c**) Representative transfer curves of the AGMs during photostimulation process. The time interval between each transfer curve is 3 s, and the scanning step is 3 mV for VG. (**d**) The sensor response to dopamine release evoked by photostimulation at 20 Hz and 5 ms pulse width. (**e**) Long-term monitoring of optogenetically evoked dopamine release in vivo using AGMs with surface coatings. The shading area represents ± SEM from three samples. (**f**) Comparison of the sensor response to dopamine release before and during photostimulation on day 1. n = 7; ****P < 0.0001. All data are represented as means ± SEM. (**g**) Schematic illustration of an implantable probe that contains graphene microtransistor with and without the aptamer functionalization. (**h**) Simultaneous operation of graphene microtransistor and AGM channels for real-time dopamine monitoring during photostimulation. The shading area represents ± SEM from four samples. (**i**) Sensor response to optogenetically evoked dopamine release for graphene microtransistor and AGM channels. n = 4; ****P < 0.0001. All data are represented as means ± SEM. (**j**) Schematic illustration of the mouse brain injected with ChrimsonR in VTA, and dLight injected and optic fiber implanted in NAcSh. (**k**) Averaged traces of dLight1.3b response in NAcSh with and without the photostimulation (20 Hz, 5 ms pulse width). The shading area represents ± SEM from 5 mice (15 tests). (**l**) Calculated response to dopamine release detected by dLight1.3b. n = 15; ****P < 0.0001. All data are represented as means ± SEM.

To further determine whether the sensor response is due to the interaction between the optically-induced dopamine release and the aptamer monolayer on the sensor surface, we designed an implantable neural probe that contains both AGM channel and graphene microtransistor only channel (**Fig. A2g**). The probe was then passivated with pyrene-PEG5-alcohol and coated with rutindoped polyacrylamide hydrogel. The probe with these two channels was implanted into the NAcSh of DAT-cre mice to monitor optically evoked dopamine release. More specifically, when the light was delivered through VTA terminal stimulation (20 Hz, 5 ms pulse width), the two channels on the implanted probe were monitored simultaneously. **Fig. A2h** shows a rapid increase in the sensor response for the AGM channel, while the graphene microtransistor channel (without aptamer functionalization) shows no clear response, indicating that the sensor response is attributed to the interaction between the surface functionalized aptamers and released dopamine molecules (**Fig. A2i**). We reason that the hydrogel coating could eliminate the influence from the electrophysiological signal through the gate electrode. Moreover, the dopamine release signal was recorded every 3 s, whereas the temporal resolution of the electrophysiological signal is in the range of milliseconds. These studies further support that the obtained transfer curve shift is indeed due to the dopamine release induced by photostimulation. Overall, these results indicate that DNase inhibitor-doped hydrogel coatings can effectively extend the lifetime of AGMs to over one week for in vivo monitoring of neurotransmitter release.

To compare the AGM biosensor with other emerging biosensors, genetically encoded fluorescent indicators, we injected Cre-recombinase-dependent viral vectors containing the lightsensitive cation channel ChrimsonR into the VTA of DAT-cre mice,

along with genetically encoded fluorescent dopamine indicator dLight and a fiber photometry implant into the NAcSh (**Fig. A2j**) (Patriarchi et al., 2018). We then delivered photostimulation (20 Hz, 5 ms pulse width) above the NAcSh. A significant peak response was obtained from stimulation followed by a decay in signal post-stimulation, similar to the response of the AGMs (**Fig. A2k-l**). These results indicate that the hardware-based AGMs demonstrate comparable performance for dopamine release detection to comparable and existing sensing technology. The genetically encoded fluorescent indicator offers a high-resolution benchmark for our AGMs. This technology, however, has limited translational potential due to complicated genetic modifications.

We next measured the capability of AGMs to record in vivo endogenous dopamine release induced through behaviors such as righting reflex and sucrose reward consumption. RORR is an established behavioral means to assess behavioral responsiveness in rodents, and it has been reported that NAcSh dopamine increases during this process (Bao et al., 2021). RORR is assessed as the time for rodent take to return to a prone position following anesthesia. We used this method to establish the ability of our device with surface coating to monitor endogenous dopamine dynamics. As shown in **Fig. A3a-b**, the RORR process is demonstrated on a mouse following AGM implantation into the VTA. Eight days following implantation, transfer curves were continuously monitored at the time of righting, and a rapid increase in sensor response was obtained by the AGMs compared to baseline measurements of the transfer curves (**Fig. A3c**). We then calculated the overall response before and during RORR and found a significant difference between the baseline and when the mice demonstrate RORR, suggesting the dopamine release in the NAcSh during this process (**Fig. A3d**).

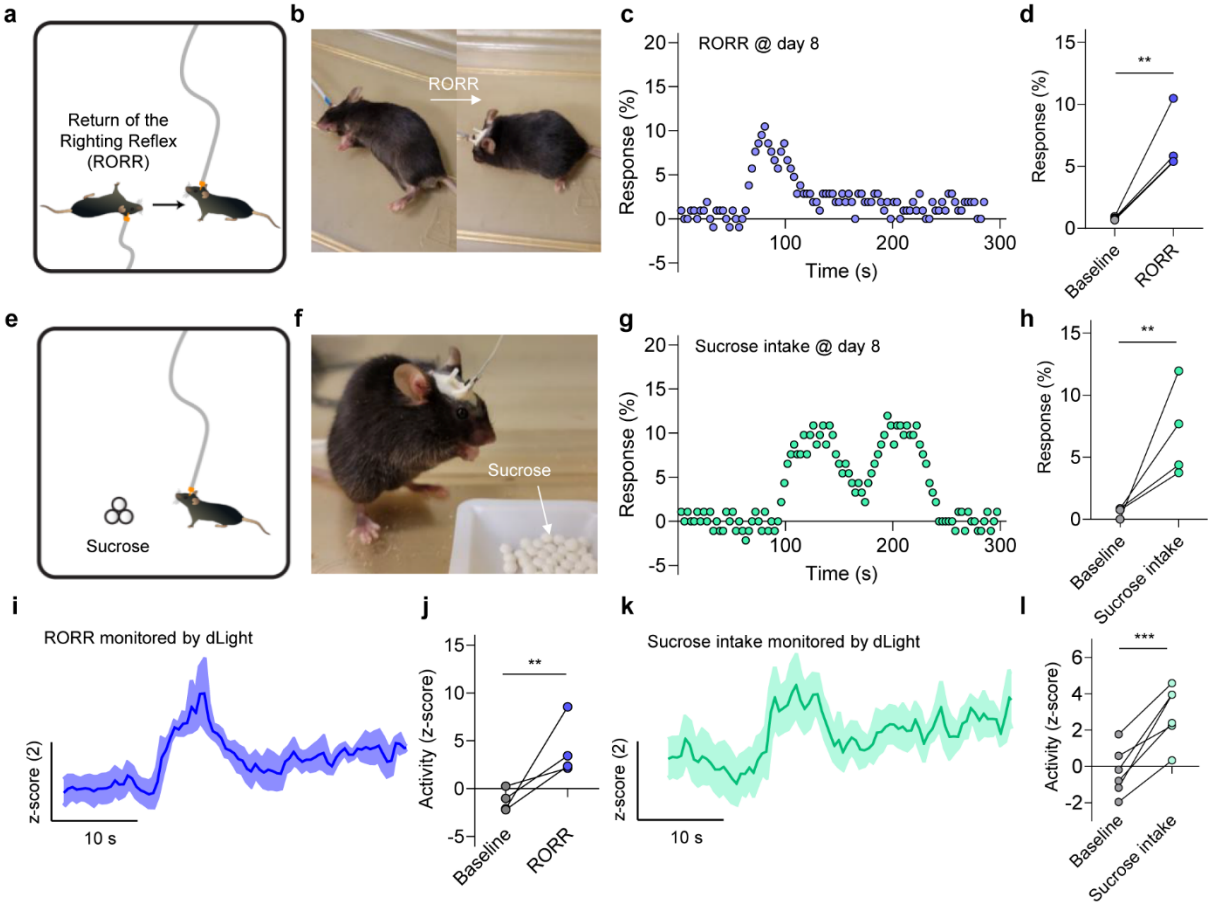

Figure 6. Long-term monitoring of dopamine release during animal behavior events.
(**a**) Schematic illustration of the return of righting reflex (RORR). (**b**) Optical images of a mouse during RORR. (**c**) The representative sensor response during RORR after eight days of sensor implantation. The time interval between each data point is 3 s. (**d**) Comparison of the sensor response before and during the RORR. n = 4; **P < 0.01. All data are represented as means ± SEM. (**e**) Schematic illustration of sucrose intake behavior. (**f**) Image of a mouse during sucrose intake behavior. (**g**) The representative sensor response during sucrose intake after eight days of sensor implantation. (**h**) Comparison of the sensor response before and during sucrose intake. n = 4; **P < 0.01. All data are represented as means ± SEM. (**i**) Representative trances of dopamine release signal during RORR detected by dLight method. (**j**) Comparison of the dLight signal response to dopamine release during the RORR. n = 4, **P < 0.01. All data are represented as means ± SEM. (**k**) Representative trances of dopamine release signal during sucrose intake detected by dLight method. (**l**) Comparison of the dLight signal response to dopamine during the sucrose intake. n = 6, ***P < 0.001. All data are represented as means ± SEM.

We also tested the capabilities of AGMs with sucrose reward consumption, which is well established to evoke robust dopamine release within the NAcSh (Hajnal and Norgren, 2001; Hajnal and Norgren, 2002; McCutcheon et al., 2012). After 8 days of sensor implantation in the NAcSh, mice were placed into a chamber with free access to sucrose pellets while continuous dopamine recording was collected (**Fig. A3e-f**). An increase in dopamine signal response was observed when the mice began consuming sucrose pellets, and the signal gradually returned to baseline when the mice stop feeding (**Fig. A3g-h**). When comparing baseline measurements to the peak response during sucrose reward consumption, a significant difference was observed, establishing detection of behaviorally evoked endogenous dopamine release by our AGM-coating strategy. Comparable dopamine release was also detected by the dLight biosensor in a series of side-by-side experiments, further establishing that the AGMs can be reliably used to monitor dopamine in vivo in freely moving animals (**Fig. A3i-l**). These successful sub-chronic monitoring of behaviorally induced in vivo dopamine release further highlights the feasibility of surface-coated AGMs for widespread use in behavioral studies and neural circuit dissection over long time frames and in more complex scenarios.

Discussion

Aptamer-based electrochemical biosensors are emerging high-performance sensing platforms for real-time molecular monitoring in undiluted whole blood samples and complex in vivo biological environments. Yet, the longevity of these sensors has been a significant challenge. To date, the in vivo operation of existing aptamer-based electrochemical biosensors is limited to a few hours (12 hours at most), which greatly

hampers applications in which one to several weeks-long operation is needed, like therapeutic drug monitoring, neurochemical monitoring, and protein detection for immunoengineering. Here, we demonstrate significant progress in solving this longstanding challenge by developing a first-generation long-term, real-time molecular monitoring platform, AGMs, in undiluted whole blood samples and complex in vivo environments. The long-term operation is achieved by a combined effect of 1) pyrene-PEG5-alcohol passivation and 2) DNase inhibitor-doped polyacrylamide hydrogel coatings. MTT analysis of forebrain organoids cocultured with these coatings and in vivo immunohistochemistry study indicate their biocompatibility for use in in vivo real-time molecular monitoring. The reported sensors allow for long-term (over one week) monitoring of optically evoked dopamine release in vivo using mice models. In addition, the monitoring of animal behavior (RORR and sucrose reward consumption) induced dopamine release by the AGMs is successfully demonstrated. Compared with the hourlong operation of existing aptamer-based biosensors in in vivo studies, this multi-day (over one week) operation significantly extends the in vivo operation lifetime and marks a new benchmark for aptamer-based biosensors in complex in vivo environments.

In addition to the significantly improved in vivo operational lifetime, the AGMs simultaneously transduce the interaction between aptamers and targets of interest and amplify the resulting signals, which makes it possible for the miniaturization of sensor size down to micrometer scale (50 μm × 50 μm of each sensor) without sacrificing the signal-to-noise ratio. In contrast, when the electrode size of aptamer-electrochemical biosensors is miniaturized down to such micrometer scale without incorporating porous

structures, the magnitude of the resulting current would be as low as nA. The reported minimum current range for the state-of-the-art miniaturized potentiostat module (EmStat Pico) is 100 nA. Therefore, the accurate detection of such low currents often requires sophisticated and bulky electrochemical data acquisition systems, which adds additional challenges to customized circuit design for developing sensors for real-time molecular monitoring in a wearable platform like CGM.

Overall, the surface-coated AGMs extend the in vivo operation lifetime of aptamer-based biosensors from a few hours to week-long time scales, which opens the avenue for long-term molecular sensing in complex biological environments in several settings. These include behavioral neural circuit analysis, disease modeling, therapeutic drug monitoring, immune monitoring, and chronic disease management. Future work includes further extending the lifetime of AGMs to even longer time scales (like CGM) by optimizing formulations of surface coatings, developing platforms for multiplexed monitoring of neurotransmitters, alongside neuropeptides, in freely moving animals, and developing a feedback-controlled system for molecular monitoring and on-demand medical interventions. The technology we present here represents a first-generation long-term aptamer-based biosensor for in vivo molecular monitoring and serves as a unique template for the design of future iterations with added functionality, longevity, and operational modes.

References

Acsády, L., Kamondi, A., Sík, A., Freund, T. & Buzsáki, G. GABAergic cells are the major postsynaptic targets of mossy fibers in the rat hippocampus. *J. Neurosci.* **18**, 3386–3403 (1998).

Adams, R.E. & Boscarino, J.A. Differences in mental health outcomes among Whites, African Americans, and Hispanics following a community disaster. *Psychiatry* **68**, 250-65 (2005).

Amaral, D.G. & Campbell, M. Transmitter systems in the primate dentate gyrus. *Hum. Neurobiol.* **5**, 169–180 (1986).

Amaral, D.G., Scharfman, H.E. & Lavenex, P. The dentate gyrus: fundamental neuroanatomical organization (dentate gyrus for dummies). *Prog. Brain Res.* **163**, 3–22 (2007).

American Psychiatric Association. Anxiety disorders. *Diagnostic and statistical manual of mental disorders* **5** (2013).

Arnsten, A. F. Through the looking glass: differential noradenergic modulation of prefrontal cortical function. *Neural Plast.* **7**, 133–146 (2000).

Arnsten, A.F. Stress signalling pathways that impair prefrontal cortex structure and function. *Nat. Rev. Neurosci.* **10**, 410-422 (2009).

Arnsten, A. F. Catecholamine influences on dorsolateral prefrontal cortical networks. *Biol. Psychiatry* **69**, e89–e99 (2011).

Arnsten, A.F. The use of α-2A adrenergic agonists for the treatment of attention deficit/hyperactivity disorder. *Expert Rev. Neurother.* **10**, 1595-1605 (2011).

Aston-Jones G. & Bloom F.E. Activity of norepinephrine-containing locus coeruleus neurons in behaving rats anticipates fluctuations in the sleep-waking cycle. *J. Neurosci.* **1**, 876-886 (1981).

Aston-Jones, G. & Bloom, F.E. Norepinephrine-containing locus coeruleus neurons in behaving rats exhibit pronounced responses to non-noxious environmental stimuli. *J. Neurosci.* **1**, 887–900 (1981).

Aston-Jones, G., Rajkowski, J. & Cohen, J. Role of locus coeruleus in attention and behavioral flexibility. *Biol. Psychiatry* **46**, 1309–1320 (1999).

Aston-Jones, G. & Cohen, J.D. An integrative theory of locus coeruleus-norepinephrine function: adaptive gain and optimal performance. *Annu. Rev. Neurosci.* **28**, 403–450 (2005).

Baker, S. et al. The human dentate gyrus plays a necessary role in discriminating new memories. *Curr. Biol.* **26**, 2629–2634 (2016).

Bartos, M. et al. Fast synaptic inhibition promotes synchronized gamma oscillations in hippocampal interneuron networks. *Proc. Natl Acad. Sci. USA* **99**, 13222–13227 (2002).

Bernier, B.E. et al. Dentate gyrus contributes to retrieval as well as encoding: evidence from context fear conditioning, recall, and extinction. *J. Neurosci.* **37**, 6359–6371 (2017).

Berridge, C.W. & Spencer, R.C. Differential cognitive actions of norepinephrine a2 and a1 receptor signaling in the prefrontal cortex. *Brain Res*. **1641**, 189-196 (2016).

Berridge, C.W. & Waterhouse, B.D. The locus coeruleus-noradrenergic system: modulation of behavioral state and state-dependent cognitive processes. *Brain Res. Rev.* **42**, 33-84 (2003).

Besnard, A. & Sahay, A. Adult Hippocampal Neurogenesis, Fear Generalization, and Stress. *Neuropsychopharmacology* **41**, 24-44 (2016).

Bezin, L., Marcel, D., Desgeorges, S., Pujol, J. F. & Weissmann, D. Singular subsets of locus coeruleus neurons may recover tyrosine hydroxylase phenotype transiently expressed during development. *Mol. Brain Res.* **76**, 275–281 (2000).

Blackstad, T.W., Fuxe, K. & Hökfelt, T. Noradrenaline Nerve Terminals in the Hippocampal Region of the Rat and the Guinea Pig. *Z. Zellforsch Mikrosk Anat.* **78**, 463-473 (1967).

Bonanno, G.A., Romero, S.A. & Klein, S.I. The temporal elements of psychological resilience: an integrative framework for the study of individuals, families, and communities. *Psychol Inquiry* **26**,139-69 (2015).

Borzello, M. et al. Assessments of dentate gyrus function: discoveries and debates. *Nat Rev Neurosci.* **24**, 502-517 (2023).

Boucetta, S., Cissé, Y., Mainville, L., Morales, M., & Jones, B.E. Discharge profiles across the sleep-waking cycle of identified cholinergic, GABAergic, and glutamatergic neurons in the pontomesencephalic tegmentum of the rat. *J. Neurosci.* **34**, 4708–4727 (2014).

Bouret, S. & Sara, S.J. Reward expectation, orientation of attention and locus coeruleus-medial frontal cortex interplay during learning. *Eur. J. Neurosci.* **20**, 791–802 (2004).

Bouret, S. & Sara, S.J. Network reset: a simplified overarching theory of locus coeruleus noradrenaline function. *Trends Neurosci.* **28**, 574–582 (2005).

Breton-Provencher, V. & Sur, M. Active control of arousal by a locus coeruleus GABAergic circuit. *Nat. Neurosci.* **22**, 218–228 (2019).

Breton-Provencher, V. et al. Locus Coeruleus Norepinephrine in Learned Behavior: Anatomical Modularity and Spatiotemporal Integration in Targets. *Front Neural Circuits* **15**, 638007 (2021).

Brewin, C.R., Andrews, B. & Valentine, J.D. Meta-analysis of risk factors for posttraumatic stress disorder in trauma-exposed adults. *J Consult Clin Psychol* **68**, 748-66 (2000).

Britton, K.T. et al. Dissociation between in vivo hippocampal norepinephrine response and behavioral/neuroendocrine responses to noise stress in rats. *Brain Res.* **574**, 125-130 (1992).

Bryant, R.A. Acute stress disorder as a predictor of posttraumatic stress disorder: a systematic review. *J Clin Psychiatry* **72**, 233-9 (2011).

Bryant, R.A. Post-traumatic stress disorder: a state-of-the-art review of evidence and challenges. *World Psychiatry* **18**, 259-269 (2019).

Cameron, H., Woolley, C., McEwen, B. & Gould, E. Differentiation of newly born neurons and glia in the dentate gyrus of the adult rat. *Neuroscience* **56**, 337–344 (1993).

Campeau, S. et al. Stress Rapidly Increases Alpha-1d Adrenergic Receptor mRNA in the Rat Dentate Gyrus. *Brain Res.* **1323**, 109-118 (2010).

Carter, M.E. et al. Tuning arousal with optogenetic modulation of locus coeruleus neurons. *Nat. Neurosci.* **13**, 1526-1533 (2010).

Castren, E., Thoenen, H. & Lindholm, D. Brain-derived neurotrophic factor messenger RNA is expressed in the septum, hypothalamus and in adrenergic brain stem nuclei of adult rat brain and is increased by osmotic stimulation in the paraventricular nucleus. *Neuroscience* **64**, 71–80 (1995).

Cedarbaum, J.M. & Aghajanian, G.K. Afferent projections to the rat locus coeruleus as determined by a retrograde tracing technique. *J. Comp. Neurol.* **178**, 1-16 (1978).

Chawla, M.K. et al. Sparse, environmentally selective expression of Arc RNA in the upper blade of the rodent fascia dentata by brief spatial experience. *Hippocampus* **15**, 579–586 (2005).

Christie, M.J. Generators of synchronous activity of the locus coeruleus during development. *Semin. Cell Dev. Biol.* **8**, 29–34 (1997).

Clelland, C.D. et al. A functional role for adult hippocampal neurogenesis in spatial pattern separation. *Science* **325**, 210–213 (2009).

Corkin, S. What's new with the amnesic patient H.M.? *Nat. Rev. Neurosci.* **3**, 153–160 (2002).

Cox, D.J., Racca, C. & LeBeau, F.E. Beta-adrenergic receptors are differentially expressed in distinct interneuron subtypes in the rat hippocampus. *J. Comp. Neurol.* **509**, 551-565 (2008).

Cox, J., Pinto, L. & Dan, Y. Calcium imaging of sleep-wake related neuronal activity in the dorsal pons. *Nat. Commun.* **7**, 10763 (2016).

Creamer, M., Burgess, P. & McFarlane, A.C. Post-traumatic stress disorder: findings from the Australian National Survey of Mental Health and Well-being. *Psychol Med* **31**,1237-47 (2001).

Danielson, N.B. et al. Distinct Contribution of Adult-Born Hippocampal Granule Cells to Context Encoding. *Neuron* **90**, 101-112 (2016).

Danielson, N.B. et al. In vivo imaging of dentate gyrus mossy cells in behaving mice. *Neuron* **93**, 552–559.e4 (2017).

Debiec, J. & Sullivan, R.M. The neurobiology of safety and threat learning in infancy. Neurobiol. Learn. Mem. 143, 49–58 (2017).

Deng, W., Mayford, M. & Gage, F.H. Selection of Distinct Populations of Dentate Granule Cells in Response to Inputs as a Mechanism for Pattern Separation in Mice. *Elife* **2**, e00312 (2013).

Denny, C.A., Burghardt, N.S., Schachter, D.M., Hen, R. & Drew, M.R. 4- to 6-week-old adult-born hippocampal neurons influence novelty-evoked exploration and contextual fear conditioning. *Hippocampus* **22**, 1188–1201 (2012).

Devilbiss, D.M. & Waterhouse, B.D. Phasic and tonic patterns of locus coeruleus output differentially modulate sensory network function in the awake rat. *J Neurophysiol.* **105**, 69-87 (2011).

Diamantaki, M., Frey, M., Preston-Ferrer, P. & Burgalossi, A. Priming spatial activity by single-cell stimulation in the dentate gyrus of freely moving rats. *Curr. Biol.* **26**, 536–541 (2016).

Diehl, G.W., Hon, O.J., Leutgeb, S. & Leutgeb, J.K. Stability of medial entorhinal cortex representations over time. *Hippocampus* **29**, 284–302 (2019).

DiGrande, L. et al. Posttraumatic stress symptoms, PTSD, and risk factors among lower Manhattan residents 2-3 years after the September 11, 2001 terrorist attacks. *J Trauma Stress* **21**, 264-73 (2008).

Ewell, L. A. & Jones, M. V. Frequency-tuned distribution of inhibition in the dentate gyrus. *J. Neurosci.* **30**, 12597–12607 (2010).

Fa, M.X. et al. Stress modulation of hippocampal activity-spotlight on the dentate gyrus. *Neurobiol Learn Mem.* **112**, 53-60 (2014).

Fanselow, M.S. Contextual fear, gestalt memories, and the hippocampus. *Behav. Brain Res.* **110**, 73–81 (2000).

Feng, J. et al. A Genetically Encoded Fluorescent Sensor for Rapid and Specific In Vivo Detection of Norepinephrine. *Neuron* **102**, 745-761 (2019).

Foote, S.L. et al. Impulse activity of locus coeruleus neurons in awake rats and monkeys is a function of sensory stimulation and arousal. *Proc. Natl. Acad. Sci. USA.* **77**, 3033-3037 (1980).

Forbes D. et al. Trauma at the hands of another: longitudinal study of differences in the posttraumatic stress disorder symptom profile following interpersonal compared with noninterpersonal trauma. *J Clin Psychiatry* **73**, 372-6 (2012).

Franowicz, J.S. et al. Mutation of the alpha2A-adrenoceptor impairs working memory performance and annuls cognitive enhancement by guanfacine. *J. Neurosci.* **22**, 8771-8777 (2002).

Gazarini, L., Stern, C.A., Carobrez, A.P. & Bertoglio, L.J. Enhanced noradrenergic activity potentiates fear memory consolidation and reconsolidation by differentially recruiting α1- and β-adrenergic receptors. *Learn. Mem.* **20**, 210-219 (2013).

Glennon, E. et al. Locus coeruleus activation accelerates perceptual learning. *Brain Res.* **1709**, 39–49 (2019).

GoodSmith, D. et al. Spatial representations of granule cells and mossy cells of the dentate gyrus. *Neuron* **93**, 677–690.e5 (2017).

Grella, S.L. et al. Locus coeruleus phasic, but not tonic, activation initiates global remapping in a familiar environment. *J. Neurosci.* **39**, 445–455 (2019).

Grzanna, R. & Molliver, M.E. The locus coeruleus in the rat: an immunohistochemical delineation. *Neuroscience.* **5**, 21-40 (1980).

Hagena, H., Hansen, N. & Manahan-Vaughan, D. β-Adrenergic Control of Hippocampal Function: Subserving the Choreography of Synaptic Information Storage and Memory. *Cereb. Cortex* **26**, 1349-1364 (2016).

Hainmueller, T. & Bartos, M. Parallel emergence of stable and dynamic memory engrams in the hippocampus. *Nature* **558**, 292–296 (2018).

Hainmueller, T. & Bartos, M. Dentate gyrus circuits for encoding, retrieval and discrimination of episodic memories. *Nat. Rev. Neurosci.* **21**, 153–168 (2020).

Han, X. et al. A High-Light Sensitivity Optical Neural Silencer: Development and Application to Optogenetic Control of Non-Human Primate Cortex. *Front. Syst. Neuro.* **5**, 18 (2011).

Hansen, N. & Manahan-Vaughan, D. Locus coeruleus stimulation facilitates long-term depression in the dentate gyrus that requires activation of β-adrenergic receptors. *Cereb. Cortex* **25**, 1889–1896 (2015).

Hansen, N. & Manahan-Vaughan, D. Hippocampal long-term potentiation that is elicited by perforant path stimulation or that occurs in conjunction with spatial learning is tightly controlled by β-adrenoreceptors and the locus coeruleus. *Hippocampus* **25**, 1285–1298 (2015).

Hargreaves, E.L., Rao, G., Lee, I. & Knierim, J.J. Major dissociation between medial and lateral entorhinal input to dorsal hippocampus. *Science* **308**, 1792–1794 (2005).

Harley, C., Milway, J.S. & Lacaille, J.C. Locus coeruleus potentiation of dentate gyrus responses: evidence for two systems. *Brain Res. Bull.* **22**, 643–650 (1989).

Harley, C.W. Norepinephrine and the Dentate Gyrus. *Prog. Brain. Res.* **163**, 299-318 (2007).

Hassani, O. K. et al. The noradrenergic system is necessary for survival of vulnerable midbrain dopaminergic neurons: implications for development and Parkinson's disease. *Neurobiol. Aging* **85**, 22–37 (2020).

Hendrickson, R.C. & Raskind, M.A. Noradrenergic dysregulation in the pathophysiology of PTSD. *Exp Neurol* **284**, 181-95 (2016).

Hennings, A.C., McClay, M., Lewis-Peacock, J.A. & Dunsmoor, J.E. Contextual reinstatement promotes extinction generalization in healthy adults but not PTSD. *Neuropsychologia* **147**, 107573 (2020).

Henze, D.A., Wittner, L. & Buzsáki, G. Single granule cells reliably discharge targets in the hippocampal CA3 network in vivo. *Nat. Neurosci.* **5**, 790–795 (2002).

Hickey, L. et al. Optoactivation of locus ceruleus neurons evokes bidirectional changes in thermal nociception in rats. *J. Neurosci*. **34**, 4148-4160 (2014).

Hirschberg, S., Li, Y., Randall, A., Kremer, E.J. & Pickering, A.E. Functional dichotomy in spinal- vs prefrontal-projecting locus coeruleus modules splits descending noradrenergic analgesia from ascending aversion and anxiety in rats. *eLife* **6**, e29808 (2017).

Holets, V.R. et al. Locus coeruleus neurons in the rat containing neuropeptide Y, tyrosine hydroxylase or galanin and their efferent projections to the spinal cord, cerebral cortex and hypothalamus. *Neuroscience.* **24**, 893-906 (1988).

Houser, C.R. Interneurons of the Dentate Gyrus: An Overview of Cell Types, Terminal Fields and Neurochemical Identity. *Prog. Brain. Res.* **163**, 217–232 (2007).

Howe, M.W., Tierney, P.L., Sandberg, S.G., Phillips, P.E. & Graybiel, A.M. Prolonged Dopamine Signalling in Striatum Signals Proximity and Value of Distant Rewards. *Nature* **500**, 575-579 (2013).

Hunsaker, M.R., Rosenberg, J.S. & Kesner, R.P. The role of the dentate gyrus, CA3a, b, and CA3c for detecting spatial and environmental novelty. *Hippocampus*.**18**, 1064-73 (2008).

Ison, M.J., Quian Quiroga, R. & Fried, I. Rapid encoding of new memories by individual neurons in the human brain. *Neuron* **87**, 220–230 (2015).

Jahn, C. I. et al. Dual contributions of noradrenaline to behavioural flexibility and motivation. *Psychopharmacology* **235**, 2687–2702 (2018).

Jennings, J.H. et al. Visualizing Hypothalamic Network Dynamics for Appetitive and Consummatory Behaviors. *Cell* **160**, 516-527 (2015).

Jimenez, J.C. et al. Anxiety Cells in a Hippocampal-Hypothalamic Circuit. *Neuron* **97**, 670-683 (2018).

Jimenez, J.C. et al. Contextual fear memory retrieval by correlated ensembles of ventral CA1 neurons. *Nat. Commun.* **11**, 3492 (2020).

Jones, B.E. & Yang, T.−Z. The efferent projections from the reticular formation and the locus coeruleus studied by anterograde and retrograde axonal transport in the rat. *J. Comp. Neurol.* **242**, 56–92 (1985).

Josselyn, S. A., Köhler, S. & Frankland, P. W. Finding the engram. *Nat. Rev. Neurosci.* **16**, 521–534 (2015).

Kalwani, R.M., Joshi, S. & Gold, J.I. Phasic activation of individual neurons in the locus ceruleus/subceruleus complex of monkeys reflects rewarded decisions to go but not stop. *J. Neurosci.* **34**, 13656–13669 (2014).

Kaouane, N. et al. Glucocorticoids Can Induce PTSD-like Memory Impairments in Mice. *Science* **335**, 1510-1513 (2012).

Kaufman, A.M., Geiller, T. & Losonczy, A. A Role for the Locus Coeruleus in Hippocampal CA1 Place Cell Reorganization during Spatial Reward Learning. *Neuron* **105**, 1018-1026 (2020).

Keene, C.S. et al. Complementary functional organization of neuronal activity patterns in the perirhinal, lateral entorhinal, and medial entorhinal cortices. *J. Neurosci.* **36**, 3660–3675 (2016).

Kempadoo, K.A., Mosharov, E.V., Choi, S.J., Sulzer, D. & Kandel, E.R. Dopamine Release From the Locus Coeruleus to the Dorsal Hippocampus Promotes Spatial Learning and Memory. *Proc. Natl. Acad. Sci. U S A.* **113**, 14835-14840 (2016).

Kessler, R.C. et al. Posttraumatic stress disorder in the National Comorbidity Survey. *Arch Gen Psychiatry* **52**,1048-60 (1995).

Kheirbek, M.A., Klemenhagen, K.C., Sahay, A. & Hen, R. Neurogenesis and Generalization: A New Approach to Stratify and Treat Anxiety Disorders. *Nat. Neurosci.* **15**, 1613-1620 (2012).

Kim, S., Kim, Y., Lee, S.-H. & Ho, W.-K. Dendritic spikes in hippocampal granule cells are necessary for long-term potentiation at the perforant path synapse. *eLife* **7**, e35269 (2018).

Kitamura, T. et al. Entorhinal cortical ocean cells encode specific contexts and drive context-specific fear memory. *Neuron* **87**, 1317–1331 (2015).

Kitayama, N., Quinn, S. & Bremner, J.D. Smaller volume of anterior cingulate cortex in abuse-related posttraumatic stress disorder. *J Affect Disord* **90**, 171-4 (2006).

Klapoetke, N., Murata, Y., Kim, S. et al. Independent optical excitation of distinct neural populations. *Nat Methods* **11**, 338–346 (2014).

Knierim, J. J., Lee, I. & Hargreaves, E. L. Hippocampal place cells: parallel input streams, subregional processing, and implications for episodic memory. *Hippocampus* **16**, 755–764 (2006).

Knierim, J. J., Neunuebel, J. P. & Deshmukh, S. S. Functional correlates of the lateral and medial entorhinal cortex: objects, path integration and local–global reference frames. *Philos. Trans. R. Soc. B Biol. Sci.* **369**, 20130369 (2014).

Koylu, E.O., Smith, Y., Couceyro, P.R. & Kuhar, M.J. CART peptides colocalize with tyrosine hydroxylase neurons in rat locus coeruleus. *Synapse* **31**, 309–311 (1999).

Kuhn, H. G., Toda, T. & Gage, F. H. Adult hippocampal neurogenesis: a coming-of-age story. *J. Neurosci.* **38**, 10401–10410 (2018).

Lang, R. et al. Physiology, signaling, and pharmacology of galanin peptides and receptors: three decades of emerging diversity. *Pharmacol. Rev.* **67**, 118-175 (2015).

Lee, J.W. & Jung, M.W. Separation or binding? Role of the dentate gyrus in hippocampal mnemonic processing. *Neurosci. Biobehav. Rev.* **75**, 183–194 (2017).

Lethbridge, R.L., Walling, S.G. & Harley, C.W. Modulation of the perforant path-evoked potential in dentate gyrus as a function of intrahippocampal β-adrenoceptor agonist concentration in urethane-anesthetized rat. *Brain Behav.* **4**, 95-103 (2014).

Li, X. G., Somogyi, P., Ylinen, A. & Buzsáki, G. The hippocampal CA3 network: an in vivo intracellular labeling study. *J. Comp. Neurol.* **339**, 181–208 (1994).

Liberzon, I. et al. Interaction of the ADRB2 gene polymorphism with childhood trauma in predicting adult symptoms of posttraumatic stress disorder. *JAMA Psychiatry* **71**, 1174–1182 (2014).

Liberzon, I. & Abelson, J.L. Context Processing and the Neurobiology of Post-Traumatic Stress Disorder. *Neuron* **92**, 14-30 (2016).

Lisman, J.E. et al. Circuit-based framework for understanding neurotransmitter and risk gene interactions in schizophrenia. *Trends Neurosci.* **31**, 234-242 (2008).

Lisman, J. et al. Viewpoints: How the Hippocampus Contributes to Memory, Navigation and Cognition. *Nat. Neurosci.* **20**, 1434-1447 (2017).

Lissek, S. et al. Overgeneralization of Conditioned Fear as a Pathogenic Marker of Panic Disorder. *Am. J. Psychiatry* **167**, 47-55 (2010).

Lohani S. et al. Burst activation of dopamine neurons produces prolonged post-burst availability of actively released dopamine. *Neuropsychopharmacology* **43**, 2083-2092 (2018).

Lovett-Barron, M. et al. Dendritic Inhibition in the Hippocampus Supports Fear Learning. *Science* **343**, 857-863 (2014).

Loy, R. et al. Noradrenergic innervation of the adult rat hippocampal formation. *J Comp Neurol.* **189**, 699-710 (1980).

Luppi, P.H., Aston-Jones, G., Akaoka, H., Chouvet, G. & Jouvet, M. Afferent projections to the rat locus coeruleus demonstrated by retrograde and anterograde tracing with

cholera-toxin B subunit and *Phaseolus vulgaris* leucoagglutinin. *Neuroscience* **65**, 119–160 (1995).

MacDonald, E. & Scheinin, M. Distribution and pharmacology of α2-adrenoceptors in the central nervous system. *J. Physiol. Pharmacol.* **46**, 241–258 (1995).

Mahn, M., Prigge, M., Ron, S., Levy, R. & Yizhar, O. Biophysical constraints of optogenetic inhibition at presynaptic terminals. *Nat. Neurosci.* **19**, 554-556 (2016).

Mair, R.D., Zhang, Y., Bailey, K.R., Toupin, M.M. & Mair, R.G. Effects of Clonidine in the Locus Coeruleus on Prefrontal- And Hippocampal-Dependent Measures of Attention and Memory in the Rat. *Psychopharmacology (Berl.)* **181**, 280-288 (2005).

Mallory, C.S., Hardcastle, K., Bant, J.S. & Giocomo, L.M. Grid scale drives the scale and long-term stability of place maps. *Nat. Neurosci.* **21**, 270–282 (2018).

Mansour, A. et al. Mu, delta, and kappa opioid receptor mRNA expression in the rat CNS: an in situ hybridization study. *J. Comp. Neurol.* **350**, 412-438 (1994).

Marín-Burgin, A., Mongiat, L.A., Pardi, M.B. & Schinder, A.F. Unique processing during a period of high excitation/inhibition balance in adult-born neurons. *Science* **335**, 1238–1242 (2012).

Marr, D. A theory of cerebellar cortex. *J. Physiol.* **202**, 437–470 (1969).

Marr, D. Simple Memory: A Theory for Archicortex. *Philos. Trans. R. Soc. Lond. B. Biol. Sci.* **262**, 23-81 (1971).

Marshall, K.C., Christie, M.J., Finlayson, P.G. & Williams, J.T. Developmental aspects of the locus coeruleus–noradrenaline system. *Prog. Brain Res.* **88**, 173–185 (1991).

Mather, M., Clewett, D., Sakaki, M. & Harley, C.W. Norepinephrine ignites local hotspots of neuronal excitation: How arousal amplifies selectivity in perception and memory. *Behav. Brain Sci.* **39**, e200 (2016).

McCall, J.G. et al. CRH Engagement of the Locus Coeruleus Noradrenergic System Mediates Stress-Induced Anxiety. *Neuron* **87**, 605-620 (2015).

McCall, J.G. et al. Locus coeruleus to basolateral amygdala noradrenergic projections promote anxiety-like behavior. *Elife* **6**, e18247 (2017).

McGaugh, J.L. The amygdala modulates the consolidation of memories of emotionally arousing experiences. *Annu. Rev. Neurosci.* **27**, 1–28 (2004).

McHugh, T.J. et al. Dentate Gyrus NMDA Receptors Mediate Rapid Pattern Separation in the Hippocampal Network. *Science* **317**, 94-99 (2007).

McNaughton, B.L. & Morris, R.G. Hippocampal synaptic enhancement and information storage within a distributed memory system. *Trends Neurosci.* **10**, 408–415 (1987).

Miller, J.F. et al. Neural activity in human hippocampal formation reveals the spatial context of retrieved memories. *Science* **342**, 1111–1114 (2013).

Miller, S.M. & Sahay, A. Functions of adult-born neurons in hippocampal memory interference and indexing. *Nat. Neurosci.* **22**, 1565–1575 (2019).

Milner, T.A., Shah, P. & Pierce, J.P. beta-adrenergic receptors primarily are located on the dendrites of granule cells and interneurons but also are found on astrocytes and a few presynaptic profiles in the rat dentate gyrus. *Synapse* **36**, 178-193 (2000).

Ming, G. & Song, H. Adult neurogenesis in the mammalian brain: significant answers and significant questions. *Neuron* **70**, 687–702 (2011).

Molinoff, P. B. α- and β-Adrenergic receptor subtypes properties, distribution and regulation. *Drugs* **28**, 1–15 (1984).

Mori, M., Abegg, M.H., Gähwiler, B.H. & Gerber, U. A frequency-dependent switch from inhibition to excitation in a hippocampal unitary circuit. *Nature* **431**, 453–456 (2004).

Morris, R.G. Elements of a Neurobiological Theory of Hippocampal Function: The Role of Synaptic Plasticity, Synaptic Tagging and Schemas. *Eur. J. Neurosci.* **23**, 2829-2846 (2006).

Myers, C. E. & Scharfman, H. E. Pattern separation in the dentate gyrus: a role for the CA3 backprojection. *Hippocampus* **21**, 1190–1215 (2011).

Nadel, L., Samsonovich, A., Ryan, L. & Moscovitch, M. Multiple trace theory of human memory: computational, neuroimaging, and neuropsychological results. *Hippocampus* **10**, 352–368 (2000).

Nagai, T. et al. Divergent projections of catecholamine neurons of the locus coeruleus as revealed by fluorescent retrograde double labeling technique. *Neurosci. Lett.* **23**, 117-123 (1981).

Nakamura, S., Kimura, F. & Sakaguchi, T. Postnatal development of electrical activity in the locus ceruleus. *J. Neurophysiol.* **58**, 510–524 (1987).

Nakazawa, K. et al. Requirement for Hippocampal CA3 NMDA Receptors in Associative Memory Recall. *Science* **297**, 211-218 (2002).

Nicoll, R.A. & Schmitz, D. Synaptic plasticity at hippocampal mossy fibre synapses. *Nat. Rev. Neurosci.* **6**, 863–876 (2005).

Nilssen, E. S., Doan, T. P., Nigro, M. J., Ohara, S. & Witter, M. P. Neurons and networks in the entorhinal cortex: a reappraisal of the lateral and medial entorhinal subdivisions mediating parallel cortical pathways. *Hippocampus* **29**, 1238–1254 (2019).

O'Reilly, R.C. & McClelland, J.L. Hippocampal Conjunctive Encoding, Storage, and Recall: Avoiding a Trade-Off. *Hippocampus* **4**, 661-682 (1994).

Otis, J.M., Werner, C.T. & Mueller, D. Noradrenergic regulation of fear and drug-associated memory reconsolidation. *Neuropsychopharmacology* **40**, 793-803 (2015).

Pang, K. & Rose G.M. Differential effects of norepinephrine on hippocampal complex-spike and theta-neurons. *Brain Res.* **425**, 146-158 (1987).

Pitman, R.K. et al. Pilot study of secondary prevention of posttraumatic stress disorder with propranolol. *Biol Psychiatry* **5**, 189-92 (2002).

Pitman, R.K. et al. Biological studies of post-traumatic stress disorder. *Nat Rev Neurosci* **13**, 769-87 (2012).

Poe, G.R., Walsh, C.M. & Bjorness, T.E. Both duration and timing of sleep are important to memory consolidation. *Sleep* **33**, 1277–1278 (2010).

Poe, G.R. et al. Locus coeruleus: a new look at the blue spot. *Nat Rev Neurosci.* **21**, 644-659 (2020).

Prince, L.Y., Bacon, T.J., Tigaret, C.M. & Mellor, J.R. Neuromodulation of the feedforward dentate gyrus-CA3 microcircuit. *Front. Synaptic Neurosci.* **8**, 32 (2016).

Raimondo, J.V., Kay, L., Ellender, T.J. & Akerman, C.J. Optogenetic silencing strategies differ in their effects on inhibitory synaptic transmission. *Nat. Neurosci.* **15**, 1102-1104 (2012).

Rangel, L. et al. Temporally selective contextual encoding in the dentate gyrus of the hippocampus. *Nat. Commun.* **5**, 3181 (2014).

Resendez, S.L. et al. Visualization of Cortical, Subcortical and Deep Brain Neural Circuit Dynamics During Naturalistic Mammalian Behavior With Head-Mounted Microscopes and Chronically Implanted Lenses. *Nat. Protoc.* **11**, 566–597 (2016).

Robertson, S.D. Developmental origins of central norepinephrine neuron diversity. *Nat. Neurosci*. **16**, 1016-1023 (2013).

Rose, G.M. & Pang, K.C. Differential Effect of Norepinephrine Upon Granule Cells and Interneurons in the Dentate Gyrus. *Brain Res.* **488**, 353-356 (1989).

Rosenbaum, R.S. et al. Remote spatial memory in an amnesic person with extensive bilateral hippocampal lesions. *Nat. Neurosci.* **3**, 1044–1048 (2000).

Rubin, A., Geva, N., Sheintuch, L. & Ziv, Y. Hippocampal Ensemble Dynamics Timestamp Events in Long-Term Memory. *Elife* **4**, e12247 (2015).

Sammer, G., Leifheit, S., Dettbarn, A. & Gallhofer, B. Effects of context information on emotion recognition in schizophrenia. *International Clinical Psychopharmacology* **26**, e175 (2011).

Sara, S.J. & Segal, M. Plasticity of sensory responses of locus coeruleus neurons in the behaving rat: implications for cognition. *Prog. Brain Res.* **88**, 571–585 (1991).

Sara, S.J. The Locus Coeruleus and Noradrenergic Modulation of Cognition. *Nat. Rev. Neurosci.* **10**, 211-223 (2009).

Sasaki, T. et al. Dentate network activity is necessary for spatial working memory by supporting CA3 sharp-wave ripple generation and prospective firing of CA3 neurons. *Nat. Neurosci.* **21**, 258–269 (2018).

Savanthrapadian, S. et al. Synaptic properties of SOM- and CCK-expressing cells in dentate gyrus interneuron networks. *J. Neurosci.* **34**, 8197–8209 (2014).

Scharfman, H., Kunkel, D. & Schwartzkroin, P. A. Synaptic connections of dentate granule cells and hilar neurons: results of paired intracellular recordings and intracellular horseradish peroxidase injections. *Neuroscience* **37**, 693–707 (1990).

Scharfman, H.E. The CA3 'backprojection' to the dentate gyrus. *Prog. Brain Res.* **163**, 627–637 (2007).

Scharfman, H.E. The enigmatic mossy cell of the dentate gyrus. *Nat. Rev. Neurosci.* **17**, 562–575 (2016).

Schmidt-Hieber, C., Jonas, P. & Bischofberger, J. Enhanced synaptic plasticity in newly generated granule cells of the adult hippocampus. *Nature* **429**, 184–187 (2004).

Schwarz, L.A. et al. Viral-genetic tracing of the input-output organization of a central noradrenaline circuit. *Nature*. **524**, 88-92 (2015).

Schwarz, L.A. and Luo, L. Organization of the locus coeruleus-norepinephrine system. *Curr Biol.* **25**, R1051-R1056 (2015).

Seidenbecher, T., Reymann, K.G. & Balschun, D. A Post-Tetanic Time Window for the Reinforcement of Long-Term Potentiation by Appetitive and Aversive Stimuli. *Proc. Natl. Acad. Sci. U S A* **94**, 1494-1499 (1997).

Senzai, Y. & Buzsáki, G. Physiological properties and behavioral correlates of hippocampal granule cells and mossy cells. *Neuron* **93**, 691–704.e5 (2017).

Seo, D.O. & Bruchas, M.R. Polymorphic Computation in Locus Coeruleus Networks. *Nat. Neurosci.* **20**, 1517-1519 (2017).

Seo, D.O. et al. A locus coeruleus to dentate gyrus noradrenergic circuit modulates aversive contextual processing. *Neuron* **109**, 2116–2130.e6 (2021).

Sharma, Y. et al. Comparative anatomy of the locus coeruleus in humans and nonhuman primates. *J. Comp. Neurol.* **518**, 963–971 (2010).

Sheffield, M.E.J., Adoff, M.D. & Dombeck, D.A. Increased prevalence of calcium transients across the dendritic arbor during place field formation. *Neuron* **96**, 490–504 (2017).

Sheintuch, L. et al. Tracking the Same Neurons across Multiple Days in Ca2+ Imaging Data. *Cell Rep.* **21**, 1102-1115 (2017).

Shipley, M.T., Fu, L., Ennis, M., Liu, W.L. & Aston-Jones, G. Dendrites of locus coeruleus neurons extend preferentially into two pericoerulear zones. *J. Comp. Neurol.* **365**, 56–68 (1996).

Shohamy, D. et al. Learning and Generalization in Schizophrenia: Effects of Disease and Antipsychotic Drug Treatment. *Biol. Psychiatry* **67**, 926-932 (2010).

Siegmund, A. & Wotjak, C.T. Toward an Animal Model of Posttraumatic Stress Disorder. *Ann. N. Y. Acad. Sci.* **1071**, 324-334 (2006).

Siuda, E.R. et al. Optodynamic Simulation of β-adrenergic Receptor Signalling. *Nat. Commun.* **6**, 8480 (2015).

Smith, M.E. Bilateral hippocampal volume reduction in adults with post-traumatic stress disorder: a meta-analysis of structural MRI studies. *Hippocampus* **15**, 798-807 (2005).

Squire, L.R. Mechanisms of memory. *Science* **232**, 1612–1619 (1986).

Stadel J.M. & Lefkowitz R.J. The Beta-Adrenergic Receptors. *The Receptors* **1**, 1-40 (1991).

Stefanelli, T., Bertollini, C., Lüscher, C., Muller, D. & Mendez, P. Hippocampal somatostatin interneurons control the size of neuronal memory ensembles. *Neuron* **89**, 1074–1085 (2016).

Strosberg, A.D. Structure, function, and regulation of adrenergic receptors. *Protein Sci*. **2**, 1998-1209 (1993).

Sun, X. et al. Functionally distinct neuronal ensembles within the memory engram. *Cell* **181**, 410–423 (2020).

Swanson, L.W. The locus coeruleus: a cytoarchitectonic, Golgi and immunohistochemical study in the albino rat. *Brain Res.* **110**, 39-56 (1976).

Swift, K.M. et al. Abnormal locus coeruleus sleep activity alters sleep signatures of memory consolidation and impairs place cell stability and spatial memory. *Curr. Biol.* **28**, 3599–3609 (2018).

Szabo, G.G. et al. Extended interneuronal network of the dentate gyrus. *Cell Rep.* **20**, 1262–1268 (2017).

Takeuchi, T. et al. Locus Coeruleus and Dopaminergic Consolidation of Everyday Memory. *Nature* **537**, 357-362 (2016).

Taylor, F.B. et al. Daytime prazosin reduces psychological distress to trauma specific cues in civilian trauma posttraumatic stress disorder. *Biol Psychiatry* **59**, 577-81 (2006).

Taylor, H.R. et al. Prazosin for treatment of nightmares related to posttraumatic stress disorder. *Am J Health Syst Pharm*. **65**, 716-722 (2008).

Tervo, D.G. et al. A Designer AAV Variant Permits Efficient Retrograde Access to Projection Neurons. *Neuron* **92**, 372-382 (2016).

Teyler, T.J. & DiScenna, P. The hippocampal memory indexing theory. *Behav. Neurosci.* **100**, 147 (1986).

Treves, A. & Rolls, E.T. Computational analysis of the role of the hippocampus in memory. *Hippocampus* **4**, 374–391 (1994).

Treves, A., Tashiro, A., Witter, M.P. & Moser, E.I. What Is the Mammalian Dentate Gyrus Good For? *Neuroscience* **154**, 1155-1172 (2008).

Uematsu, A. et al. Modular Organization of the Brainstem Noradrenaline System Coordinates Opposing Learning States. *Nat. Neurosci.* **20**, 1602-1611 (2017).

Ungerstedt, U. Stereotaxic mapping of the monoamine pathways in the rat brain. *Acta Physiol Scand Suppl.* **367**, 1-48 (1971).

Usher, M., Cohen, J.D., Servan-Schreiber, D., Rajkowski, J. & Aston-Jones, G. The role of locus coeruleus in the regulation of cognitive performance. *Science* **283**, 549–554 (1999).

Valentino, R.J. & Van Bockstaele, E. Convergent Regulation of Locus Coeruleus Activity as an Adaptive Response to Stress. *Eur. J. Pharmacol.* **583**, 194-203 (2008).

Vankov, A., Herve-Minvielle, A. & Sara, S.J. Response to novelty and its rapid habituation in locus coeruleus neurons of the freely exploring rat. *Eur. J. Neurosci.* **7**, 1180–1187 (1995).

Varazzani, C., San-Galli, A., Gilardeau, S. & Bouret, S. Noradrenaline and dopamine neurons in the reward/effort trade-off: a direct electrophysiological comparison in behaving monkeys. *J. Neurosci.* **35**, 7866–7877 (2015).

Vivar, C. et al. Monosynaptic inputs to new neurons in the dentate gyrus. *Nat. Commun.* **3**, 1107 (2012).

Vivar, C. & van Praag, H. Functional circuits of new neurons in the dentate gyrus. *Front. Neural Circuits* **7**, 15 (2013).

Wagatsuma, A. et al. Locus Coeruleus Input to Hippocampal CA3 Drives Single-Trial Learning of a Novel Context. *Proc. Natl. Acad. Sci. U S A.* **115**, E310-E316 (2018).

Walling, S.G. & Harley, C.W. Locus Coeruleus Activation Initiates Delayed Synaptic Potentiation of Perforant Path Input to the Dentate Gyrus in Awake Rats: A Novel Beta-Adrenergic- And Protein Synthesis-Dependent Mammalian Plasticity Mechanism. *J. Neurosci.* **24**, 598-604 (2004).

Wang, C. et al. Egocentric coding of external items in the lateral entorhinal cortex. *Science* **362**, 945–949 (2018).

Wang, F. et al. RNAscope: A Novel in Situ RNA Analysis Platform for Formalin-Fixed, Paraffin-Embedded Tissues. *J. Mol. Diagn.* **14**, 22–29 (2012).

Waterhouse, B.D. & Chandler, D.J. Heterogeneous organization and function of the central noradrenergic system. *Brain Res.* **1641**, v–x (2016).

Woods, N.I. et al. Preferential targeting of lateral entorhinal inputs onto newly integrated granule cells. *J. Neurosci.* **38**, 5843–5853 (2018).

Xavier, G.F. & Costa, V.C.I. Dentate gyrus and spatial behaviour. *Prog. Neuro-psychopharmacol. Biol. Psychiatry* **33**, 762–773 (2009).

Xu, Y.L. et al. Neuropeptide S: a neuropeptide promoting arousal and anxiolytic-like effects. *Neuron* **43**, 487–497 (2004).

Yassa, M. A. & Stark, C. E. Pattern separation in the hippocampus. *Trends Neurosci.* **34**, 515–525 (2011).

Young 3rd, W.S. & Kuhar, M.J. Noradrenergic alpha 1 and alpha 2 receptors: light microscopic autoradiographic localization. *Proc. Natl. Acad. Sci. USA*. **77**, 1696-1700 (1980).

Yu, A.J. & Dayan, P. Uncertainty, neuromodulation, and attention. *Neuron* **46**, 681–692 (2005).

Zerbi, V. et al. Rapid reconfiguration of the functional connectome after chemogenetic locus coeruleus activation. *Neuron* **103**, 702–718.e5 (2019).

Zhou, P. et al. Efficient and Accurate Extraction of in Vivo Calcium Signals From Microendoscopic Video Data. *Elife* **7**, e28728 (2018).

Zhuo, J.-M. et al. Young adult born neurons enhance hippocampal dependent performance via influences on bilateral networks. *eLife* **5**, e22429 (2016).

Ziv, Y. et al. Long-term dynamics of CA1 hippocampal place codes. *Nat. Neurosci.* **16**, 264–266 (2013).

Zucca, S. et al. Control of spike transfer at hippocampal mossy fiber synapses in vivo by $GABA_A$ and $GABA_B$ receptor-mediated inhibition. *J. Neurosci.* **37**, 587–598 (2017).

Appendix References

Arroyo-Curras, N. et al. Real-time measurement of small molecules directly in awake, ambulatory animals. *Proc Natl Acad Sci U S A* **114**, 645-650 (2017).

Baker, B.R. et al. An electronic, aptamer-based small-molecule sensor for the rapid, label-free detection of cocaine in adulterated samples and biological fluids. *J Am Chem Soc.* **128**, 3138-3139 (2006).

Bao, W.W. et al. Nucleus accumbens neurons expressing dopamine D1 receptors modulate states of consciousness in sevoflurane anesthesia. *Current Biology* **31**, 1893-1902. e5 (2021).

Bidinger, S.L. et al. Pulsed transistor operation enables miniaturization of electrochemical aptamer-based sensors. *Sci Adv* **8**, eadd4111 (2022).

Dauphin-Ducharme, P. et al. Electrochemical Aptamer-Based Sensors for Improved Therapeutic Drug Monitoring and High-Precision, Feedback-Controlled Drug Delivery. *ACS Sens.* **4**, 2832-2837 (2019).

Dauphin-Ducharme, P. et al. Redox Reporter - Ligand Competition to Support Signaling in the Cocaine-Binding Electrochemical Aptamer-Based Biosensor. *Chemistry* **29**, e202300618 (2023).

Downs, A.M. et al. Nanoporous Gold for the Miniaturization of In vivo Electrochemical Aptamer Based Sensors. *ACS Sens*. **6**, 2299-2306 (2021).

Downs, A.M. & Plaxco, K.W. Real-Time, In vivo Molecular Monitoring Using Electrochemical Aptamer Based Sensors: Opportunities and Challenges. *ACS Sens.* **7**, 2823-2832 (2022).

Ferguson, B.S. et al. Real-time, aptamer-based tracking of circulating therapeutic agents in living animals. *Sci Transl Med* **5**, 213ra165 (2013).

Flynn, C.D. et al. Biomolecular sensors for advanced physiological monitoring. *Nature Reviews Bioengineering* **1**, 560–575 (2023).

Friedel, M. et al. Opportunities and challenges in the diagnostic utility of dermal interstitial fluid. *Nature Biomedical Engineering* **7**, 1541-1555 (2023).

Fu, W., Jiang, L., van Geest, E.P., Lima, L.M. & Schneider, G.F. Sensing at the surface of graphene field-effect transistors. *Advanced Materials* **29**, 1603610 (2017).

Gao, Z. et al. Multiplexed Monitoring of Neurochemicals via Electrografting-Enabled Site-Selective Functionalization of Aptamers on Field-Effect Transistors. *Anal Chem* **94**, 8605-8617 (2022).

Hajnal, A. & Norgren, R. Accumbens dopamine mechanisms in sucrose intake. *Brain Res* **904**, 76-84 (2001).

Hajnal, A. & Norgren, R. Repeated access to sucrose augments dopamine turnover in the nucleus accumbens. *Neuroreport* **13**, 2213-2216 (2002).

Idili, A., Gerson, J., Kippin, T. & Plaxco, K.W. Seconds-Resolved, In Situ Measurements of Plasma Phenylalanine Disposition Kinetics in Living Rats. *Anal Chem* **93**, 4023-4032 (2021).

Jeong, J.W. et al. Wireless Optofluidic Systems for Programmable In vivo Pharmacology and Optogenetics. *Cell* **162**, 662-674 (2015).

Kim, T.I. et al. Injectable, cellularscale optoelectronics with applications for wireless optogenetics. *Science* **340**, 211216 (2013).

Lu, L. et al. Wireless optoelectronic photometers for monitoring neuronal dynamics in the deep brain. *Proc Natl Acad Sci U S A* **115**, E1374-E1383 (2018).

McCutcheon, J.E., Beeler, J.A. & Roitman, M.F. Sucrose-predictive cues evoke greater phasic dopamine release than saccharin-predictive cues. *Synapse* **66**, 346-351 (2012).

Parolo, C. et al. Real-Time Monitoring of a Protein Biomarker. *ACS Sens.* **5**, 1877-1881 (2020).

Patriarchi, T. et al. Ultrafast neuronal imaging of dopamine dynamics with designed genetically encoded sensors. *Science* **360**, eaat4422 (2018).

Phillips, P.E., Stuber, G.D., Heien, M.L., Wightman, R.M. & Carelli, R.M. Subsecond dopamine release promotes cocaine seeking. *Nature* **422**, 614-8 (2003).

Reiner-Rozman, C., Larisika, M., Nowak, C. & Knoll, W. Graphene-based liquid-gated field effect transistor for biosensing: Theory and experiments. *Biosens Bioelectron* **70**, 2127 (2015).

Sempionatto, J.R., Lasalde-Ramirez, J.A., Mahato, K., Wang, J. & Gao, W., Wearable chemical sensors for biomarker discovery in the omics era. *Nat. Rev. Chem.* **6**, 899-915. (2022).

Shaver, A. & Arroyo-Curras, N. The challenge of long-term stability for nucleic acid-based electrochemical sensors. *Curr Opin Electrochem* **32**, 100902 (2022).

Torricelli, F. et al. Electrolyte-gated transistors for enhanced performance bioelectronics. *Nature Reviews Methods Primers* **1**, 66 (2021).

Tran, T.T. & Mulchandani, A. Carbon nanotubes and graphene nano field-effect transistor-based biosensors. *TrAC Trends in Analytical Chemistry* **79**, 222-232 (2016).

Tsai, H. C. et al. Phasic firing in dopaminergic neurons is sufficient for behavioral conditioning. *Science* **324**, 1080-1084 (2009).

Wang, G.Y., Lian, K. & Chu, T.Y. Electrolyte-gated field effect transistors in biological sensing: A survey of electrolytes. *IEEE Journal of the Electron Devices Society* **9**, 939-950 (2021).

White, R.J., Phares, N., Lubin, A.A., Xiao, Y. & Plaxco, K.W. Optimization of electrochemical aptamer-based sensors via optimization of probe packing density and surface chemistry. *Langmuir* **24**, 10513-10518 (2008).

Wu, G. et al. Implantable Aptamer-Graphene Microtransistors for Real-Time Monitoring of Neurochemical Release in vivo. *Nano Lett* **22**, 3668-3677 (2022).

Wu, Y. et al. Microneedle Aptamer-Based Sensors for Continuous, Real-Time Therapeutic Drug Monitoring. *Anal Chem* **94**, 8335-8345 (2022).

Zhang, H. et al. Wireless, battery-free optoelectronic systems as subdermal implants for local tissue oximetry. *Sci Adv* **5**, eaaw0873 (2019).

Zhao, C. et al., Implantable aptamer-field-effect transistor neuroprobes for in vivo neurotransmitter monitoring. *Sci Adv* **7**, eabj7422 (2021).